Master Thesis

Electron Detection Efficiency of the CBM-TRD Prototypes in Testbeams at DESY

Adrian Meyer-Ahrens

Westfälische Wilhelms-Universität Münster
Institut für Kernphysik

06.03.2019

Erster Gutachter: Prof. Dr. Anton Andronic
Zweiter Gutachter: Prof. Dr. Christian Klein-Bösing

"The most merciful thing in the world, I think, is the inability of the human mind to correlate all its contents. We live on a placid island of ignorance in the midst of black seas of infinity, and it was not meant that we should voyage far."

Howard Phillips Lovecraft [Lov28]

Contents

Acronyms

ADC Analog to Digital Converter (also used as unit)

AFCK AMC FMC Carrier Kintex

ALICE A Large Ion Collider Experiment

AMC Advanced Mezzanine Card

ASIC Application Specific Integrated Circuit

BM@N Baryonic Matter at Nuclotron

CBM Compressed Baryonic Matter

CBM-TRD Transition Radiation Detector for the CBM Experiment

CERN Conseil Européen pour la Recherche Nucléaire

CSA Charge Sensitive Amplifier

DAQ Data Acquisition

DESY Deutsches Elektronen-Synchrotron

DORIS Doppel-Ring-Speicher

DSP Digital Signal Processor

FAIR Facility for Antiproton and Ion Research

FEB Front-End Board

FIFO First In, First Out

FLES First Level Event Selector

FLIB FLES Interface Board

FMC FPGA Mezzanine Card

FNR Forced Neighbor Readout

FPGA Field Programmable Gate Array

GSI	Gesellschaft für Schwerionenforschung
IC	Integrated Circuit
MWPC	Multi Wire Proportional Chamber
PE	PolyEthylene
PETRA	Positron-Elektron-Tandem-Ring-Anlage
PIA	Positron Intensity Accumulator
PMT	Photomultiplier
PVT	Polyvinyl Toluene
QA	Quality Assurance
QCD	Quantum Chromodynamics
QGP	Quark-Gluon Plasma
RHIC	Relativistic Heavy Ion Collider
SD	Scintillation Detector
SPADIC	Self-triggered Pulse Amplification and Digitisation as IC
STAR	Solenoidal Tracker at RHIC
TR	Transition Radiation
TRD	Transition Radiation Detector
TS	Time Stamp
TSA	Timeslice Archive

1. Introduction

How does one observe objects so small that millions of them would fit on a single grain of sand, if anyhow outer dimensions can even be considered? How to make incomprehensively small, seemingly invisible objects visible is one of the most fundamental and constantly asked questions in detector physics. While the elementary particles in physics have decreased significantly in size over the last 100 years from atoms, over nuclei and nucleons, to quarks, so have the detectors increased in size and complexity from Geiger counters emitting a sound when radiation is detected, to giant setups like the ALICE detector, consisting of various subsystems and providing several GByte/s of data when running.
A planned experiment creating new challenges for detector systems, especially in terms of rate capability, is the Compressed Baryonic Matter (CBM) experiment. CBM is a fixed target collider experiment, which will start operation in 2025 and take place at the new accelerator complex Facility for Antiproton and Ion Research (FAIR), which is currently under construction at the *Helmholtzzentrum der Gesellschaft für Schwerionenforschung* (GSI) in Darmstadt, Germany.
Main task of CBM is gaining new knowledge about the Quantum Chromodynamics (QCD) phase diagram, and especially investigating the transition of baryonic matter to the Quark-Gluon Plasma (QGP). The QGP is a state of matter, in which quarks and gluons are no longer bound in nucleons and which is only achieved at very high temperatures and/or baryon densities [CBM18]. As the QGP is a very short lived state, it cannot be observed directly, but rather through particles that mostly formed after expansion and freeze-out of the QGP volume. To acquire sufficient statistics even on rare probes of the QGP, CBM will be operated at high interaction rates up to 10 MHz, which is two orders of magnitude larger than comparable existing heavy-ion experiments such as BM@N or STAR [A^{+}17].
The detector setup for this experiment will consist of various subsystems, each with its own specific tasks and properties. One of these is the Transition Radiation Detector for the CBM Experiment (CBM-TRD). Its main tasks are the identification of electrons and positrons with a momentum $p > 1.0\,\mathrm{GeV}/c$ and particle tracking [CBM18].
To successfully conduct measurements at interaction rates as high as the ones planned for CBM, new detector and readout concepts had to be developed and tested. For this purpose, four current CBM-TRD prototypes have been set up at a test beam area at *Deutsches Elektronen-Synchrotron* (DESY) in 2017, where measurements with electron beams at momenta ranging from 1 to $4\,\mathrm{GeV}/c$ have been conducted. As the detectors themselves are expected to have an electron

detection efficiency near to 100 %, its calculation from the measured data can serve as a valuable system check, which is the primary motivation for this thesis. Furthermore, since the DESY 2017 test beam campaign was the first to readout and correlate data from multiple detectors with the (then) current readout electronics, a great amount of Quality Assurance (QA) had to be done, to evaluate and secure the general functionality of the system.

This thesis is divided into five chapters. Following this introduction, the theoretical and experimental background will be presented in Chapter 2. Here, the basic processes of interaction of particles with matter as well as their application in detector physics will be explained, namely the working principles of the used detectors. Subsequently, in Chapter 3 the properties of the actual setup used at the DESY 2017 test beam will be described, ranging from the electron beam generation over detector properties to readout electronics. In Chapter 4, results of the analysis regarding QA and electron detection efficiencies of the CBM-TRD prototypes will be presented, before a conclusion and outlook is given in Chapter 5.

2. Theoretical & Experimental Background

2.1. Interaction of Particles with Matter

When a particle passes through matter, the occuring interaction processes and the energy deposit by these interactions depend on various parameters such as the particle's charge, its momentum and the atomic number of the transversed matter. In this chapter, the interaction processes of relevance in the course of this thesis between particles and matter and their most important dependencies will be discussed.

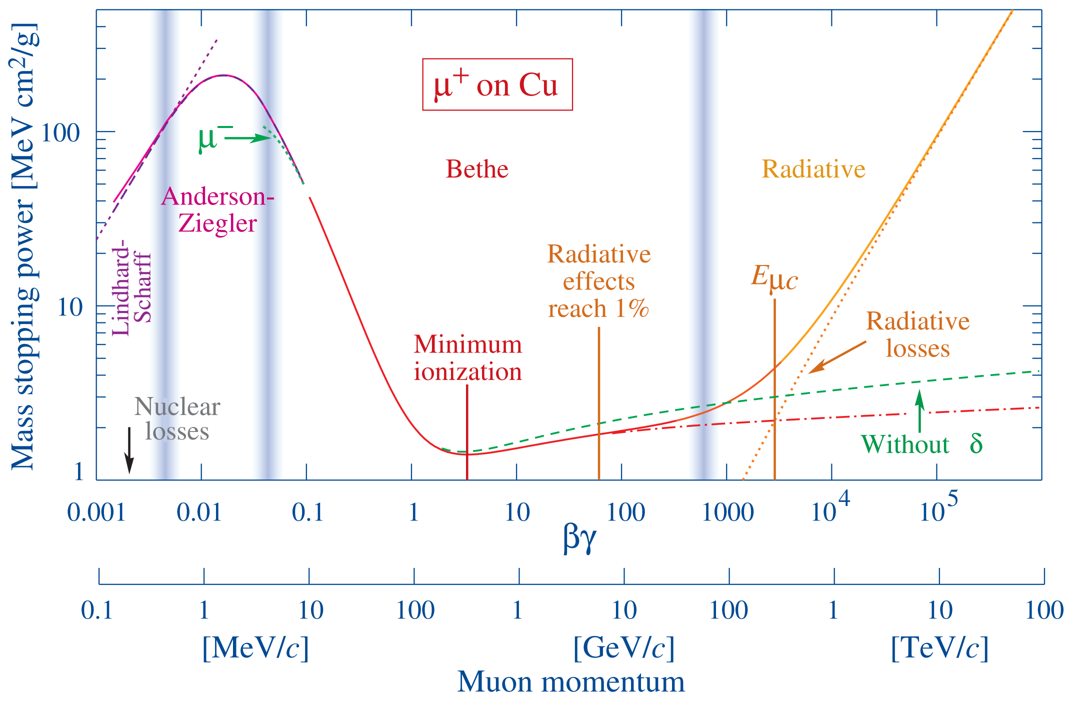

Figure 2.1.: Mean energy loss of a positive muon passing through copper depending on its $\beta\gamma$: The region of intermediate $\beta\gamma$ can be described by Equation 2.1 [T+18].

2.1.1. Heavy Charged Particles

Moderately relativistic charged heavy particles lose their energy mainly through single inelastic collisions with shell electrons, resulting in ionization of atoms in the surrounding material [T+18]. The particle's mean energy loss per distance can be described by the *Bethe-Equation*:

$$\left\langle -\frac{dE}{dx} \right\rangle_{\text{ion}} = Kz^2 \frac{Z}{A} \frac{1}{\beta^2} \left[\frac{1}{2} \ln \frac{2m_e c^2 \beta^2 \gamma^2 T_{\max}}{I^2} - \beta^2 - \frac{\delta(\beta\gamma)}{2} \right]. \tag{2.1}$$

For intermediate-Z materials this equation has an accuracy of a few percent in the range of $0.1 \lesssim \beta\gamma \lesssim 1000$ where $\beta = \frac{v}{c}$ and $\gamma = \frac{1}{\sqrt{1-\beta^2}}$ [T+18]. All further variables and constants of Equation 2.1 are listed in Table 2.1. A graphical visualization of the $\beta\gamma$ dependence of the energy loss of a positive muon through copper can be seen in Figure 2.1, with the Bethe region described by Equation 2.1 being located at intermediate $\beta\gamma$. In the lower limit of the Bethe region, shell corrections accounting for atomic binding have to be included. Radiative energy losses by bremsstrahlung (see Section 2.1.2) become relevant in the upper end of the Bethe region [T+18].

Table 2.1.: Variables and constants used in 2.1. All values are taken from [T+18].

Symbol	Definition	Value or (usual) units
K	$4\pi N_{\mathrm{A}} r_e^2 m_e c^2$	$0.31\,\mathrm{MeV\ mol^{-1}\ cm^2}$
N_{A}	Avogadro's number	$6.02 \times 10^{23}\,\mathrm{mol^{-1}}$
r_e	classical electron radius	$2.82\,\mathrm{fm}$
$m_e c^2$	electron mass $\times c^2$	$0.51\,\mathrm{MeV}$
z	charge number of incident particle	
Z	atomic number of absorber	
A	atomic mass of absorber	$\mathrm{gmol^{-1}}$
$T_{\max}$	maximum energy transfer to an electron in a single collision	MeV
I	mean excitation energy	eV
$\delta(\beta\gamma)$	density effect correction	

2.1.2. Electrons

When being decelerated, charged particles emit their lost kinetic energy as photons. This radiation is called *bremsstrahlung* [Kle05]. As its emission probability is proportional to the energy of the particle but inversly proportional to the square of its mass, for particles heavier than electrons it only becomes relevant at very high energies [Leo87] (See Figure 2.1). For electrons (and positrons) on the other hand, bremsstrahlung is the dominant source of energy loss already at a few MeV depending on the surrounding material, as pointed out in Figure 2.2.

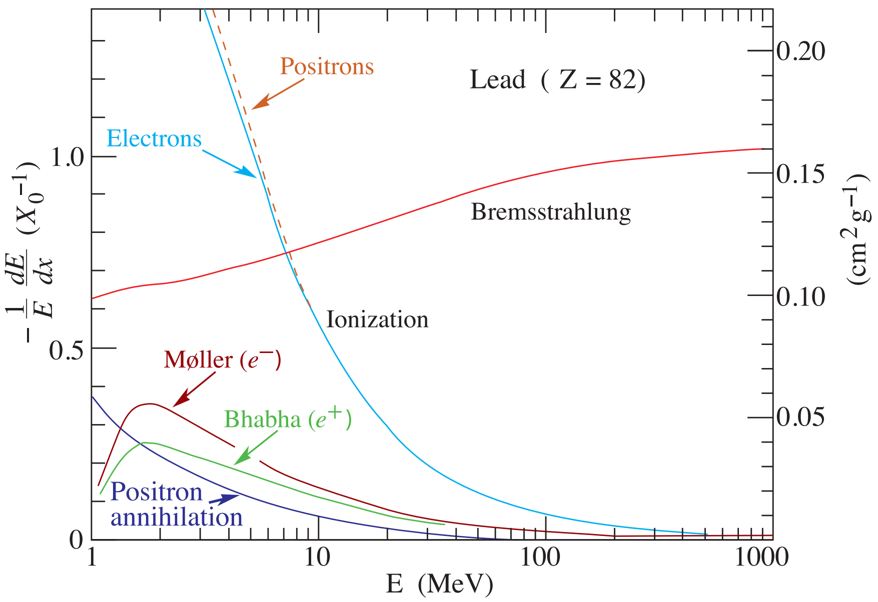

Figure 2.2.: Fractional energy loss of electons/positrons per radiation length in lead plotted as a function of electron/positron energy: At lower energies, energy loss by collision processes is dominant, which significantly decreases with increasing energy. For very high energies, the energy loss by collision is negligible and the total loss can be approximated by bremsstrahlung alone [T+18].

The mean energy loss by bremsstrahlung per distance can be described by:

$$\left\langle -\frac{dE}{dx} \right\rangle_{\text{brem}} = \frac{E}{X_0}. \tag{2.2}$$

X_0 is the particle's *radiation length*, the mean traversed distance over which it emits all but $\frac{1}{e}$ of its energy via bremsstrahlung. For electrons it is given by Equation 2.3 [Kle05]:

$$\frac{1}{X_0} = 4\alpha N_0 \frac{Z^2}{A} r_e^2 \ln \frac{183}{Z^{1/3}}. \tag{2.3}$$

Here, r_e is the classical electron radius, defined by [T+18]:

$$r_{\text{e}} = \frac{e^2}{4\pi\varepsilon_0 m_e c^2}. \tag{2.4}$$

By calculating the classical radius of charged particles other than electrons, one can also obtain their radiation length. Since the classical radius has an inverse mass dependence, particles heavier than electrons have larger radiation lengths. This makes it a less useful property to descibe their energy loss because a significant amount of energy is lost through ionisation in the distance of one radiation length. For highly relativistic electrons on the other hand, the energy loss can be approximated by bremsstrahlung only, neglecting other sources of energy loss like ionisation or Møller scattering. At lower energies, at which these collision processes have to be taken into account, the energy loss can be described by Equation 2.5. This equation is similar to the Bethe equation but includes additional correction terms due to the comparatively low mass of electrons and their indistinguishability with shell electrons in the medium [T+18, Leo87].

$$\begin{aligned}\left\langle -\frac{dE}{dx} \right\rangle_{\mathrm{col}} = \frac{1}{2} K \frac{Z}{A} \frac{1}{\beta^2} \Bigg[\ln \frac{m_e c^2 \beta^2 \gamma^2 \left\{ m_e c^2 (\gamma - 1)/2 \right\}}{I^2} \\ + (1 - \beta^2) - \frac{2\gamma - 1}{\gamma^2} \ln 2 + \frac{1}{8} \left(\frac{\gamma - 1}{\gamma} \right)^2 - \delta \Bigg]\end{aligned} \tag{2.5}$$

Finally, the total energy loss is then given by adding radiative and collision energy loss [Leo87]:

$$\left\langle -\frac{dE}{dx} \right\rangle_{\mathrm{tot}} = \left\langle -\frac{dE}{dx} \right\rangle_{\mathrm{col}} + \left\langle -\frac{dE}{dx} \right\rangle_{\mathrm{brems}} . \tag{2.6}$$

2.1.3. Photons

Contrary to charged particles, photons do not deposit their energy through several collisions on their path through a medium, but rather in one single interaction. Depending on the initial energy of the photon and the atomic number of the surrounding material, there are three different processes resulting in energy loss that may occur.

At low photon energies (of the order of the binding energies of electrons), the photoelectric effect is predominant, getting surpassed by Compton scattering at intermediate energies, while pair production is the most likely process at high energies as can be deduced in Figure 2.3 [Kle05]. In an energy range similar to that of the photoelectric effect also Rayleigh scattering is possible, but as an elastic process it does not contribute to the energy loss of the photon [Leo87]. The cross sections of all of these processes increase in media with higher atomic numbers. For the photoelectric effect and Compton scattering, this is due to the presence of more electrons, while increased pair production comes from a stronger electric field of the atomic nucleus. The *order* of Z dependence differs from process to process (photoelectric effect between $\propto Z^4$ and Z^5, compton scattering $\propto Z$ and pair production $\propto Z^2$), resulting in the photoelectric effect being dominant in absorbers with higher Z [KW16].

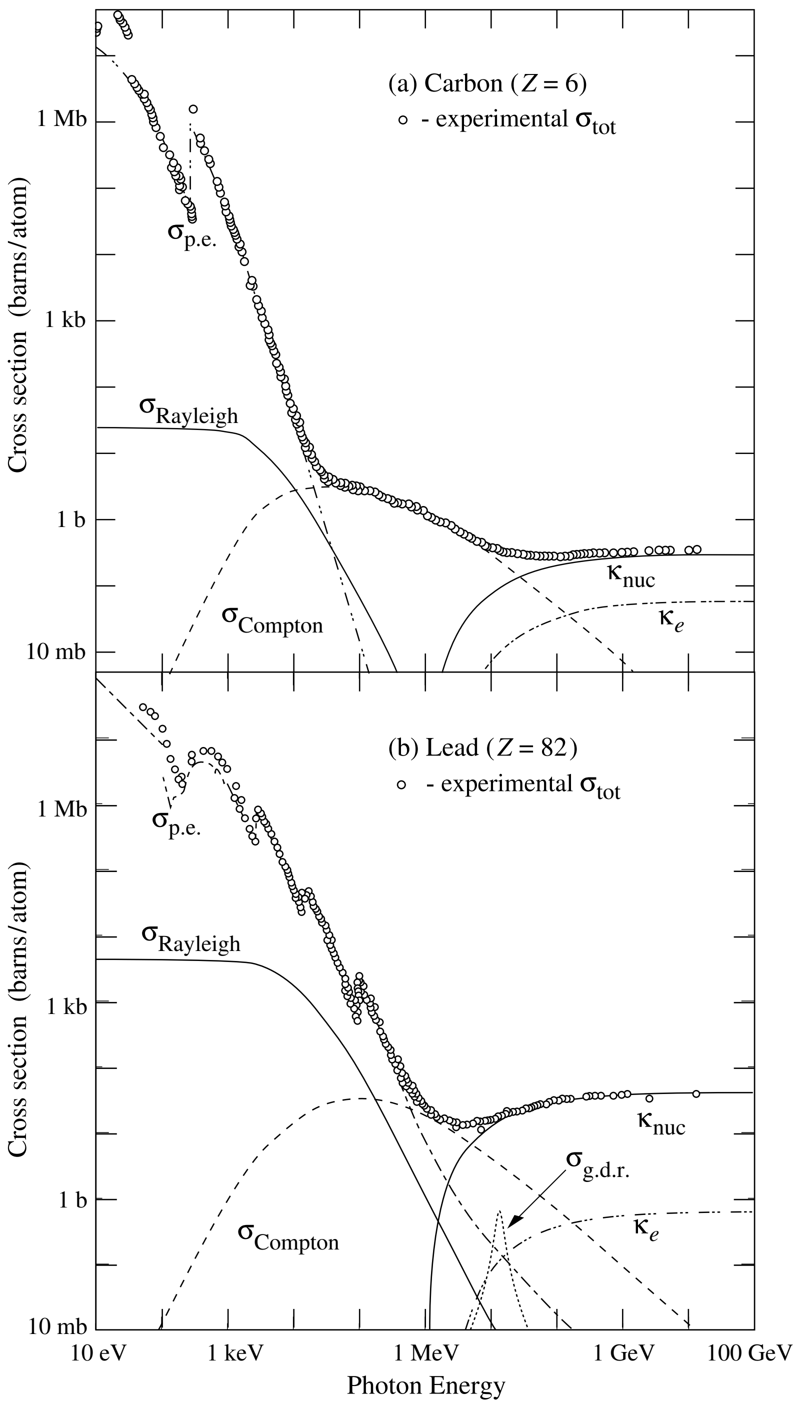

Figure 2.3.: Cross sections of photon interaction processes as a function of its energy in carbon (upper panel) and lead (lower panel): Generally, the photoeffect is dominant at low energies, Compton scattering at intermediate energies and pair production at high energies. Since the cross section of Compton scattering has a comparably weak dependence on Z, the energy range in which it is the dominant source of energy loss decreases from carbon to lead [T+18].

2.2. Multi Wire Proportional Chambers

A Multi Wire Proportional Chamber (MWPC) is a commonly used particle detector consisting of an array of equally spaced anode wires between two cathode planes [Leo87]. With a layer of cathode wires it can also be extended to a Drift-MWPC, as is shown in Figure 2.4 [Ber14]. The chamber is usually filled with a gas mixture containing a heavy noble gas and an organic quenching component. Alternatively, purely organic gas mixtures are possible [BRR08].
The electrical field resulting from applying a voltage to a wire grid as it is used in MWPCs is sketched in Figure 2.4. As evident from the field lines, the field is almost constant, except in the region close to the anode wires where it has an $1/r$ dependence [Leo87].
A particle entering the detector will interact with the chamber gas through the processes described in Section 2.1, resulting in electron ion pairs. The positive ions will then be accelerated to the cathode planes, while the electrons move to the anode wires. Due to the $1/r$ dependence of the electric field close to the anode wires, the electrons velocity increases significantly upon entering this region, where it then ionizes further atoms and creates an avalanche. As the electron avalanche is collected by the anode wire, it can be either measured directly as a current or by its induced mirror charge on the cathode plane [BRR08].

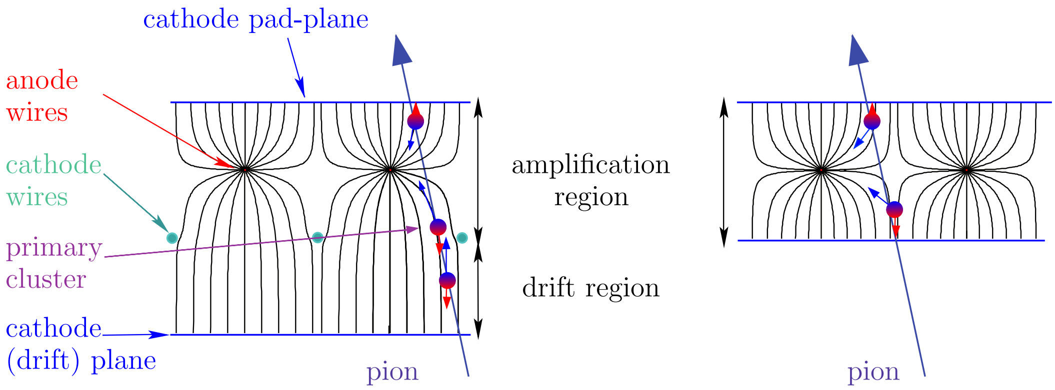

Figure 2.4.: Two different types of MWPCs: The Drift-MWPC with an additional cathode wire plane (left) and a symmetric simple MWPC (right): An incident particle will create electron ion pairs which are separated by the applied electric field. The positive ions drift to the cathode pads while the electrons drift to the anode wires. Close to the anode wires the electric field increases, accelerating the electron and causing it to create an avalanche. The avalanche is then measured as a current on the anode wire or as a mirror charge on the cathode pad-plane. [Ber14]

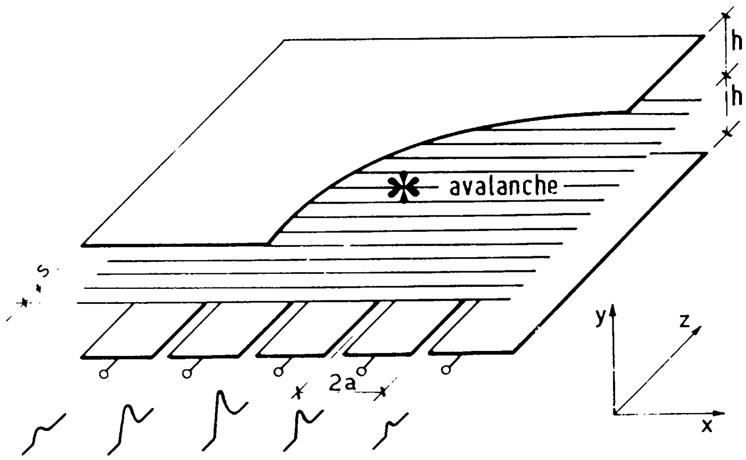

Figure 2.5.: Sketch of a MWPC with one cathode plane divided into single pads: As visualized by the pulses at the bottom, the induced signal is the stronger the closer the pad is to the position of the avalanche, enabling position resolved measurements. By adding up the charge on all cathode pads, the total deposited energy can be determined [BRR08].

By separating the cathode plane into single cathode pads, the position of the avalanche can be obtained since the charge induction is a localised effect. Because most charge amplification takes place in the region very close to the anode wire, the total strength of the avalanche (and thus the total induced signal) does not depend on the position of the primary ionization, but only on the amount of energy deposited by the incident particle [Leo87]. The signal induced by an avalanche at a certain position in the chamber is sketched in Figure 2.5. As visible in the drawing, the strongest signal is induced on the pad closest to the avalance and decreases with growing distance. By examining the distribution of the induced charge over the pads, the position of the avalanche can be determined with a resolution even smaller than the pad width [BRR08].

The addition of a drift region on one side of the amplification region increases the detector volume and thus also the interaction probability of the incidenct particle with the detector gas. Furthermore, it can stabilize the gas amplification against external pressure variations, which works as follows: In some cases (e.g. the CBM-TRD), the side of the detector where particles are expected to enter is relatively thin. This reduces material budget and increases the probality of low energy particles like TR photons (see Section 2.3.2) to reach the active detector volume. Therefore, the cathode plane on the entrance side is able to bend outwards or inwards if the pressure inside or outside of chamber varies, which will also alter its electrical field. If a drift region is added on the entrance side, this will not have an effect on the electrical field amplification region, but only in the drift region [CBM18].

2.3. Transition Radiation Detectors

A Transition Radiation Detector (TRD) normally consists of two parts. First there is the so-called *radiator*, a material causing traversing particles to emit Transition Radiation (TR). Behind the radiator, one type of a conventional radiation detector (e.g. MWPC, silicon detector) is placed, measuring both the energy loss of the particle itself as well as its produced TR. In this section, at first general characteristics of TR and its production in radiators will be described (Section 2.3.1). Subsequently, its application in detector physics is discussed (Section 2.3.2).

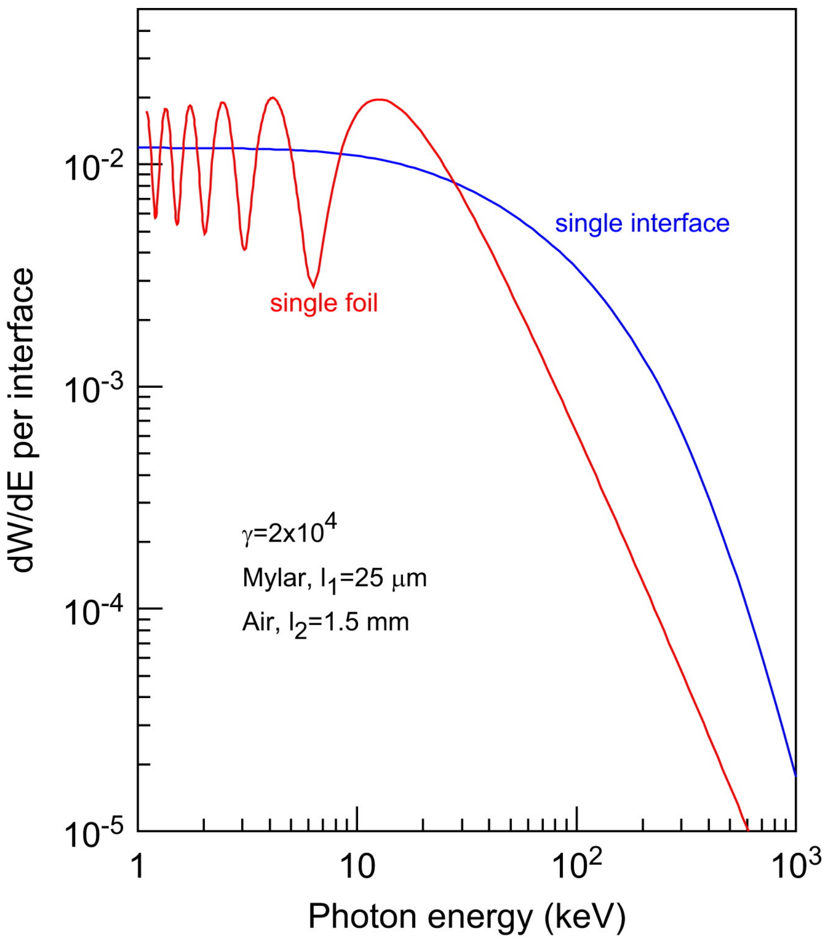

Figure 2.6.: Simulated TR spectrum of a particle with $\gamma = 2 \cdot 10^4$ transitioning between air and mylar at a single interface (blue) and through a foil with two interfaces (red) [AW12]

2.3.1. Transition Radiation

A relativistic charged particle crossing the boundary between two media with different dielectric constants emits so-called TR. Its double differential energy spectrum depending on the particles Lorentz factor γ and the dielectric properties of the two media can be described as follows:

$$\frac{d^2W}{d\omega d\Omega} = \frac{\alpha}{\pi^2}\left(\frac{\theta}{\gamma^{-2}+\theta^2+\xi_1^2} - \frac{\theta}{\gamma^{-2}+\theta^2+\xi_2^2}\right). \tag{2.7}$$

Equation 2.7 is valid for $\gamma \gg 1$ and $\xi_1^2, \theta \ll 1$ and $\xi_2^2 \ll 1$ with $\xi_i^2 = \omega_{Pi}^2/\omega^2$. ω_P^2 is the plasma frequency of the surrounding material, which depends on its electron density n_e. It can be calculated by [AW12]:

$$\omega_P = \sqrt{\frac{4\pi\alpha n_e}{m_e}}. \tag{2.8}$$

From Equation 2.7 follows that there is a shift to higher energies for increasing γ. This results in more TR leaving the medium, since low energy photons are mostly absorbed [T$^+$18]. A graphical visualization of a possible TR spectrum can be seen in Figure 2.6.
Most of the TR is produced in the so called "formation zone" Z_i, the distance over which the TR photon is separated from the parent particle. As can be seen in Equation 2.9, it depends on the particle's Lorentz factor as well as the energy of the TR photon and its emission angle, which for high γ can be approximated by $\theta \simeq 1/\gamma$.

$$Z_i = \frac{1}{\gamma^{-2}+\xi_i^2}\frac{2\gamma c}{\omega} \tag{2.9}$$

If the formation zone is much longer than the distance traveled in the medium $l_i \ll Z_i$, the TR yield is suppressed [AW12]. Since TR is produced when a charged particle enters a medium as well as when it leaves the medium again, interference has also to be taken into account. For a foil with two interfaces this can be done by adding a correction factor to Equation 2.7 [AW12]:

$$\left(\frac{d^2W}{d\omega d\Omega}\right)_{\text{foil}} = \left(\frac{d^2W}{d\omega d\Omega}\right)_{\text{interface}} \cdot 4\sin^2\left(\frac{\phi_i}{2}\right). \tag{2.10}$$

The phase ϕ_i in the correction factor can be approximated by [AW12]:

$$\phi_i \simeq \frac{(\gamma^{-2}+\theta^2+\xi_i^2)\omega l_i}{2\beta c}. \tag{2.11}$$

Finally, by taking into account absorption of low energy TR, suppression of TR with a formation zone longer than the length of the medium and interference effects, TR yield spectra for radiators with multiple foil layers can be calculated. In Figure 2.7 the dependence of the TR yield on γ as well as the foil thickness l_1 and the foil spacing l_2 (i.e. the thickness of the air volume between two foils) are visualized.
It is visible in the upper panel of Figure 2.7 that the yield dependency on γ is threshold-like, with almost no TR being produced at $\gamma = 391$ (blue data points) but then increasing drastically with rising γ.
For both l_1 (foil thickness) and l_2 (foil spacing) the yield saturates when the length of the formation zone in the respective medium is reached ($\approx 7\,\mu$m for CH_2 and $\approx 700\,\mu$m for air). An increased foil thickness also increases the absorption of photons on the lower end of the energy spectrum as can be seen by the red data points on the middle panel of Figure 2.7.

Apart from radiators composed out of n layers of foil with regular thickness and spacing also irregular radiators consisting of foam or fibers can be used to produce TR. Since there is no coherent interference of TR photons, the yield in irregular radiators is smaller than in regular ones. This is partly compensated by smaller structure sizes, thus resulting in more boundaries per unit length [CBM18]. In practice, irregular radiators are often favored due to their greater physical stability, smaller sensitivity for external factors such as temperature and pressure, as well as their lower production costs.

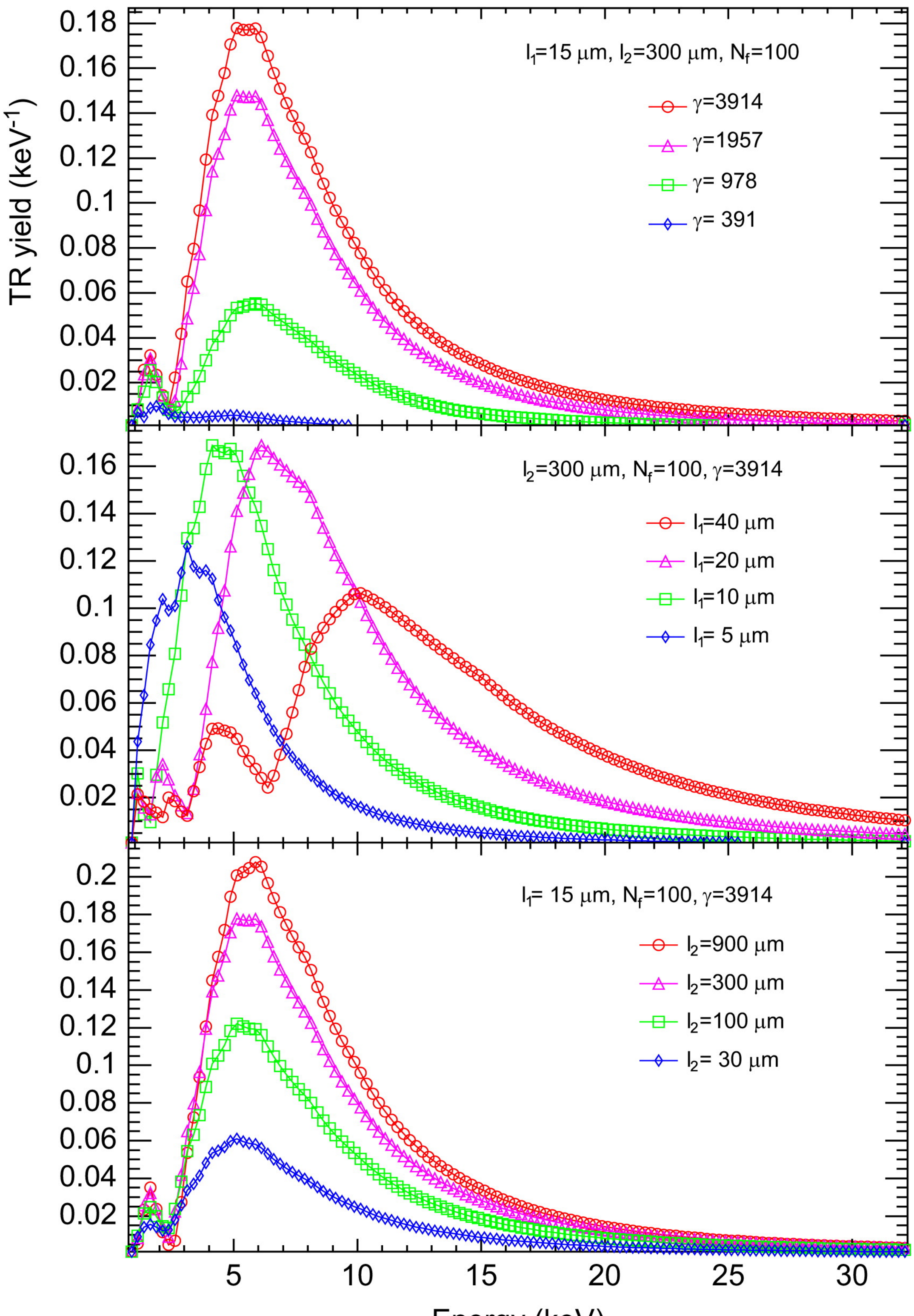

Figure 2.7.: Simulated TR yields for a 100 foil radiator depending on the Lorentz factor γ (upper panel), foil thickness l_1 (middle panel) and foil spacing l_2 (lower panel) [AW12]

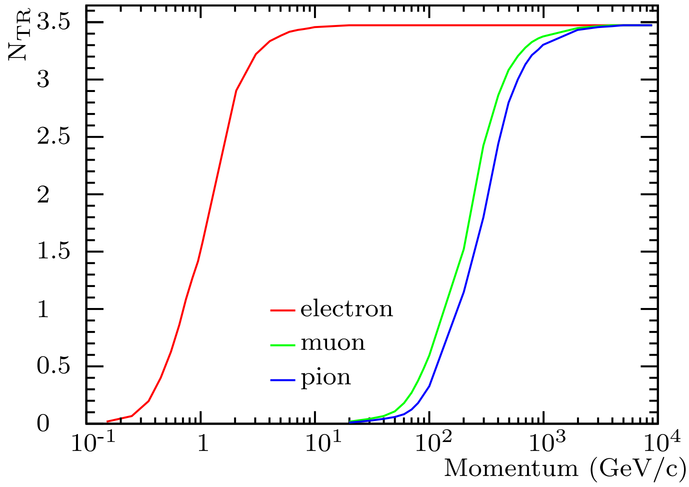

Figure 2.8.: Simulated TR yield of electrons, muons and pions depending on the particle momentum for a Polyethylene radiator with 200 layers, foil thickness $l_1 = 15\,\mu$m and foil spacing $l_2 = 750\,\mu$m [Ber14]

2.3.2. Transition Radiation for Particle Detection

Because of its small emission angle ($\theta \simeq 1/\gamma$) and strong γ-dependence, TR is very useful for particle detection. If a radiator is placed in front of a detector, a particle and its produced TR reach the detector basically at the same time and place, causing a different detector response than a particle which does not create TR. As stated in Section 2.3.1 the production depends threshold-like on γ, resulting in almost no TR produced by heavier particles at certain momenta where lighter particles already produce TR. As visualized in Figure 2.8, an electron passing through a radiator creates a significant amount of TR already at momenta more than 100 times smaller than muons and pions [Ber14].

2.4. Scintillation Detectors

Scintillation Detectors (SDs) are one of the most widely used radiation detectors due to their low complexity, response time and price. Generally they consist out of three parts: A scintillator, a light guide and a Photomultiplier (PMT), while a light guide might be optional depending on the shape of the scintillator. A schematic drawing of a scintillation detector is shown in Figure 2.9

A scintillator is a material with the property of luminescence, emitting light when being struck by ionizing radiation [Leo87]. There are different types of scintillators such as organic scintillators (i.e. organic crystals, organic liquids or plastics), inorganic crystal scintillators as well as gaseous or glass scintillators [Leo87]. Since for this thesis only plastic scintillators are of relevance the other types will not be discussed any further.

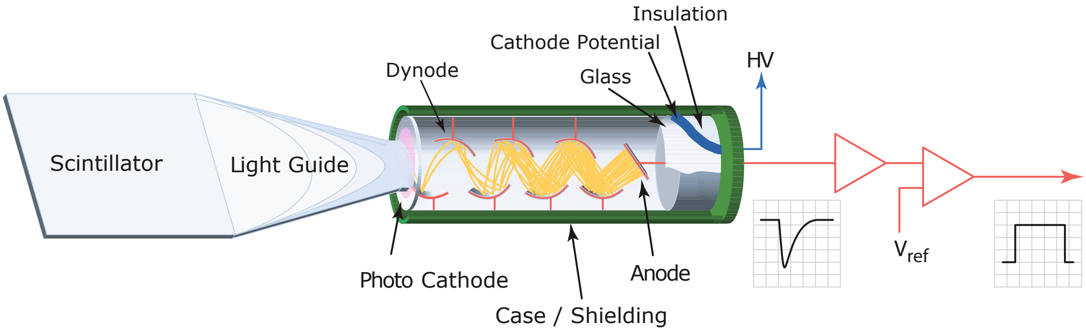

Figure 2.9.: Schematic setup of a scintillation detector consisting of scintillator, light guide, PMT and readout electronics [KW16] [edited]

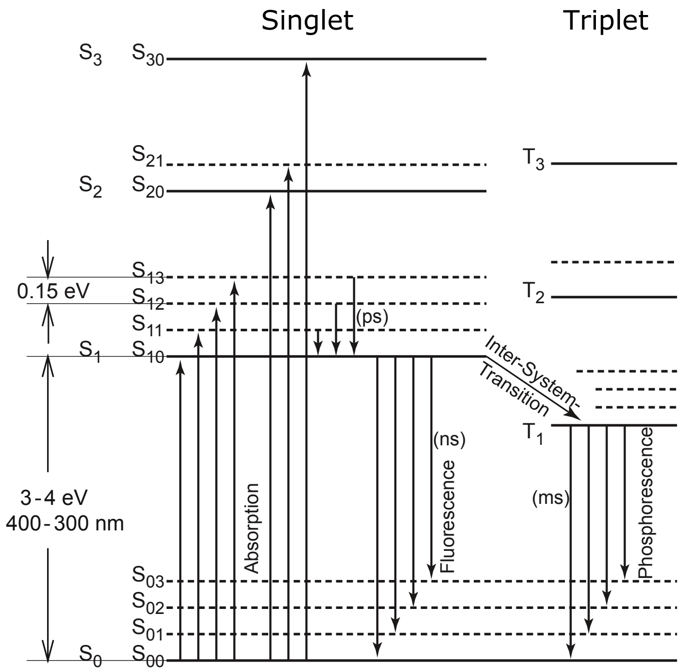

Figure 2.10.: Energy states of p orbital electrons in organic scintillators [KW16] [edited]

2.4.1. Plastic Scintillators

The scintillation process in plastic (as well as all other organic) scintillators utilizes electrons in the p orbitals of the benzene rings in the material. The orbits overlap so that none of these electrons are bound to a particular atom of the ring making the electrons *delocalized* [Leo87].

These electrons normally occupy the energetic ground state S_{00} (singlet). Energy deposited in the scintillator by an incident particle will excite the electrons

to higher energetic states (and vibrational modes) S_{1i}, S_{2i}, etc. which then decay in a very short time ($\leq 10\,\mathrm{ps}$) to the lowest excited state S_{10} via a radiationless process called *internal degradation* [Leo87]. This state S_{10} normally has a lifetime in the order of a few nanoseconds and subsequently decays through emission of a scintillation photon back into the ground state or, with a much higher probability, into the vibrational modes of the ground state. Since the energy gap between the excited state S_{10} and the vibrational modes of the ground state S_{0i} is smaller than the gap between the excited state and the ground state S_{00}, the scintillation photon does not possess enough energy to excite electrons from S_{00} to any excited state. Therefore, the scintillator is transparent to its own scintillation photons [Leo87]. This process is visualized in Figure 2.10.
Instead of decaying, the excited singlet states can also convert through so called *inter-system transitions* to excited triplet states T_{1i}. These triplet states will decay in a similar way as the singlet states first radiationless to T_{10} and then to S_{0i} trough emission of a scintillation photon. Since T_{10} is metastable, this process is much slower ($\sim$ ms) and therefore not useful for fast particle detection. Thus, in an ideal organic scintillation material, inter-system transitions are suppressed [KW16].
Because the energy gap between the ground and excited state is only a few eV wide, an incident particle will generally cause excitation of many electrons resulting in equally many scintillation photons. The number of emitted photons with a specific wavelength λ along the track of the particle can be quantified by the light output L [KW16]:

$$\frac{dL}{dx} = S\frac{dE}{dx}. \tag{2.12}$$

The proportionality factor S is called *scintillation efficiency*. Hence, the total number of scintillation photons is proportional to the total amount of energy deposited by the incident particle. Since the whole scintillation process relies only on molecular properties of the material, plastic scintillators can be used in various shapes and forms making them highly versatile in usage. With response times generally smaller than 5 ns they are also the fastest among scintillators while their light output and thus energy resolution is relatively low compared to other types like organic or anorganic crystal scintillators [Leo87].

2.4.2. Photomultipliers

To convert the photons emitted by the scintillator into an electrical signal, a PMT is used. Depending on the sizes of scintillator and PMT, a lightguide is placed between the two, making sure as many photons as possible reach the latter. On arrival at the PMT, a photon will hit a photocathode and release an electron through the photoelectric effect, which is then accelerated onto a dynode by an electrical field, ionizing atoms of the dynode. The secondary electrons are then accelerated to the next dynode, freeing more electrons. Important is that at every dynode level, a nearly constant factor of electrons is released per incident electron [KW16]. This process is visualized by the yellow lines in Figure 2.9. After the last dynode, the electrons will hit an anode where they can be measured as an electrical current. Typical PMTs contain 10 to 14 dynodes achieving total gains of 10^7 electrons per incident photon [Leo87]. Since the output current of the PMT I_{PMT} is proportional to the number of incoming scintillation photons N_γ it is also proportional to the amount energy deposited in the detector E_{particle} enabling energy-resolved particle detection:

$$E_{\mathrm{particle}} \propto N_\gamma \propto I_{\mathrm{PMT}}. \tag{2.13}$$

3. Experimental Setup

For testing purposes, the CBM-TRD prototypes were set up at a test beam facility at DESY, where measurements with electron beams at energies ranging from 1 to 4 GeV with different beam intensities were conducted. In this chapter, the experimental setup will be described, starting with the DESY II accelerator and the properties of the electron beam at the visited test beam site (Section 3.1). Afterwards, the used CBM-TRD prototypes themselves as well as the geometry of the overall setup will be shown (Section 3.2). Finally, the data acquisition methods will be discussed, explaining the readout electronics, self-trigger conditions, digitization and data format (Section 3.3).

3.1. DESY II Test Beam Facility

The research center DESY in Hamburg operates several particle accelerators and accelerator based experiments such as the *Doppel-Ring-Speicher* (DORIS), the *Positron-Elektron-Tandem-Ring-Anlage* (PETRA) or the DESY II synchrotron. The DESY II is a circular synchrotron with a circumference of 292.8 m, able to accelerate electrons or positrons to energies up to 7 GeV. It started operation in 1985 and nowadays serves mainly as an injector for DORIS and PETRA [D$^+$18]. Furthermore, it delivers its electron or positron beam to test beam facilities on the DESY campus, which are accessible to external users. At the test beam site T22 (see Figure 3.1) the CBM-TRD prototypes were set up and all measurements concerning this thesis have been recorded.

3.1.1. Beam Generation

The DESY II test beam sites do not receive the primary electron (or positron) beam accelerated in the synchrotron itself, but rather a secondary beam produced in additional steps. This enables the individual users to change various beam parameters such as momentum and intensity without having to alter the operation mode of the accelerator. The beam production process is sketched in Figure 3.1. In the DESY II synchrotron, an electron (or positron) bunch of about 10^{10} particles revolves around the ring with a revolution frequency of $f_\mathrm{r} \approx 1.025\,\mathrm{MHz}$ [D+18]. At three different positions, one per test beam area, a carbon fiber target can be moved into the beam line, causing electrons (or positrons) passing through it to emit bremsstrahlung (see Section 2.1.2). These photons will then hit a secondary target consisting of copper or aluminum and convert into electron-positron pairs. Because of the broad energy spectrum of bremsstrahlung, the electron-positron pairs will have an equally broad range of momenta. To separate these particles by charge and momentum, a dipole magnet is set up behind the secondary target spreading them out into a horizontal fan [D+18].

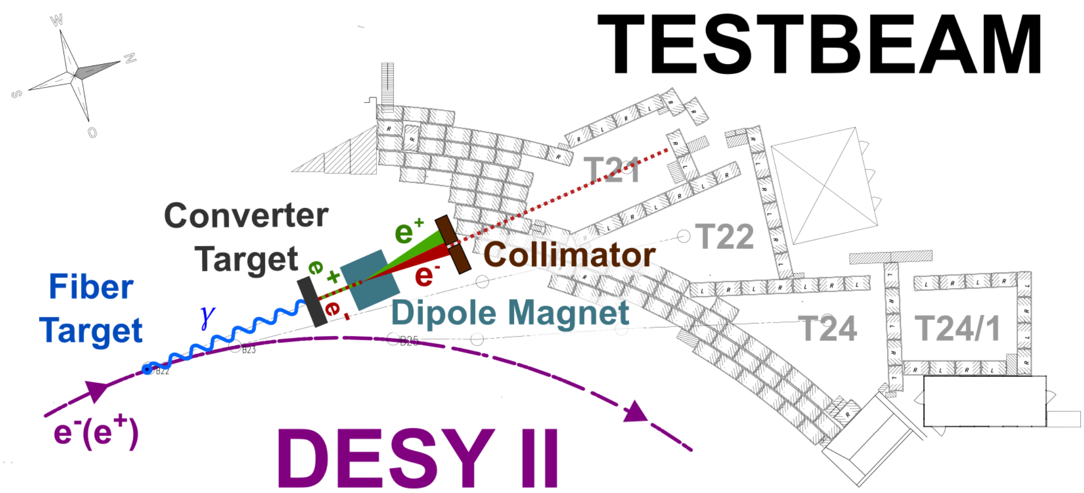

Figure 3.1.: Beam generation at DESY II test beam facility: The electrons (or positrons) accelerated in the DESY II hit a fiber target, emitting bremsstrahlung. The bremsstrahlung photons then convert into electron-positron pairs through a converter target which get spread out like a fan by a dipole magnet. By applying different magnetic field strengths it can be chosen which part of the fan (i.e. particles with which momentum) will pass through the primary collimator. The beam generation is only sketched for the experimental site T21 but works in the same way also for T22 and T24 [D+18].

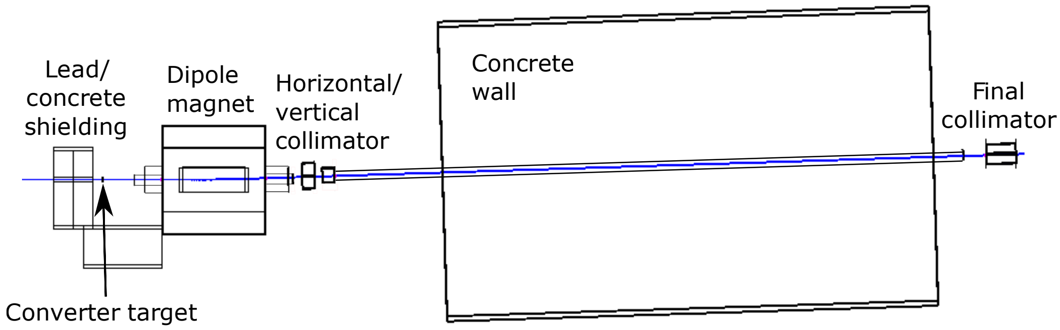

Figure 3.2.: Simulation of a charged particle traversing the beam pipe: Due to the small kink in the beam line, neutral particles hit the concrete wall because they are not deflected by the magnetic field. Furthermore, only charged particles with a specific momentum depending on the strength of the magnetic field will receive the correct curvature in their trajectory to pass through the beam pipe [D$^+$18][edited].

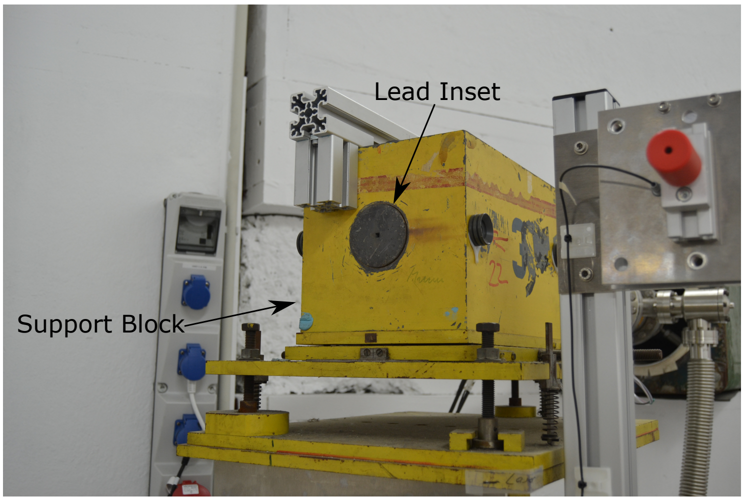

Figure 3.3.: Secondary collimator of the TB22 site: Lead insets with different aperture shapes and diameters can be inserted into the yellow support block (Photo: Florian Roether).

Neutral particles such as unconverted photons need to be separated from the beam before it reaches the test beam site. For this purpose, there is a small kink in the beam line behind the dipole magnet (Figure 3.2). As neutral particles do not undergo a change in trajectory due to the magnetic field, they continue their straight path and hit a concrete wall [D$^+$18]. The trajectory of the electrons and positrons on the other hand will undergo a slight curvature, with the radius of curve depending on charge and momentum of the electron/positron as well as the strength of the magnetic field. Hence, applying different magnetic field strengths will result in particles with different momenta being able to pass through the beam pipe, enabling momentum selection by the user. By changing the polarity of the magnetic field, it is possible to choose between electrons and positrons. [D+18].

The secondary electron/positron beam can be collimated with two different collimators: The primary collimator consists of a horizontal and a vertical tungsten jaw, which both are individually controllable by the user, and is positioned directly behind the dipole magnet which is used for momentum selection (Figure 3.2). On the test beam site itself, behind the end of the beam pipe, a secondary collimator is located where one of several lead insets with different apertures ranging from $5\,\mathrm{mm} \times 5\,\mathrm{mm}$ to $20\,\mathrm{mm} \times 20\,\mathrm{mm}$ can be inserted into a support block (Figure 3.3) [D+18].

3.1.2. Timing Structure

The beam entering the test beam area is not a continuous, steady stream of electrons but varies in intensity over time based on three different cycles. At first, the finite revolution frequency of the electron bunch itself in the synchrotron has to be taken into account. The secondary beam is generated only when the electron bunch hits the fiber target, which happens once every $0.976\,\mu\mathrm{s}$ $\equiv (1.025\,\mathrm{MHz})^{-1}$. However, not every bunch cycle results in a particle reaching the test beam area. Therefore, while two incoming electrons being just $0.976\,\mu\mathrm{s}$ apart is possible, the mean frequency is much lower, generally in the order of a few kHz (see Section 3.1.3), which itself is quantized by the revolution frequency [D+18]. Theoretically, also two secondary electrons resulting from a single collision of the primary electron bunch with the fiber target can occur, but with a negligible probability of about $0.6\,\%$ even at a selected momentum of $2\,\mathrm{GeV}/c$, at which the rate is generally the highest (see Section 3.1.3) [D+18].

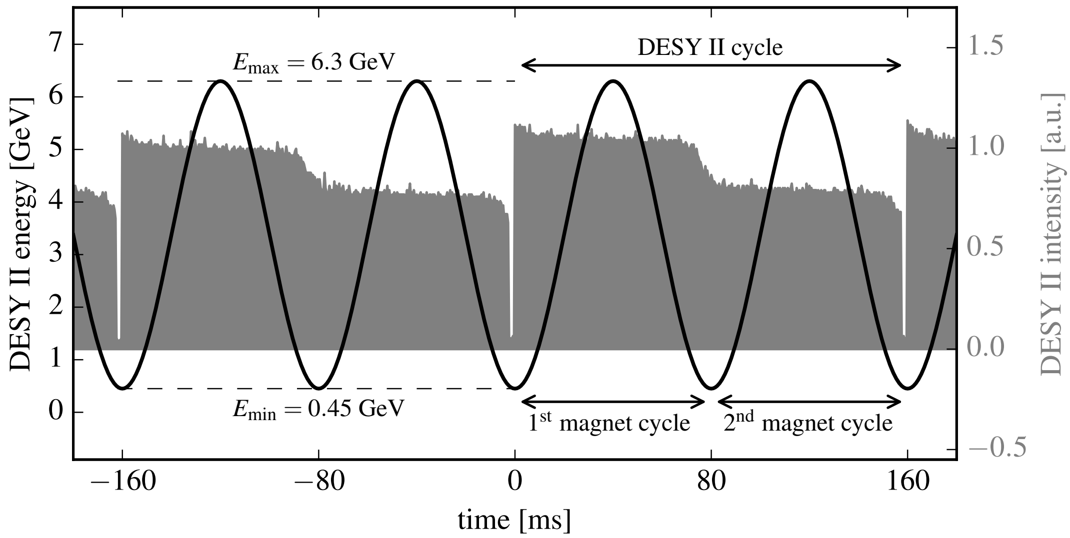

Figure 3.4.: DESY II magnet cycle: Schematic representation of the beam energy (black) increasing and decreasing sinusodially from 0.45 GeV to 6.3 GeV. The beam intensity (grey) decreases every second magnet cycle because of higher beam loss at lower energies [D+18].

Secondly, the DESY II magnet cycle has to be considered. The electrons inside the synchrotron do not revolve with a constant energy, but get accelerated and decelerated sinusodially by magnets with a frequency of $f_m = 12.5\,\mathrm{Hz} \equiv (80\,\mathrm{ms})^{-1}$, with the lowest energy being $E_{\min} = 0.45\,\mathrm{GeV}$ and the highest $E_{\min} = 6.3\,\mathrm{GeV}$ (Figure 3.4) [D+18]. At times in which the primary beam energy is lower than the desired secondary beam energy, the particle rate in the test beam area will be zero. Therefore, the electron spills reaching the area are shorter for a higher the momentum selected by the user [D+18].
Finally, there is the so called "PETRA III top-up", in which electrons revolving inside the DESY II are injected into the PETRA III storage ring, causing a decrease in DESY II beam intensity and thus less (or almost no) secondary beam for a few seconds. The injections can reoccur with times ranging from every 30 s to a few minutes depending on the operation mode of PETRA III [D+18].

3.1.3. Expected Frequency

The final rate of particles arriving at the test beam area depends on many factors along the particles generation process such as DESY II beam intensity, primary and secondary target properties, desired particle momentum and collimator settings. As can be seen in Figure 3.5, the test beam rate increases almost linearly with the intensity of the DESY II beam. This dependence simply is due to the fact that an increased number of electrons in the primary beam leads to a higher interaction rate at the primary target [D+18].

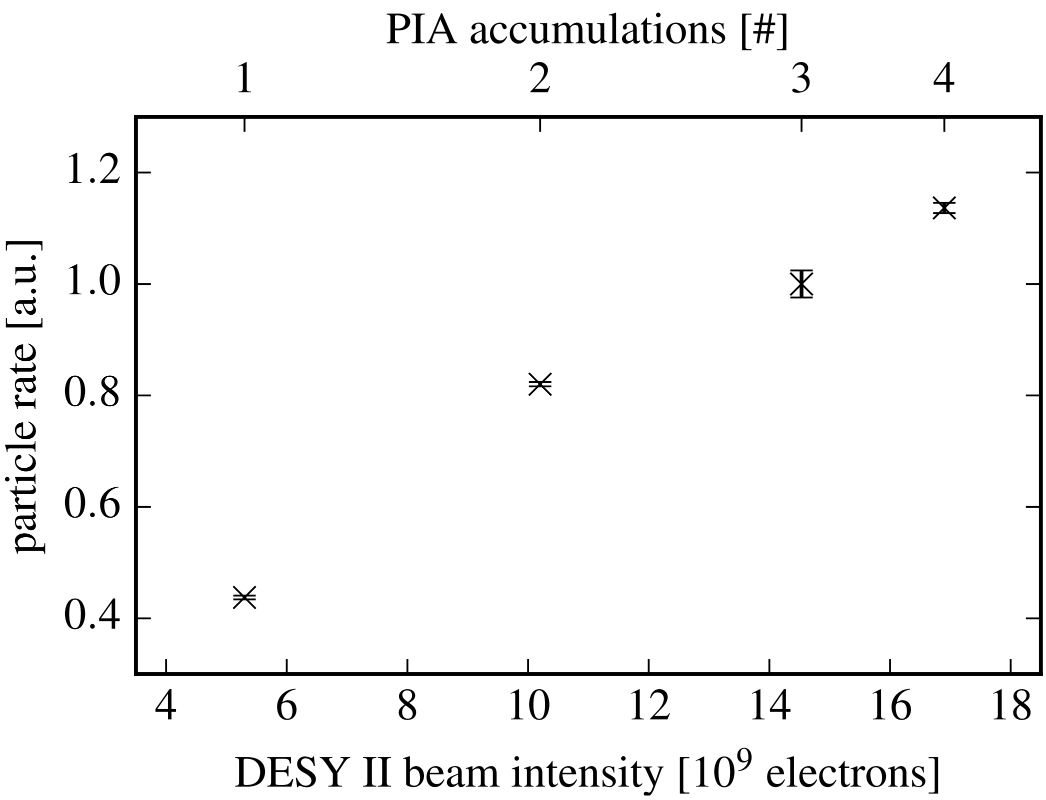

Figure 3.5.: Rate of test beam particles reaching site T22 (see Figure 3.1) depending on DESY II beam intensity. The increased intensity was achieved by accumulating several electron bunches with the storage ring PIA, the number of bunches accumulated can be seen on the upper X-axis [D$^+$18].

Similarly, the position of the primary target has an effect on the particle rate: Moving the target further into the DESY II beam results in a larger collision cross section, creating more bremsstrahlung and thus secondary beam of higher intensity. In Figure 3.6 the particle rates at the three test beam sites depending on the position of their respective primary target are shown, which can equivalently be seen as the DESY II beam profile. The difference between the beam profiles of the individual test beam sites is caused by a broadening of the electron bunch in the synchrotron after passing through the first primary target [D$^+$18].

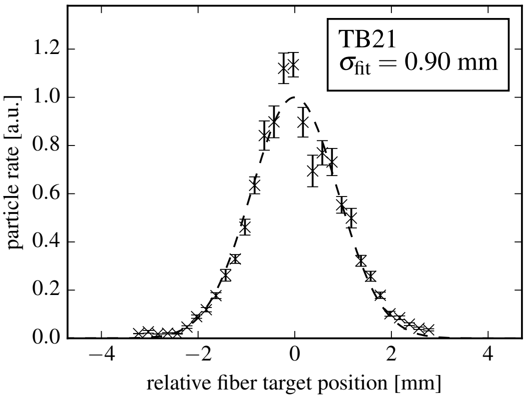

(a) at TB21

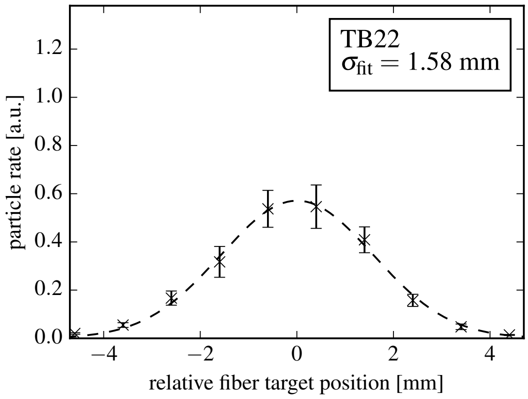

(b) at TB22

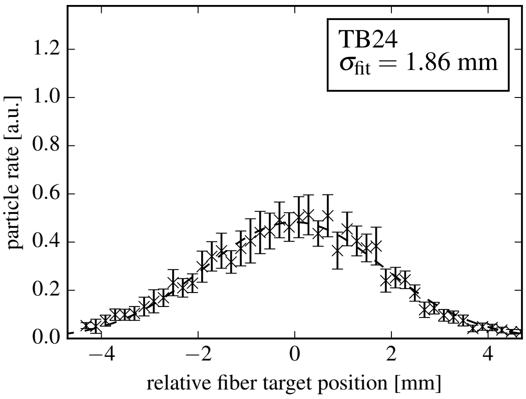

(c) at TB24

Figure 3.6.: Particle rates at the three test beam sites depending on the position of the primary target. Each distribution is normalized by the integral of the TB21 distribution making them comparable to each other [D+18].

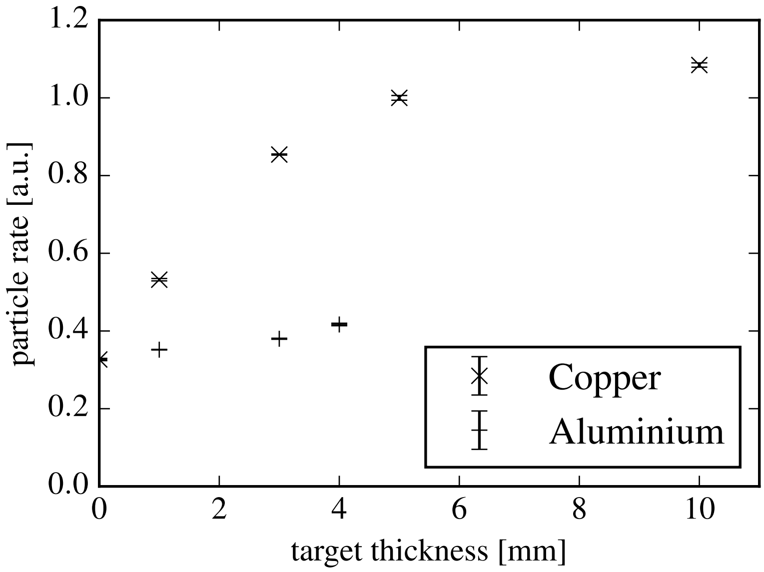

Figure 3.7.: Dependence of the particle rate on secondary target material and thickness. Because of its higher Z copper targets have a higher probability of converting a bremsstrahlung photon into an electron-positron pair thus resulting in more particles at the test beam site. A thicker target will also have an increased conversion probability since the photon has to travel along a longer path through it. An increased thickness will also result in scattering processes widening the radiation angle of the electron-positron pairs which decreases the proportion of created particles staying in the beam line. This results in the visible saturation at higher target thicknesses [D$^+$18].

The available secondary targets are either made out of copper or aluminum and come in several different thicknesses. Since the probability for pair production scales with the square of the atomic number of the surrounding material (see Section 2.1.3), copper targets generally produce more electron-positron pairs than aluminum targets with the same thickness. Naturally, the conversion probability also increases with the target thickness. But as scattering increases in thicker material, the radiation angle widens, resulting in a saturation of the particle rate, as shown in Figure 3.7 [D$^+$18].
The desired particle momentum selected by the user also has a strong impact on the rate. Since the bremsstrahlung spectrum decreases for higher energies, also the amount of created electron-positron pairs and hence the particle rate is lower at higher selected momenta (Figure 3.8). Even though many more bremsstrahlung photons with low energies are created, there is also increased scattering causing a reduced rate at low momenta. These two effects result in a maximum rate at a selected momentum of $2\,\mathrm{GeV}/c$ [D$^+$18].

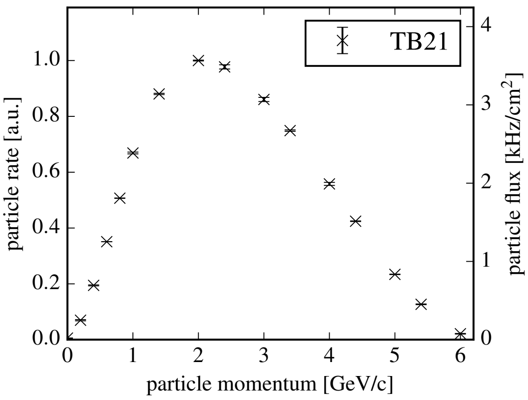

(a) at TB21

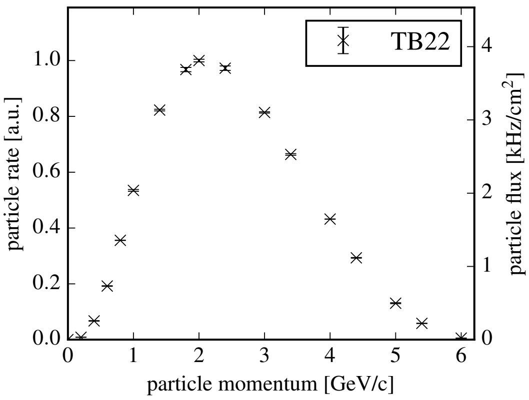

(b) at TB22

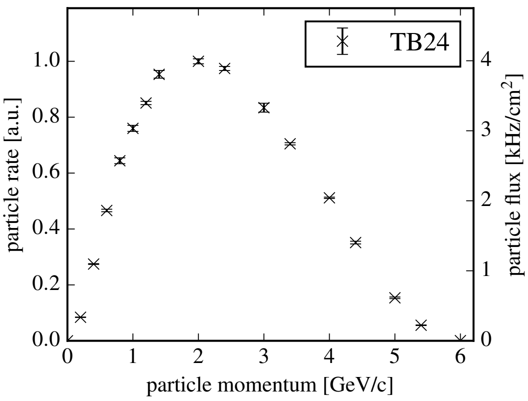

(c) at TB24

Figure 3.8.: Particle rate dependence on the selected momentum [D$^+$18].

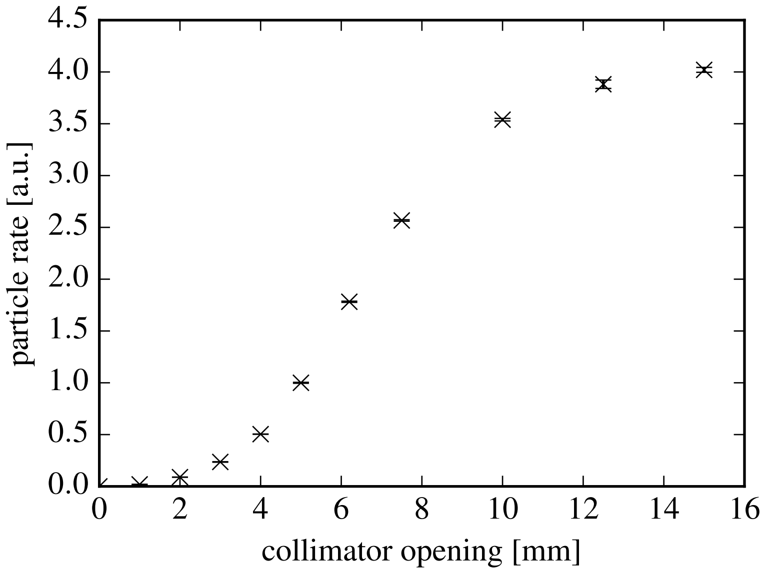

Figure 3.9.: Particle rate dependence on the primary collimator opening: The collimator was opened symmetrically in X- and Y-direction [D+18].

Finally, also the collimator openings have an impact on the particle rate. In Figure 3.9 the rate dependence on the opening of the primary collimator is shown. Evidently, the rate increases for wider openings as a larger part of the beam can pass the collimator. Since the beam has a finite width the particle rate saturates for very wide openings [D+18]. For the secondary collimator no data is available but a similar behaviour is expected.

3.1.4. Beam Profile

The profile of the final particle beam entering the test beam area depends mostly on the collimator settings and the beam momentum. For a detector setup, also the distance between the collimator and the detector is important, as the beam spread increases over its path due to scattering with air molecules. Measured beam widths in X and Y direction for different collimator settings can be seen in Figure 3.10. In the upper panel it can be seen that the beam is asymmetrical with respect to X and Y direction, with a wider profile in the horizontal plane. As the collimation increases in the middle and lower panel, this effect becomes less visible.
At lower momenta the beam width increases due of increased scattering, which can be seen in Figure 3.11.

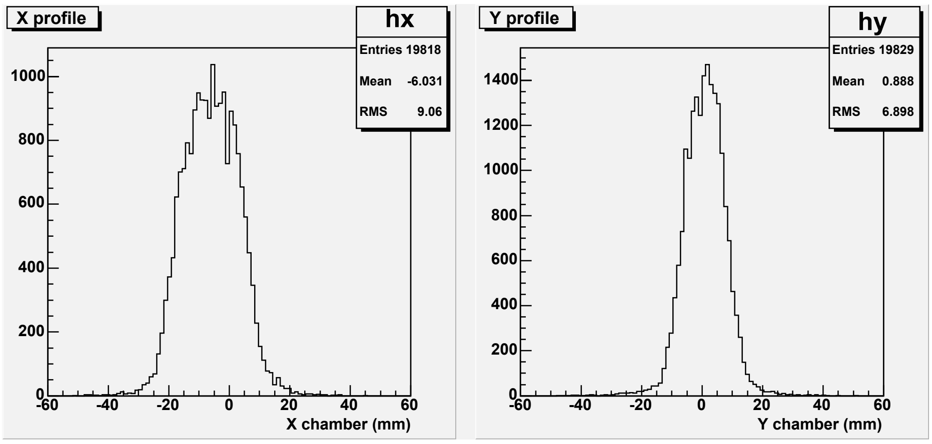

(a) 10 mm × 10 mm Collimator Opening

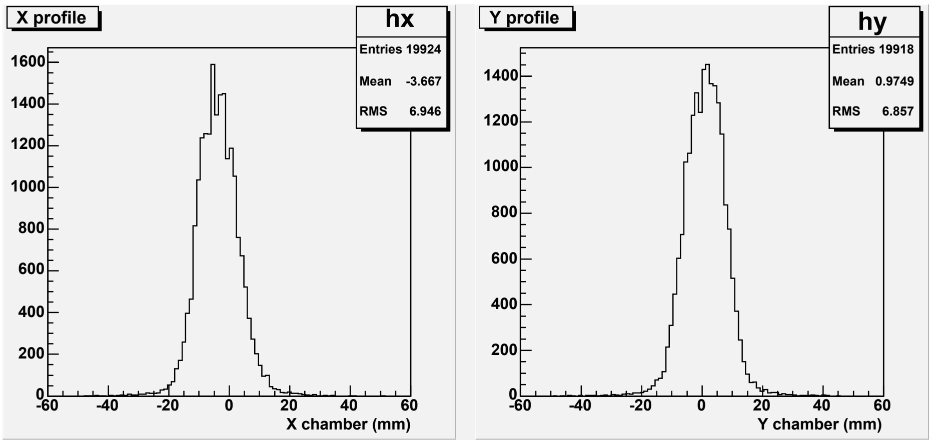

(b) 5 mm × 5 mm Collimator Opening

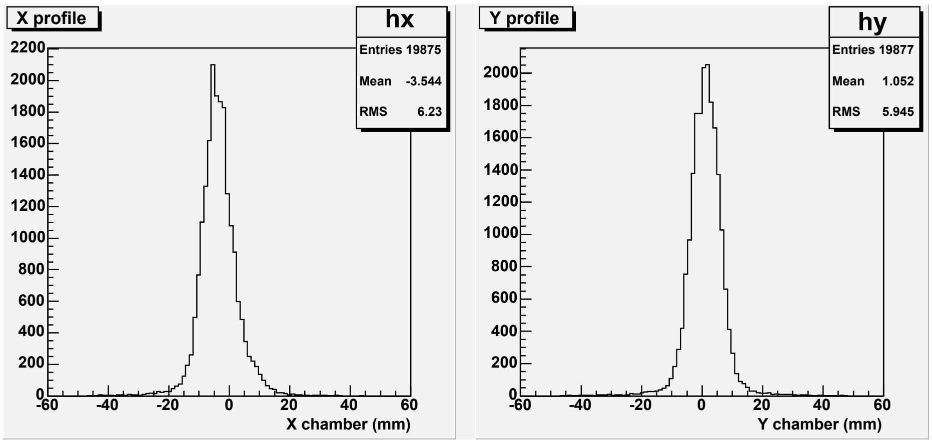

(c) 2.5 mm × 2.5 mm Collimator Opening

Figure 3.10.: Measured beam profiles in X and Y direction for different collimator openings: All profiles are measured at a beam momentum of 6 GeV/c. As can be seen in the upper panel, the beam is not symmetrical in X and Y direction but generally wider in X. This effect is less pronounced for narrower collimator openings [ACE+05].

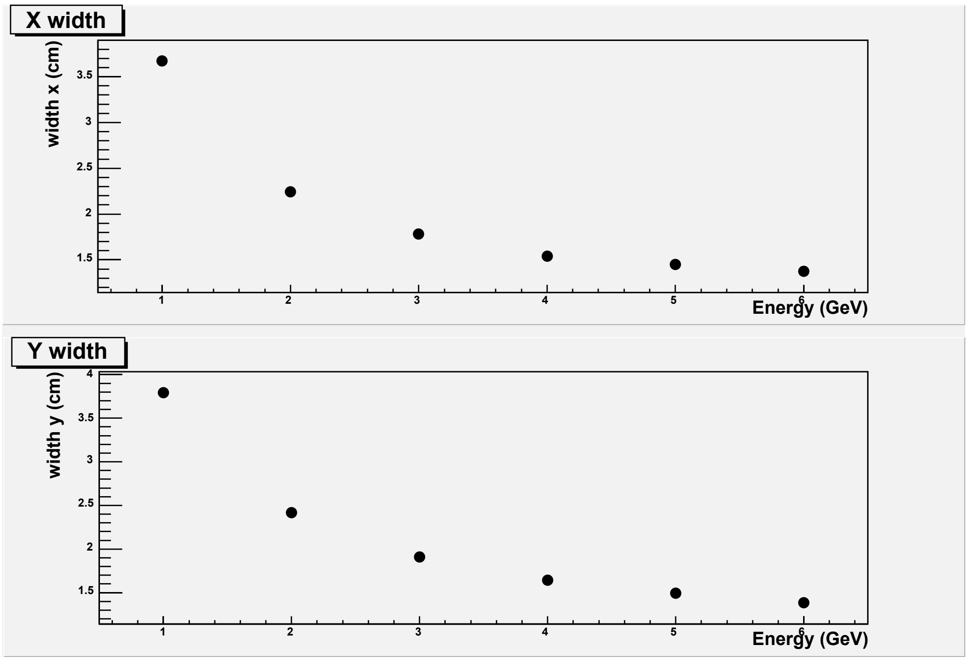

Figure 3.11.: Measured beam widths at different beam energies, obtained with a collimator opening of 5 mm × 5 mm: The width decreases in both directions with increasing energy [ACE+05].

3.2. Detector Attributes and Setup

At the DESY test beam site T22, four 2015-type CBM-TRD prototypes, two 2012-type CBM-TRD prototypes and two scintillation detectors have been set up (Figure 3.12). A more close up photo of the SDs can be found in Figure A.1. As this thesis is focused on the efficiency determination of the 2015-type prototypes in combination with the readout electronics, the 2012-type detectors are omitted in the following.

3.2.1. Used CBM-TRD Prototypes

Each of the four 2015-type CBM-TRD prototypes consists of a MWPC and a radiator, both having the outer dimensions of 96×96 cm. The MWPCs have a total thickness of 5 cm and consist of several layers, which can be seen in Figure 3.14. An incident particle will enter the chamber through a 25 μm thick Kapton foil entrance window and get into the active, gas filled detector area, which is composed of a drift region and an amplification region, as described in Section 2.2. The parameters of the wire spacing can be found in Figure 3.13.
The pad plane is divided into 768 equally sized cathode pads, each being 15.25 cm long and 0.72 cm wide. A to scale drawing can be found in Figure 3.15. The direction of the smaller separations is generally to referred as "columns", while the direction of large separations is referred to as "rows", independent of its

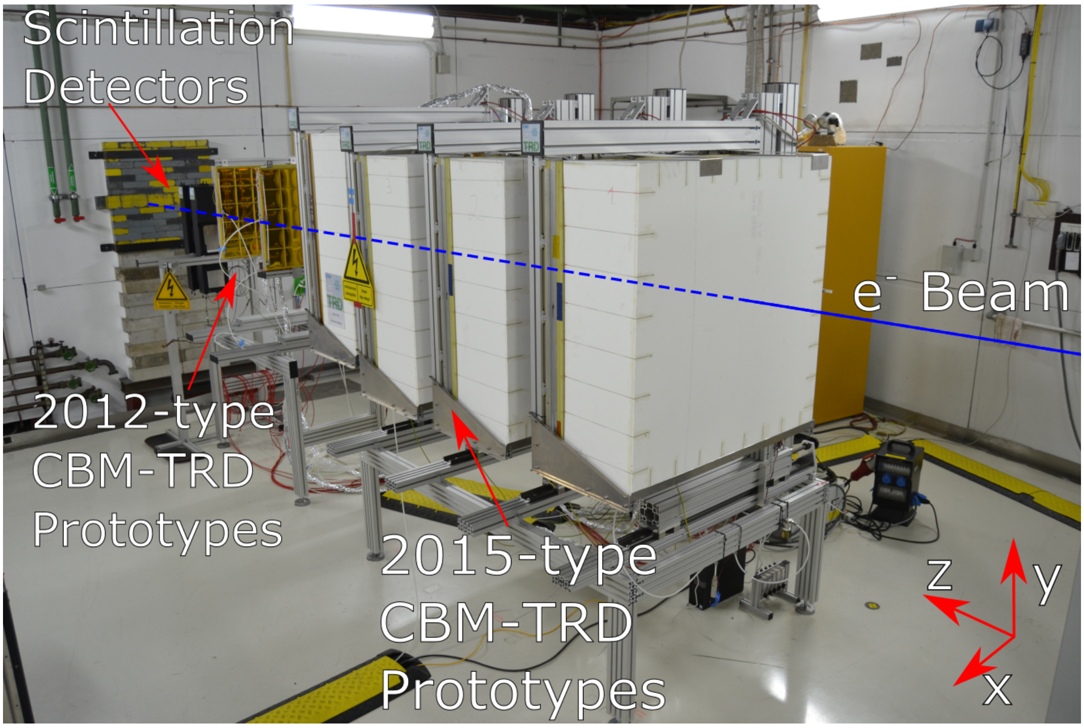

Figure 3.12.: Detector setup used at the test beam: First in the beam line are four 2015-type CBM-TRD prototypes, followed by two 2012-type CBM-TRD prototypes. Right in front of the beam dump two scintillation detectors are setup. In this photo, radiators (white boxes) are mounted in front of every 2015-type prototype (Photo: Florian Roether).

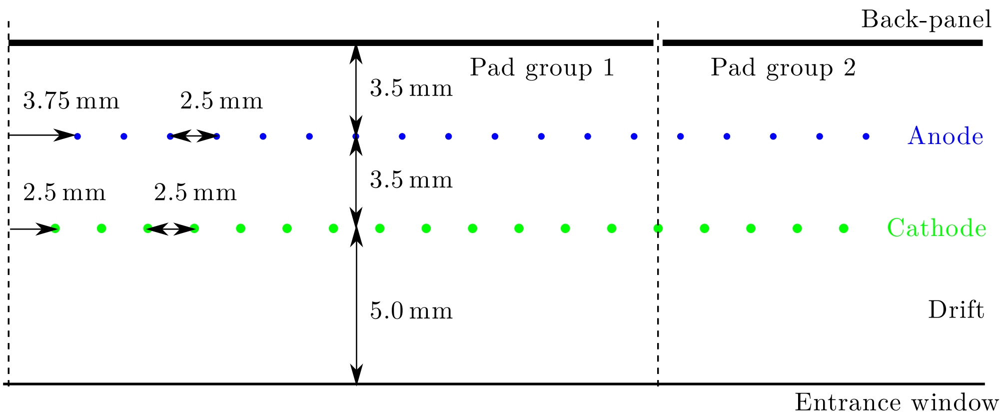

Figure 3.13.: Parameters of the drift and amplification region in the used CBM-TRD prototypes [CBM18].

orientation. Hence, the pad plane sketched in Figure 3.15 is divided into 128 columns and 6 rows. Due to the small expected beam width (see Section 3.1.4), the chambers were only partly equipped with readout electronics during the test beam, reading out 32 pads per detector in a rectangular shape, signified by the green box in Figure 3.15. Due to the pad shape, a high position resolution can be obtained only in one direction per detector. For this reason, the fourth chamber was rotated by 90°, which is slightly visible in Figure 3.12. As a chamber gas a mixture of 80% Xe as the active component and 20% CO_2 as the quenching gas was chosen [CBM18]. As a chamber gas a mixture of 80% Xe as the active component and 20% CO_2 as the quenching gas was chosen [CBM18].
The radiators consist of a Rohacell HF71 box, which is filled with 146 layers of PolyEthylene (PE) foam foils, each with a thickness of about 2 mm. As the box not closed at the front side, a polymer filament grid was added to stabilize the shape of the radiator (see right panel of Figure 3.16). Together with the 8 mm back wall of the Rohacell box, the total thickness of each radiator amounts to 30 cm.

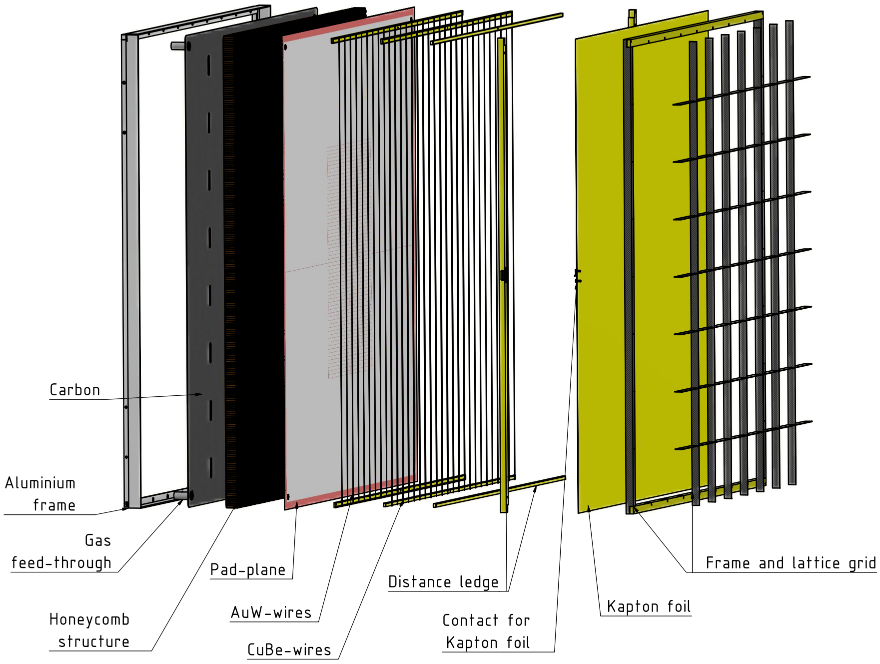

Figure 3.14.: Explosion view of the used MWPCs: [CBM18]

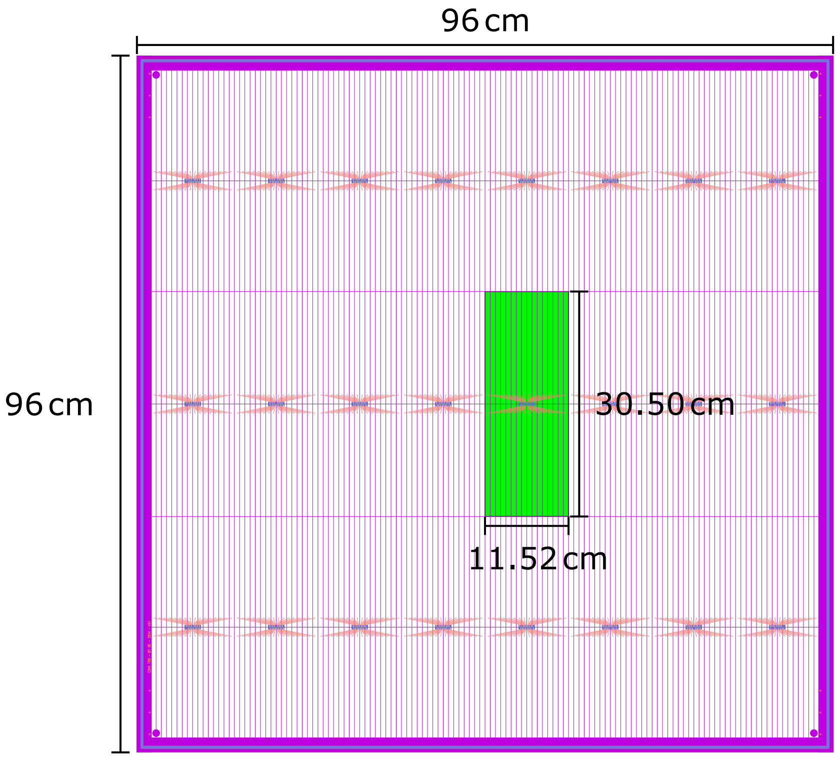

Figure 3.15.: Technical drawing of the padplane: Every block of 32 pads is connected to one SPADIC readout chip (see Section 3.3). The green rectangle represents the size of the active area for the conducted measurements. [Ems] [Drawing: David Emschermann, edited]

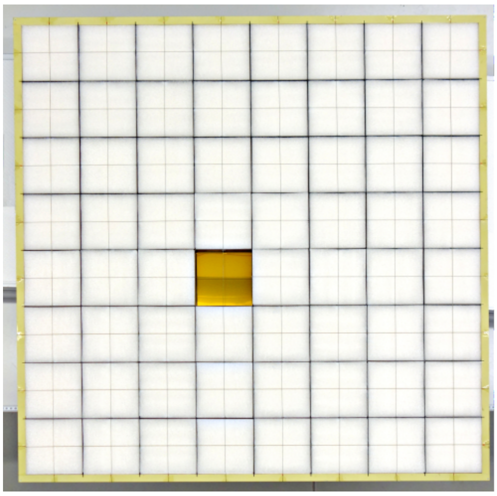

Figure 3.16.: Left: Photo of the small PE foam foils inserted into the carbon lattice grid of the MWPC. For test measurements, one cell of the grid was left free. Right: Photo of one of the used radiators, consisting of the Rohacell box filled with PE foam foils, which are held in position by the polymer filament [CBM18].

3.2.2. Used Scintillation Detectors

Two identical SDs were used, each consisting of a scintillator, a light guide and a PMT. The two scintillators BC-408 by Bicron are made out of Polyvinyl Toluene (PVT), an organic, synthetic polymer and have the outer dimensions of 160 mm × 240 mm × 10 mm. Their most important properties can be found in Table 3.1. The two PMTs which have been used are the type R2154-02 PMTs by Hamamatsu. Their properties can be seen in Table 3.2.

Table 3.1.: Most important features of the used scintillators: The rise and decay time are defined as the time, in which the pulse rises from 10 % of its amplitude to its maximum, and vice versa. All values have been taken from [Bic].

Light Output (Compared to Antracene)	64 %
Wavelength of Max. Emission	425 nm
Rise Time	0.9 ns
Decay Time	2.1 ns
Pulse Width (FWHM)	$\sim$ 2.5 ns

Table 3.2.: Most important properties of the used PMTs: The rise time ist defined as the time, in which the pulse rises from 10 % of its amplitude to its maximum. All values are taken from [Ham].

Spectral Response	300 nm to 650 nm
Wavelength of Maximum Response	420 nm
Photocathode Material	Bialkali
Number of Dynode Stages	10
Maximum Supply Voltage	1750 V
Gain (at 1250 V)	1.0×10^6
Rise Time	3.4 ns
Pulse Width (FWHM)	3.6 ns

3.2.3. Geometry of the Setup

The setup of the detectors including their respective distances is sketched in Figure 3.17. Full, to scale drawings of the active detector areas in both the XY- and XZ-plane can be found in Figure A.2 and A.3. When setting up the detectors, the active areas of the first three TRDs have been aligned as much as possible. Their positions with respect to the beam has been chosen in a way that the beam will not hit the border between two pad rows. The last TRD, which was rotated by 90°, and the SDs were positioned so that they would be hit central. A drawing of the overlaps of the active areas can be seen in Figure 3.18.

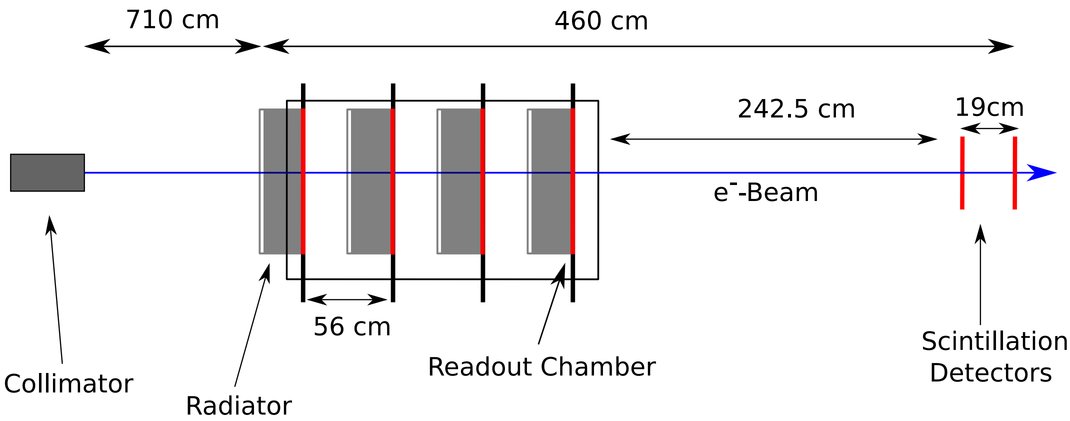

Figure 3.17.: Sketch of the detectors used for this thesis with their respective distances: This sketch is not to scale [Fid][edited].

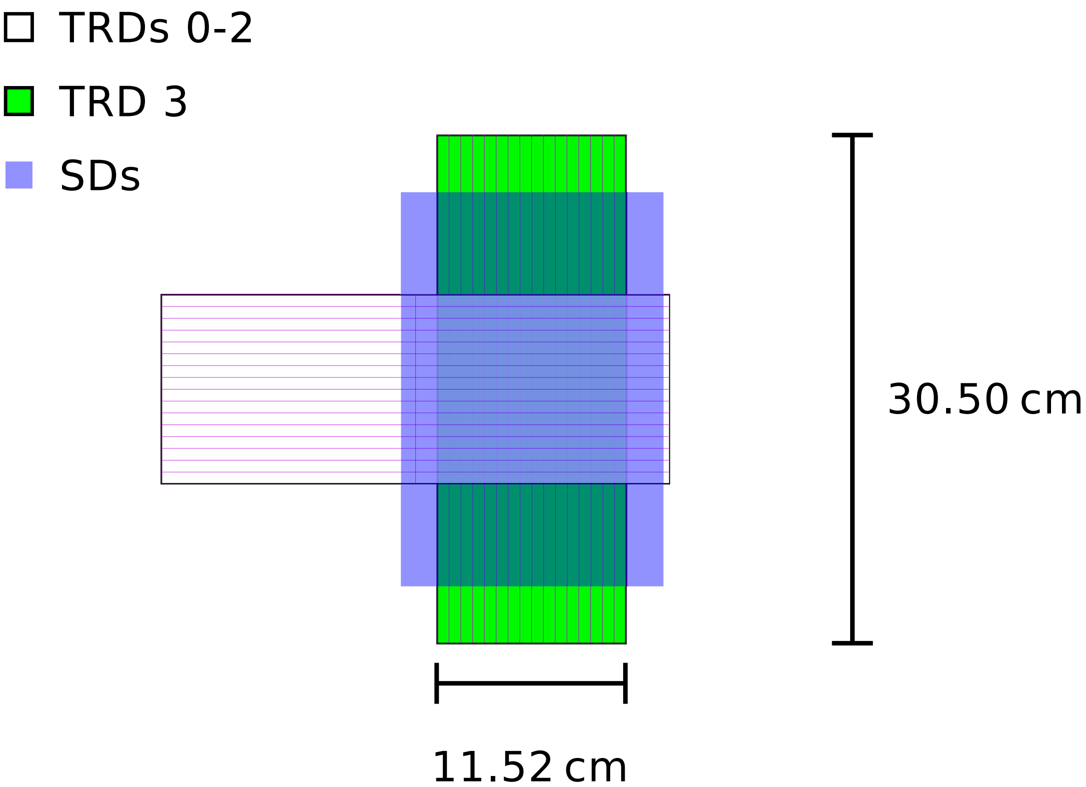

Figure 3.18.: Sketch of the overlap of the active areas of TRDs 0-2 and TRD 3 (to scale).

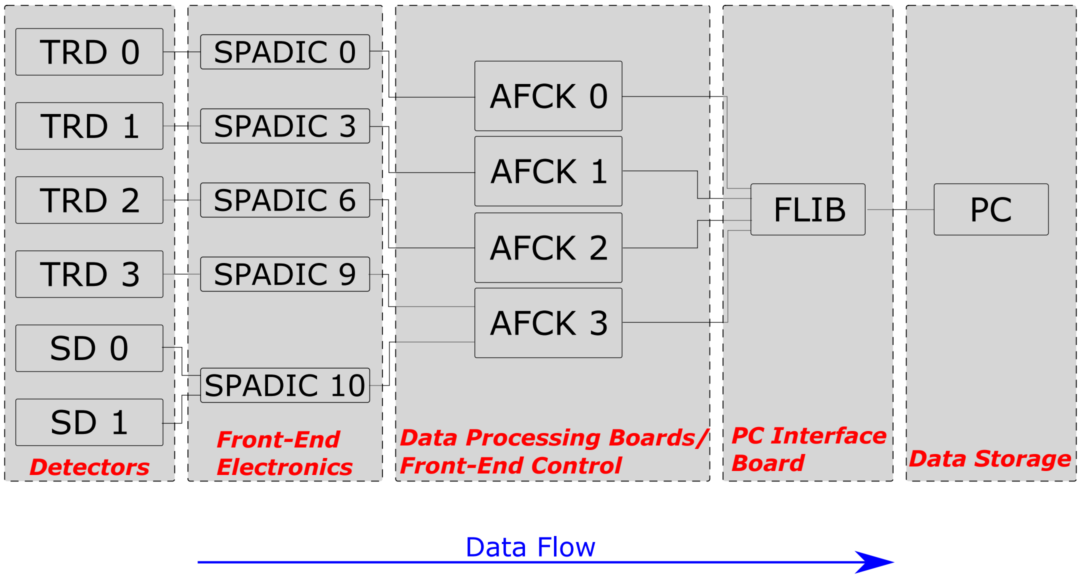

Figure 3.19.: Schematic drawing of the detectors and readout electronics used at the test beam: The charge pulses from the detectors are delivered to the SPADIC readout chips where they are amplified and digitized. The streams of digital data from up to three SPADICs are then passed on by the AFCKs to the FLIB, where they are stored in packages (timeslices) and finally saved as a TSA file on the PC.

3.3. Data Acquisition

All detectors were read out using the Self-triggered Pulse Amplification and Digitisation as IC (SPADIC) 2.0 readout chip, an integrated circuit that amplifies and continuously samples incoming charge signals. Most importantly, its build-in trigger logic allows a signal selection without the need for an external trigger (see Section 3.3.1). The digitized signal from the SPADIC is then sent to a data processing board called AMC FMC Carrier Kintex (AFCK). Here, signals from up to three SPADICs are passed on to the FLES Interface Board (FLIB). The FLIB is a PC interface board that stores the incoming data from the AFCKs into data containers with a fixed length. These containers are called *timeslices* and have a length of 0.1024 s. Finally, the timeslices are saved as a Timeslice Archive (TSA) file on the PC. The whole readout chain is sketched in Figure 3.19.

3.3.1. Detector Readout and Triggering

Each SPADIC has 32 individual readout channels, which are divided in groups of 16 over two half chips, thus being able to read out 32 detector pads simultaneously. Every channel consists of four main parts: A Charge Sensitive

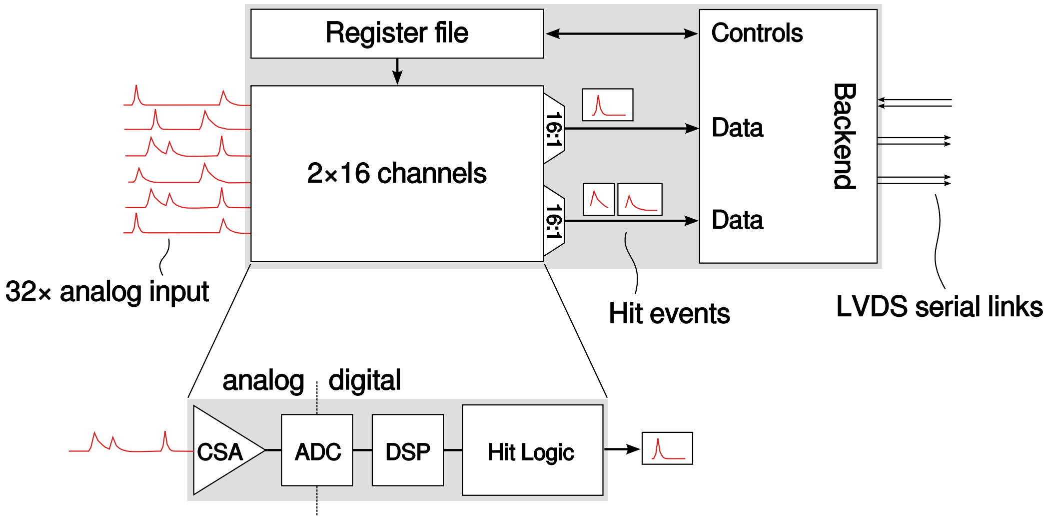

Figure 3.20.: Block diagram of the SPADIC: 32 channels are divided on two 16 channel half chips, while each channel consists of CSA, ADC, DSP and hit logic [CBM18].

Amplifier (CSA), an Analog to Digital Converter (ADC), a Digital Signal Processor (DSP) and the hit logic, as is sketched in Figure 3.20.

The general readout process works as follows: An incoming charge signal will first be amplified by the CSA's preamplifier. The CSA's integrated shaper will then release a voltage pulse of the form:

$$V_s(t) = A \cdot \frac{t}{\tau} \cdot \exp\left(-\frac{t}{\tau}\right) \qquad (\text{for } t \geq 0) \tag{3.1}$$

with a shaping time of $\tau = 240\,\text{ns}$ [CBM18]. The amplitude A of this pulse depends on the total charge of the initial signal. The voltage pulse is then converted into a current by a resistance and subsequently digitized by the ADC, which is continuously sampling the incoming current with a rate of 16 MHz, resulting in each sample having a length of 62.5 ns. The ADC itself has a range of 9 bit, and hence outputs values between -256 and 255 [CBM18]. In the DSP, additional filtering or scaling of the digital signal can be performed. To keep the readout process as simple as possible, this feature was disabled during the testbeam campaign at DESY.

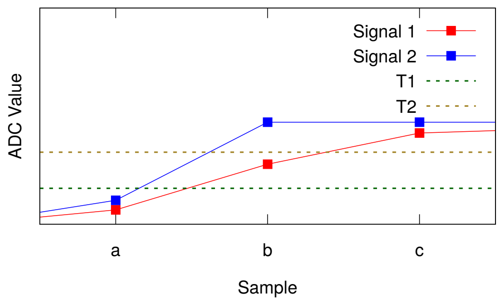

(a) $a \leq T_1, b > T_1, c > T_2$

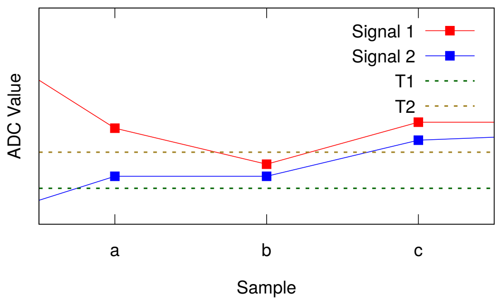

(b) $b \leq T_2, b > T_1, c > T_2$

Figure 3.21.: Sketch of four different sets of samples fulfilling the trigger condition: In the left panel, the first part of the "OR" condition in Equation 3.2 is fulfilled, in the right panel the second part.

Finally, the signal reaches the hit logic, where it is decided, wether it will be passed on and recorded or not. This is done by continuously checking the following trigger condition for three subsequent ADC samples a, b and c and two programmable threshold values T_1 and T_2 [MA16]:

$$t = [(a \leq T_1) \vee (b \leq T_2)] \wedge (b > T_1) \wedge (c > T_2) \tag{3.2}$$

Examples of signals fulfilling this condition can be seen in Figure 3.21. When the trigger condition is fulfilled, the transmission of 32 ADC samples together with data containing additional information (see below) as a so called "hit message" is triggered. These 32 samples include the two samples before of the trigger samples, the trigger samples themselves, and the 27 subsequent samples. Since all channels are readout in parallel while each half SPADIC has only one uplink to the AFCK, the hit messages are first stored in an individual buffer for each channel. The so called "channel switch" then choses one message after the other in the order of their creation and sends it to the AFCK. This is sketched in Figure 3.22.

3.3.2. Forced Neighbor Readout and Multihits

Two additional features of the SPADIC's selftriggered readout are worth mentioning. First, there is the so called Forced Neighbor Readout (FNR). When the signal on one cathode pad is high enough to fulfill the trigger condition, both neighboring pads are also read out, even if they do not fulfill the condition, since knowledge about the charge distribution over adjacent pads enhances the position resolution. In the meta data of the hit message it is flagged, if a signal triggered the readout on its own, by FNR or both at the same time.
Secondly, it is also possible that a signal, before reaching the 32nd sample, will fall below the thresholds, rise again due to a new charge deposition and thus trigger another readout, while the initial hit message was not yet completed.

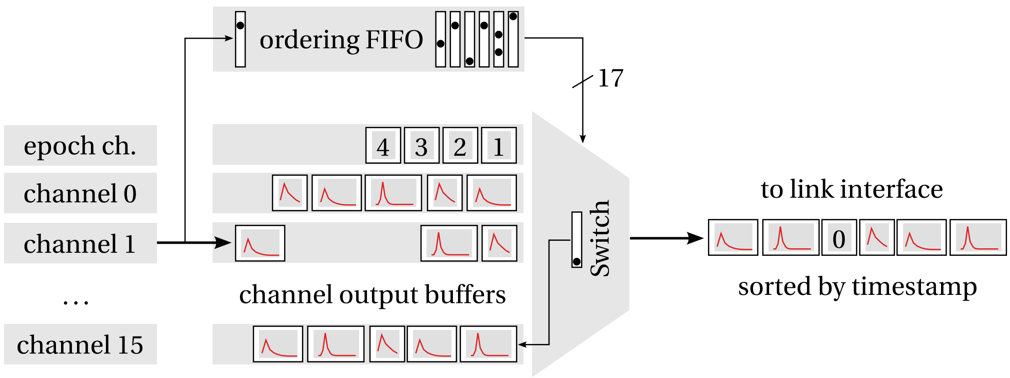

Figure 3.22.: Schematic drawing of the SPADIC's working principle between each channel output and the single uplink (per half chip) to the AFCK: The hit messages from each channel are buffered in individual channel buffers and then transmitted to the AFCK one by one in the order of their creation [Kri18].

This case is called a *multihit scenario*. When a multihit occurs, the SPADIC ends the transmission of the initial hit message and flags it as "interrupted by multihit", before beginning a new hit message at the time of the second trigger, which will as usual last 32 samples.

3.3.3. Meta Data

In addition to the sampled ADC values, each hit message contains information about time, place and conditions of its triggered readout, which is listed below [Arm13]:

- Group & Channel ID: Number of the half chip and channel of the hit message
- Timestamp: 12 bit time information
- Triggertype: Value between 0 and 3 signifying how the readout of the hit message was triggered. The triggertypes are:

    0: Triggered by machine trigger signal

    1: Selftriggered readout

    2: Triggered by FNR

    3: Selftriggered and FNR simultanously

- Stoptype: Value between 0 and 5 signifying how the readout of the hit message has ended. The stoptypes are:

    0: Normal end of the hit message

1: Aborted because the message output buffer was full

2: Aborted because the ordering FIFO was full

3: Multihit: The next hit message was triggered before the current one was finished

4: Output buffer was full, multihit detected simultaneously

5: Ordering FIFO was full, multihit detected simultaneously

- Number of Samples: Number of transmitted ADC samples

As stated above, the Time Stamp (TS) is a 12 bit value containing the time information about the triggering of a hit message, thus being able to take values from 0 to 4095. As each ADC sample needs its own TS and has the length of 62.5 ns, this value is only unique for 0.256 ms. Therefore, so called epoch markers and super epoch markers were introduced. Everytime the TS moves from 4095 back to 0, the SPADIC sends out one epoch message, which itself contains a 12 bit value with the number of the epoch. Subsequently, when the number of epoch moves from 4095 back to 0, a super epoch message is emitted. With these two additional 9 bit values and the 9 bit TS, the time information is unique for about 4295 s (≈ 1.2 h).

3.3.4. Data Loss in Channel Switch

There is a known issue in the channel switch of the SPADIC 2.0, which can lead to the loss of parts of a hit message [Kri18]. Because the analyis of the data relies on the specific structure of the SPADIC's messages, the ones which are missing a part are subsequently discarded. The extent of the message loss was observed to be generally increasing with the detector load, however not linearly. It is rather the case, that characteristic message rates exist, at which the loss is especially high. In total, the discarded messages due to this issue have been approximated to be up to 15 % of all messages[1]. Furthermore, the problem was fixed in the SPADIC versions 2.1 and up [Kri18].

3.3.5. Expected Random Noise

The random noise on the SPADIC's analog part is in the order of $Q_{\mathrm{random}} \approx 200\,\mathrm{e}^- + 20\,\mathrm{e}^-/\mathrm{pF}$ [CBM18]. As the pad capacity is in the order of $C_{\mathrm{pad}} \approx 30\,\mathrm{pF}$, this gives a random noise of $Q_{\mathrm{random}} \approx 800\,\mathrm{e}^-$. To compare this to the digitized signal output of the SPADIC it has to be converted into ADC values. The maximum voltage of the shaper response depending on the incoming charge Q_i can be calculated by [Arm13]:

$$\hat{V}_{\mathrm{s}} = \frac{2n}{e} \frac{Q_i}{C_s} \tag{3.3}$$

[1]private communication, P. Kähler (March 2018)

With the number of amplifier cells $n = 12$ and feedback capacity $C_s = 450\,\mathrm{fF}$ one gets [Arm13]:

$$\hat{V}_{\mathrm{s}} = 19.26\,\frac{\mathrm{mV}}{\mathrm{fC}} \cdot \mathrm{Q_i} \tag{3.4}$$

As the output range of 1 V (0.5 V to 1.5 V, [Arm13]) is digitized into 512 ADC values this results in:

$$1\,\mathrm{ADC} \equiv 1.95\,\mathrm{mV} \tag{3.5}$$

This can be inserted into Equation 3.4 to get the input charge equivalent to 1 ADC value:

$$Q_{1\mathrm{ADC}} = 0.0996\,\mathrm{fC} \approx 622\,\mathrm{e}^{-} \tag{3.6}$$

As $Q_{1\mathrm{ADC}} < Q_{\mathrm{random}} < 2 \cdot Q_{1\mathrm{ADC}}$, random analog noise is not expected to be larger than 2 ADC.

4. Analysis

In this chapter, the results of the analysis will be presented. As the DESY 2017 campaign was the first time the detectors and readout electronics were tested in a setup of this scale, a considerable amount of QA had to be done to gain a better understanding of the behaviour of the system in general. Results of the QA are shown in Section 4.1. After the examination of many general aspects of the system, an analyis regarding its electron detection efficiency was conducted, which is presented in Section 4.2.

4.1. QA

4.1.1. Hit Correlations and Time

As a first step, the timing structure of hits in the detectors was investigated. In Figure 4.1 a section of a measurement at a beam momentum of $3\,\mathrm{GeV}/c$ is visualized. In this histogram, the X-axis represents the time in timestamps while on the Y-axis the different SPADICs are plotted. An entry is placed every time a channel on a SPADIC is self-triggered (triggertype 1 or 3). In the histogram, the beam's spill structure caused by the DESY magnet cycle (see Section 3.1.2) is clearly visible. By measuring the distance in time between the start of consecutive spills, a magnet frequency of $(12.49 \pm 0.06)\,\mathrm{Hz}$ is determined, which is in accordance with [D+18]. As no signal is expected in between the electron spills, it can already be seen that the TRDs 1-3 and the scintillation detectors work fairly clean, while TRD 0 has noise on it, which is further discussed in Section 4.1.7. The secondary beam arrives in the time intervals in which the primary electrons in the DESY II have momenta equal to or above the selected secondary beam momentum (see Section 3.1.2). Hence, at a lower selected momentum, the length of the spills is expected to increase, while the intervals in between the spills should decrease. This behaviour can be seen by comparing the measurement at $3\,\mathrm{GeV}/c$ (Figure 4.1) with a measurement at $1\,\mathrm{GeV}/c$ (Figure 4.2).

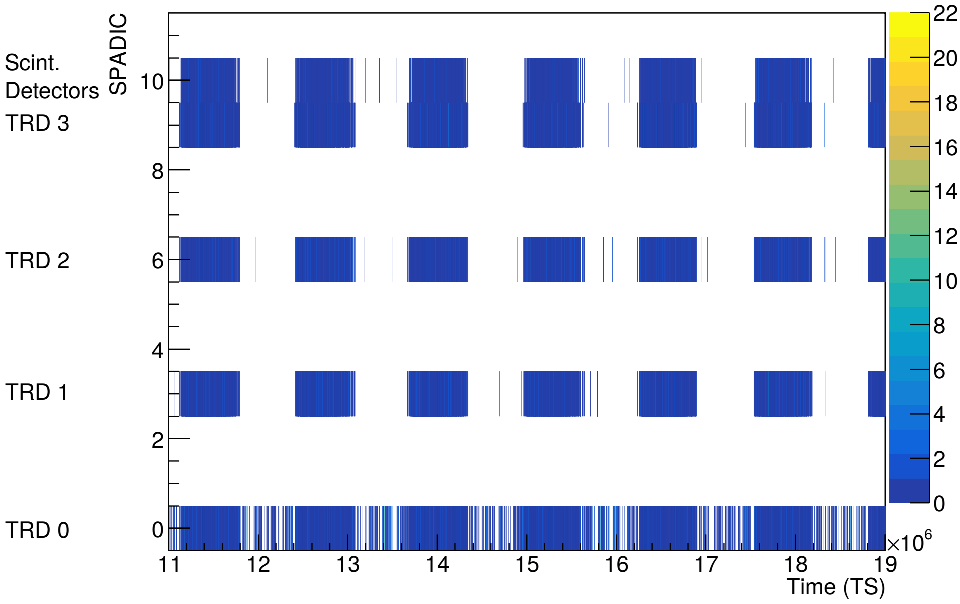

Figure 4.1.: Self-triggered messages on each SPADIC/detector at 3 GeV/c plotted as a function of time: The range of the X-axis of $8 \cdot 10^6$ TS is equal to 0.5 s of measurement.

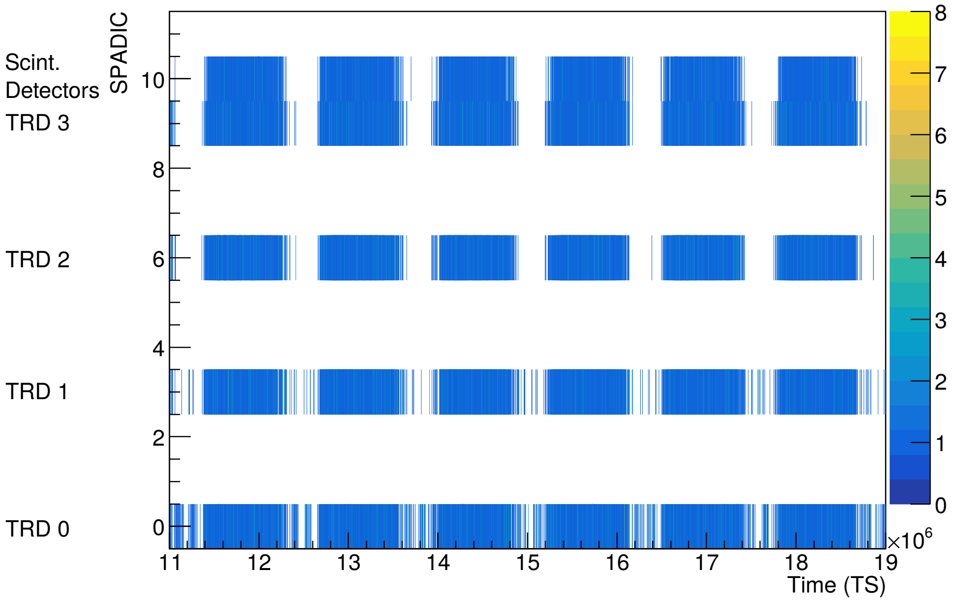

Figure 4.2.: Self-triggered messages on each SPADIC/detector at 1 GeV/c plotted as a function of time: The range of the X-axis of $8 \cdot 10^6$ TS is equal to 0.5 s of measurement.

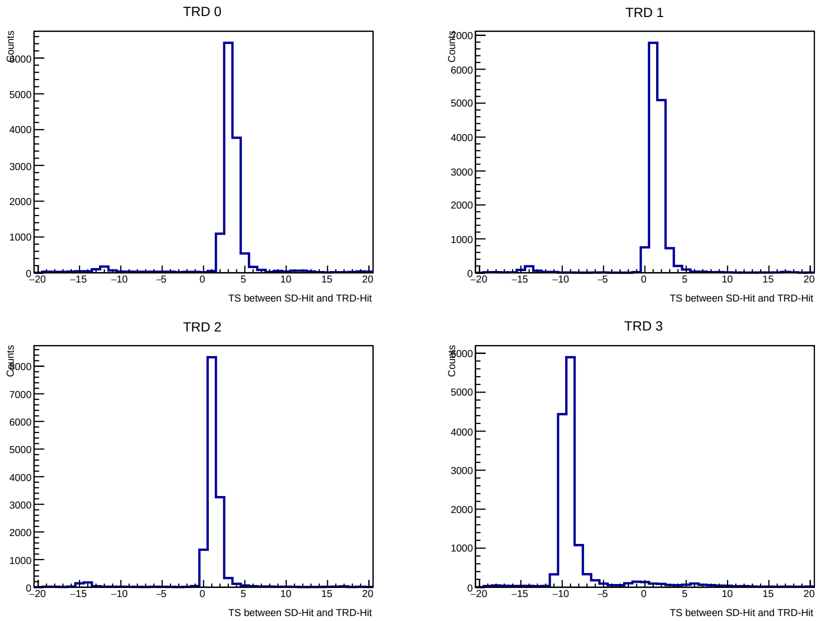

Figure 4.3.: Uncorrected time difference spectra between a coincidence on the SDs and a hit on one of the TRDs. The difference is calculated by $\Delta t = t_{\mathrm{TRD}} - t_{\mathrm{SD}}$, hence, an entry on positive Δt corresponds to a later signal on the TRD (Run 111).

4.1.2. Synchronicity between Detectors

4.1.2.1. Incomplete Synchronization and Corrections

At the time of the test beam, the procedure to synchronize all SPADICs was just recently implemented and not yet fully tested. After the test beam, errors in this procedure were found suggesting the possiblilty of small deviations of a few TS between the SPADIC clocks. To test this, the time difference between a coincidence in the SDs and a hit message in one of the TRDs was examined. For each single TRD this is plotted in Figure 4.3 for one measurement run (run 111), and in Figure 4.4 for a different measurement run (run 88). If all clocks were running synchronous, one would still expect a non-zero time difference due to different cable lengths and response times of the SDs and TRDs, but this shift should be constant over all measurement runs. When comparing Figure 4.3 and Figure 4.4 one can see that the shift clearly changes. Hence, this is not a physical time difference, but an effect caused by incomplete synchronization, needing to be corrected. This was done by calculating the median of each time difference distribution and setting it to zero, as shown in Figure 4.5.

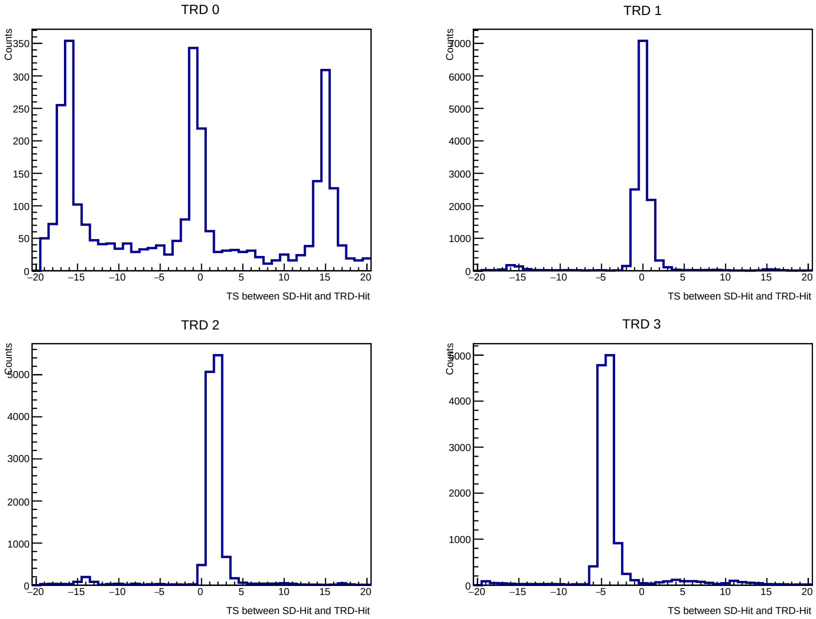

Figure 4.4.: Uncorrected time difference spectra between a coincidence on the SDs and a hit on one of the TRDs. The difference is calculated by $\Delta t = t_{\mathrm{TRD}} - t_{\mathrm{SD}}$, hence, an entry on positive Δt corresponds to a later signal on the TRD (Run 88).

The histogram of TRD 0 in run 88 (upper left panel of Figure 4.4) has a significantly smaller amount of entries and furthermore, its time difference distribution shows three peaks, which are about 16 TS apart. In this particular run (and others, further discussed in Section 4.1.5), the SPADIC on TRD 0 was, additionally to the incomplete synchronization mentioned above, out of sync by one epoch (4096 TS). The peaks in the spectrum are caused by the quantization of the electron beam by the DESY II revolution frequency of $1.025\,\mathrm{MHz} \approx (15.61\,\mathrm{TS})^{-1}$. When incrementing the TS of SPADIC 0 by 4096, it behaves similarly to the other SPADICs (see Figure 4.6). The small peaks 16 TS to the left or right of the main peak can also be spotted in the time difference distributions of the detectors which are not out of sync by one epoch (Figure 4.3 & Figure 4.6).

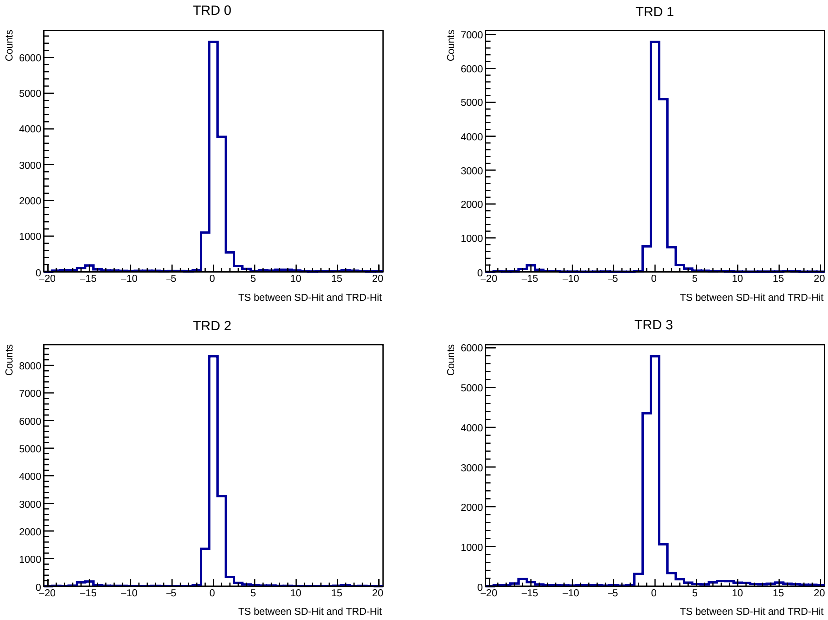

Figure 4.5.: Corrected time difference spectra between a coincidence on the SDs and a hit on one of the TRDs. The difference is calculated by $\Delta t = t_{\mathrm{TRD}} - t_{\mathrm{SD}}$, hence, an entry on positive Δt corresponds to a later signal on the TRD (Run 111).

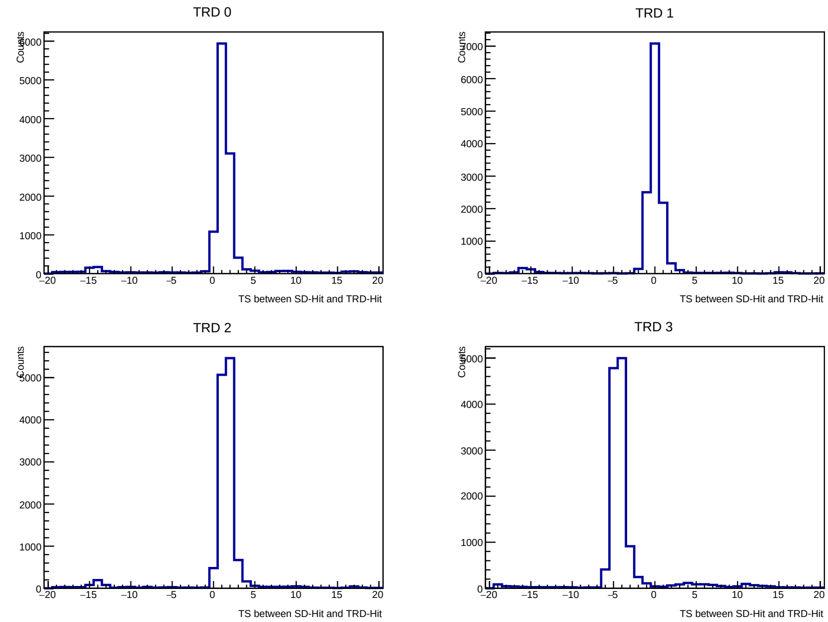

Figure 4.6.: Uncorrected time difference spectra between a coincidence on the SDs and a hit on one of the TRDs. The time on the SPADIC on TRD 0 was incremented by 4096 TS. The difference is calculated by $\Delta t = t_{\mathrm{TRD}} - t_{\mathrm{SD}}$, hence, an entry on positive Δt corresponds to a later signal on the TRD (Run 88).

4.1.2.2. Width of Time Difference Distribution

When taking into account only the physical process of an electron passing through the detectors, a very narrow time difference distribution is expected. The time difference resulting from the time of flight of the electron and the different response times of the TRDs and SD is a fixed value which is the same for each electron. Hence, depending on the phase position with respect to the ADC sampling, only two different time differences should be possible. With a traveled distance of $s = 4.3\,\mathrm{m}$ between the entry window of the first TRD and the last SD, and a velocity $v \approx c \approx 3 \cdot 10^8\,\mathrm{m/s}$ the time difference due to the time of flight is approximately:

$$\Delta t_{\mathrm{TOF}} = \frac{s}{c} \approx 14.3\,\mathrm{ns} \tag{4.1}$$

The response time for the SDs can be estimated by adding the rising times of both the scintillator and the PMT:

$$t_{\mathrm{SD}} = t_{\mathrm{scin}} + t_{\mathrm{PMT}} = 4.3\,\mathrm{ns} \tag{4.2}$$

With the signal collection time of the TRDs of $t_{\mathrm{TRD}} = 300\,\mathrm{ns}$ the resulting measured time difference is:

$$\Delta t_{\mathrm{tot}} = -281.4\,\mathrm{ns} \approx -4.5\,\mathrm{TS} \tag{4.3}$$

Hence, based on the physical processes alone, the time difference should be $-4\,\mathrm{TS}$ in about $50\,\%$ of the cases, and $-5\,\mathrm{TS}$ in the other, resulting in entries in only two different bins.
As the time difference distribution is fairly wide and has a significant amount of entries for at least 4 different time differences, effects of the readout electronics have to be taken into account. First of all, two obvious factors that can possibly lead to earlier/later triggering on one of the TRDs are the baseline and the amplitude of the signal. As is known (and further discussed in Section 4.1.6), the baselines of the different channels of the SPADIC were not all located on the same level and also slightly vary over time. Since absolute trigger thresholds were used, a signal lying on a higher baseline will fulfill the trigger conditions earlier than a signal with the same amplitude coming from a lower baseline. Similarly, a signal with a higher amplitude and thus a steeper rising slope will fulfill the conditions earlier than a lower amplitude signal coming from the same baseline level. Furthermore, these two effects cannot be separated easily, as e.g. a signal with a higher amplitude can still trigger later than a signal with a lower amplitude coming from a higher baseline. The correlation of amplitude and baseline position with the time difference between a coincidence in the SDs and a hit in a TRD can be observed in Figure 4.7, in which the maximum ADC value of each signal with a specific time difference is plotted against the value of its first sample. Even though the entries in the histograms are widely spread, the mean values show a clear correlation, wich can be seen in the two lower panels.

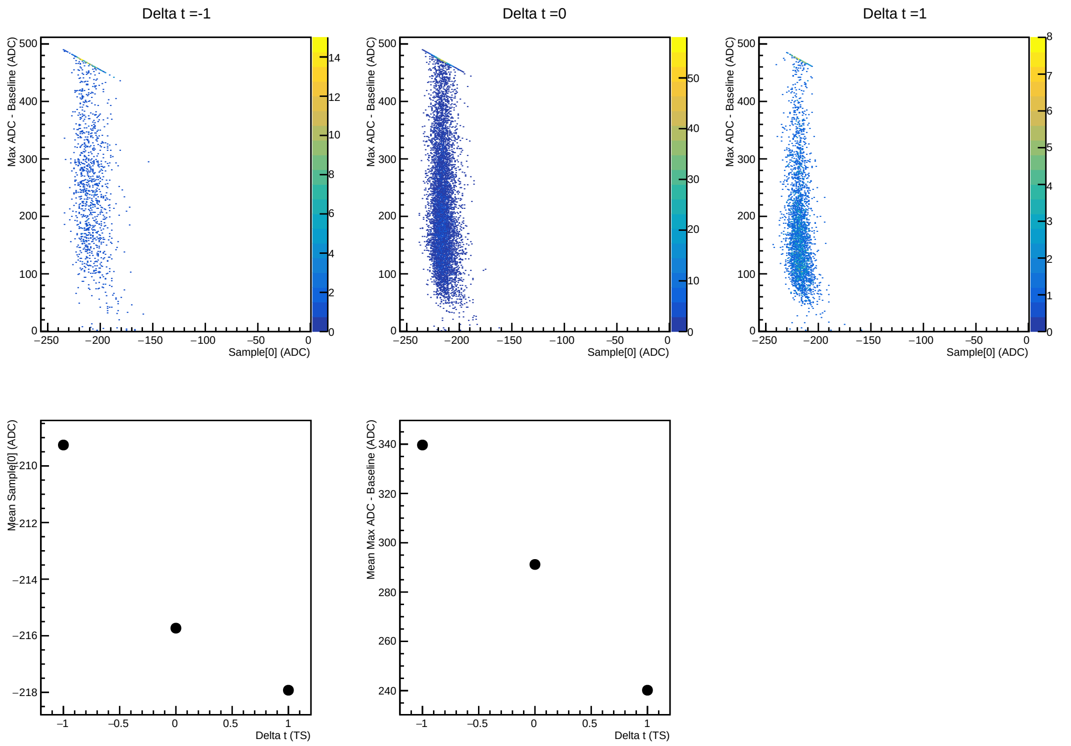

Figure 4.7.: Maximum ADC values (baseline corrected) of self-triggered hit messages with $\Delta t = -1\,\text{TS}$, $\Delta t = 0\,\text{TS}$ and $\Delta t = 1\,\text{TS}$ plotted against the ADC value of their sample[0] (upper panels). In the lower panels, the mean values in X- (left panel) and Y-direction (right panel) of the three upper histograms are shown.

A second effect that can lead to different time differences - even at exactly the same amplitude and baseline - is the phase position of the signal with respect to the sampling of the ADC. This is visualized in Figure 4.8: In both panels, one fast, high amplitude signal similar to the signal of the SD, and one slower, lower amplitude signal similar to the signal of the TRD, can be seen[1]. Then continuous analog signals are represented by the lines, while the points show the sampled ADC values at each TS. The two trigger threshold can be seen as dashed horizontal lines. In both panels, the two signals occur at exactly the same time, hence, one would expect a time difference of $\Delta t = 0\,\mathrm{TS}$ in both cases. In the upper panel, this is in fact the case: Both signals fulfill the trigger condition (see Section 3.3.1) at the same time, with:

$$[S_{\mathrm{SD}}(0\,\mathrm{TS}) \leq T_1] \wedge \quad [S_{\mathrm{SD}}(1\,\mathrm{TS}) \geq T_1] \wedge [S_{\mathrm{SD}}(2\,\mathrm{TS}) \geq T_2] \tag{4.4}$$
$$[S_{\mathrm{TRD}}(0\,\mathrm{TS}) \leq T_1] \wedge [S_{\mathrm{TRD}}(1\,\mathrm{TS}) \geq T_1] \wedge [S_{\mathrm{TRD}}(2\,\mathrm{TS}) \geq T_2] \tag{4.5}$$

As the condition is fulfilled at the exact same time, this would give $\Delta t = 0\,\mathrm{TS}$. In the lower panel, the exact same signals as in the upper panel can be seen, the only difference being a phase shift with respect to the ADC sampling. Here, at $t = 1\,\mathrm{TS}$, the sample of the SD signal is above both thresholds (most importantly above T_1), while the sample of the TRD signal is below both thresholds, resulting in both signals fulfilling the trigger conditions at different times:

$$[S_{\mathrm{SD}}(0\,\mathrm{TS}) \leq T_1] \wedge \quad [S_{\mathrm{SD}}(1\,\mathrm{TS}) \geq T_1] \wedge [S_{\mathrm{SD}}(2\,\mathrm{TS}) \geq T_2] \tag{4.6}$$
$$[S_{\mathrm{TRD}}(1\,\mathrm{TS}) \leq T_1] \wedge [S_{\mathrm{TRD}}(2\,\mathrm{TS}) \geq T_1] \wedge [S_{\mathrm{TRD}}(3\,\mathrm{TS}) \geq T_2] \tag{4.7}$$

Thus, the measured time difference between the two signals in the lower panel would be $\Delta t = 1\,\mathrm{TS}$ as signal from the TRD fulfills the condition one TS later than the signal from the SD. The dependence of Δt on the signal's phase positions with respect to the sampling rate is difficult to quantify, as it depends also on the difference of length and amplitude of the two signals. In general, the Δt of two synchronous signals will be as high as the number of consecutive samples in which $S_{\mathrm{SD}} \geq T_1$ while $S_{\mathrm{TRD}} < T_1$.

As stated above, the physical time difference between the analog signal of the SDs and each one of the TRDs will always be the same. Therefore, if there is a smaller *measured* time difference, the trigger condition was fulfilled on a part closer to the start of the analog signal of the TRD, while a larger time difference indicates triggering on a later part of the signal shape. Hence, the TRD's signal shape captured in the 32 samples should have a slightly different form, depending on the measured time difference between the trigger on the SD and the TRD.

[1]For the actual measured signalshapes see Section 4.1.4.

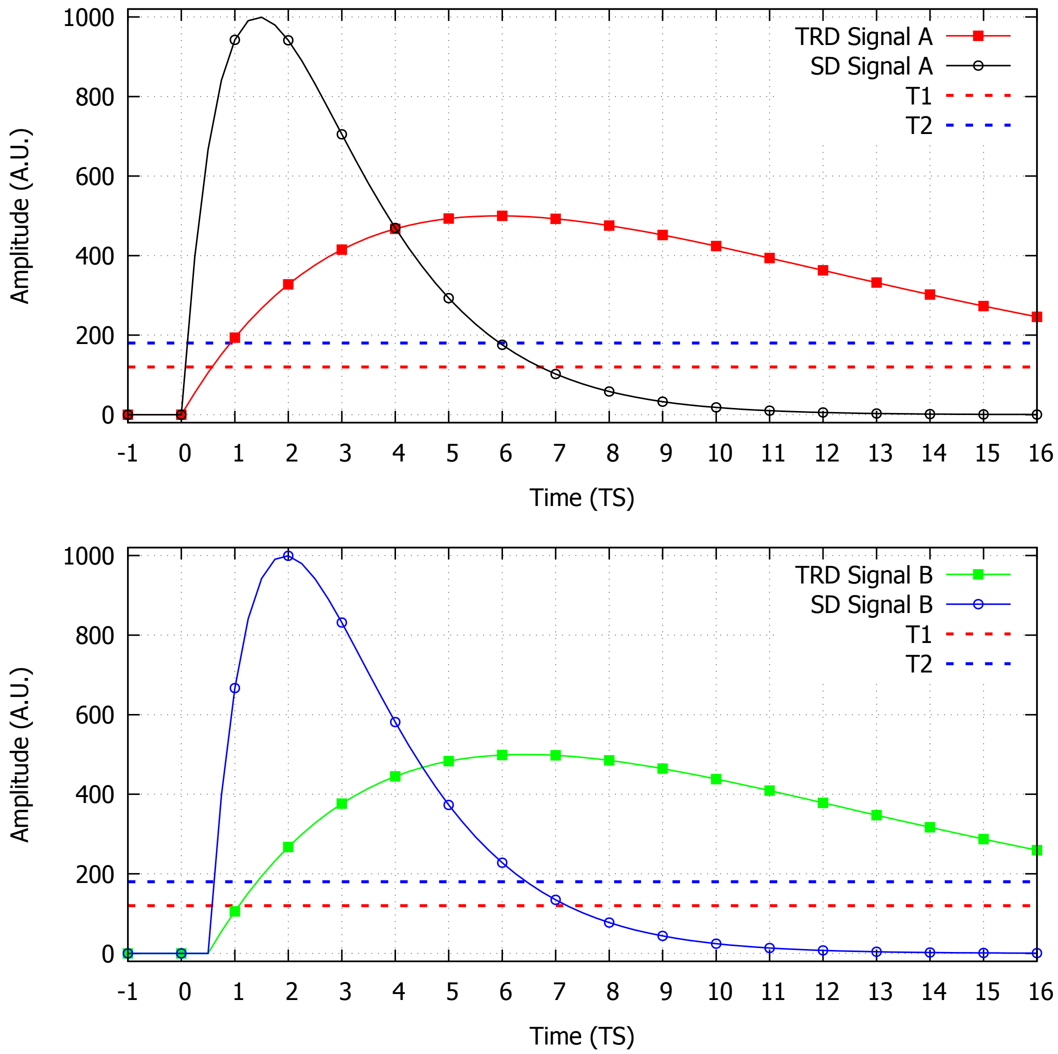

Figure 4.8.: Possible analog signals coming synchronous from the SDs and a TRD being sampled by the ADC: In the upper panel, the measured time difference is $\Delta t = 0\,\mathrm{TS}$, while in the lower panel it is $\Delta t = 1\,\mathrm{TS}$. The difference is only caused by a different phase position with respect to the sampling.

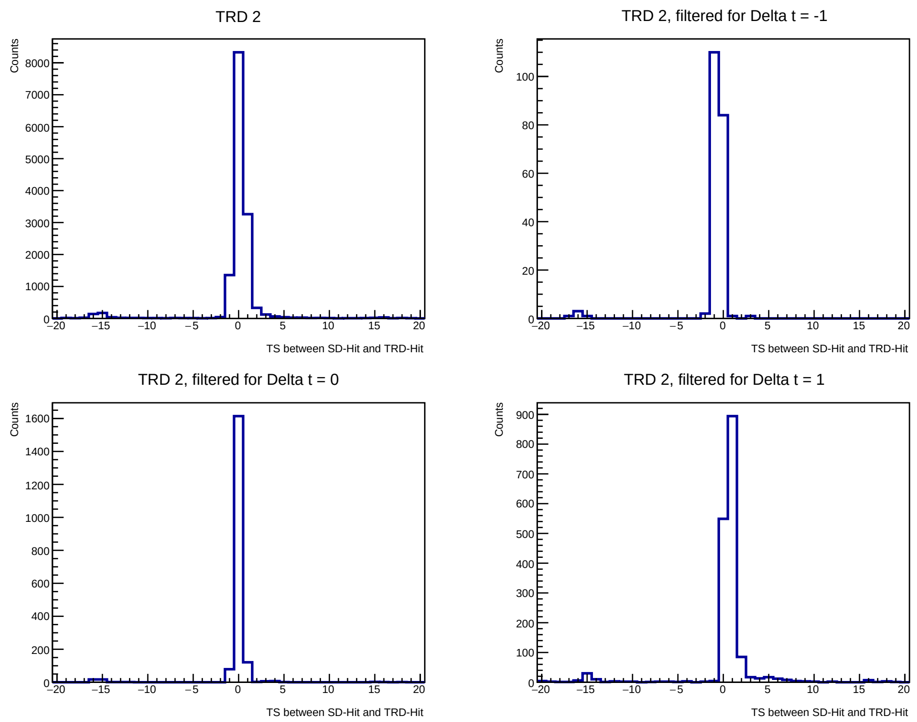

Figure 4.9.: Time difference distributions on TRD 2: The upper left panel includes all self-triggered hit messages, while the other three conditions for specific forms of the signal shape (see Section A.3) were applied to show, how at different Δt, the hit logic triggers on different phases of the analog signal.

Furthermore, one should be able to filter for a specific time difference by demanding a specific form of the signal shape. After setting the median of each time difference distibution to zero, as mentioned in Section 4.1.2.1, different conditions for the signal shapes were applied, in order to filter for $\Delta t = -1\,\mathrm{TS}$, $\Delta t = 0\,\mathrm{TS}$ and $\Delta t = 1\,\mathrm{TS}$, respectively. The resulting distributions are plotted in Figure 4.9, while the exact used filter conditions are listed in Section A.3.

4.1.3. Beam Position and Width

The position and width of the electron beam on each TRD can be approximated simply by counting the number of hit messages on each pad, which has already been done in Ref. [Fid]. For a calculation of the beam width, it has to be decided which triggertypes should be taken into account. While looking exclusively at hits with triggertype 1 will result in a calculated beam width, which is smaller than the actual beam, a combination of the triggertypes 1 and 3 will give a too large width. Thus, both methods were used and compared to achieve the most accurate results. The hitmaps on all four TRDs for messages with triggertype 1 at a beam momentum of $4\,\mathrm{GeV}/c$ are plotted in Figure 4.10. These where

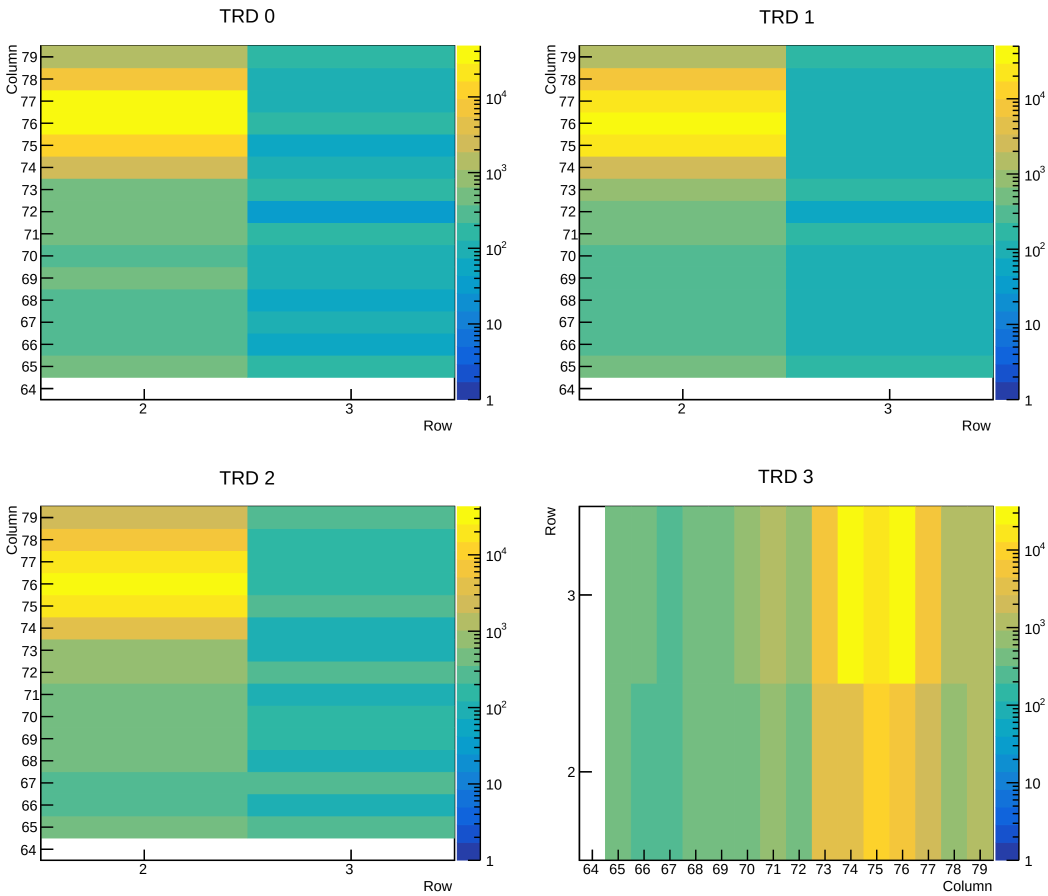

Figure 4.10.: Hitmaps for each TRD: The total amount of hit messages with triggertype 1 registered on individual pad is plotted. The data was taken from one TSA file at a momentum of 4 GeV/c.

then projected on the Y-axis (X-axis for TRD 3) and fitted with a Gaussian function. This was also done with the hitmaps for both triggertypes 1 and 3. The projections and fitted Gaussian functions can be seen in Figure 4.11, while the fit parameters are listed in Table 4.1. This procedure has been repeated also for runs at 1,2 and 3 GeV/c, the plots of hitmaps, projections and Gaussian fits can be found in Figure A.4 - A.8.

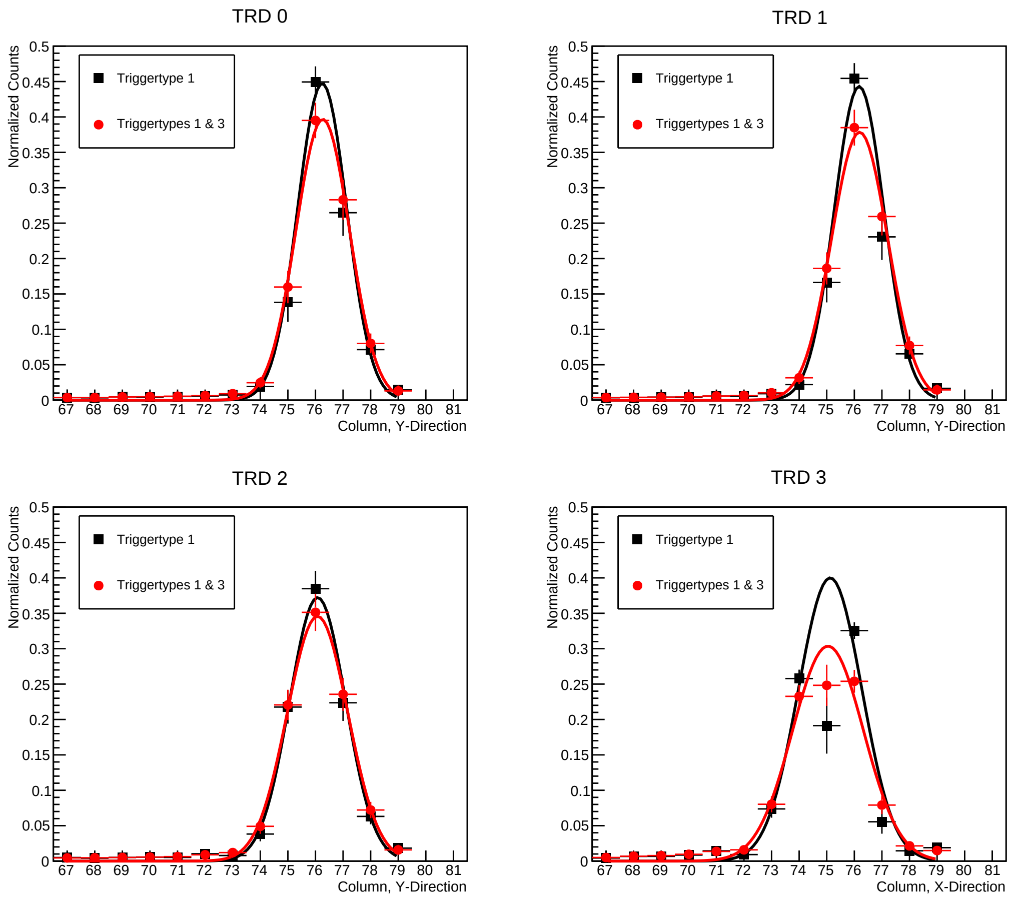

Figure 4.11.: Projections of the hitmaps on the “column-axis”, each fitted with a Gaussian function: The TRDs 0-2 give the beam position in Y-direction and TRD 3 in X-direction, due to its rotation by 90°.

Table 4.1.: Fit parameters of the Gaussian fits for the projections of the hitmaps at 4 GeV/c: The data and the Gaussian functions are plotted in Figure 4.11.

TRD	Triggertypes	Constant	Mean (Column)	Sigma (Column)	χ^2_{red}
0	1	0.45 ± 0.02	76.24 ± 0.05	0.890 ± 0.038	1.30
	1 & 3	0.40 ± 0.02	76.26 ± 0.05	0.969 ± 0.041	0.90
1	1	0.44 ± 0.02	76.17 ± 0.05	0.902 ± 0.036	1.67
	1 & 3	0.38 ± 0.02	76.19 ± 0.05	1.013 ± 0.041	0.96
2	1	0.37 ± 0.02	76.08 ± 0.05	1.018 ± 0.042	1.45
	1 & 3	0.35 ± 0.02	76.08 ± 0.05	1.098 ± 0.044	1.08
3	1	0.40 ± 0.02	75.13 ± 0.04	1.151 ± 0.039	6.72
	1 & 3	0.30 ± 0.02	75.05 ± 0.05	1.287 ± 0.046	2.74

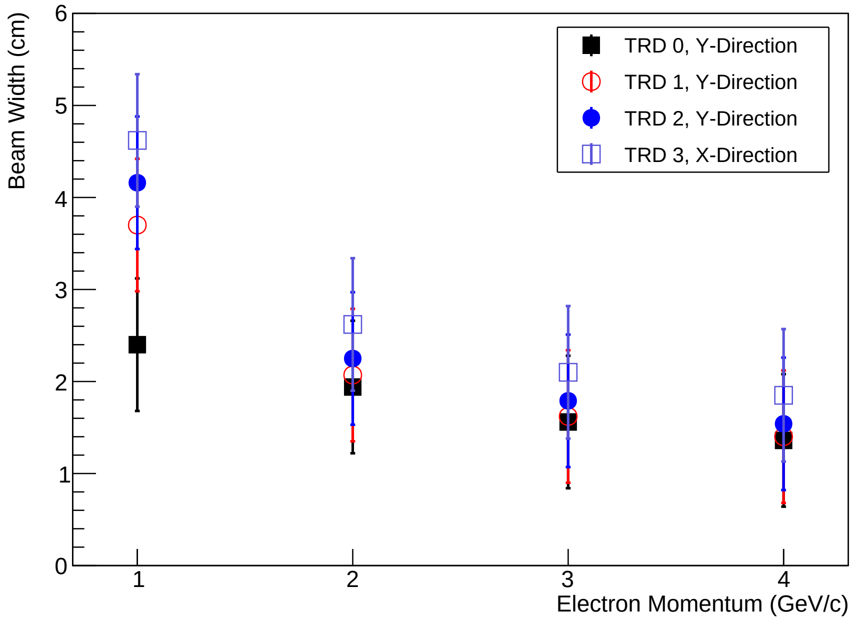

Figure 4.12.: Calculated beam widths for each TRD in the direction of its respective high position resolution are plotted against the electron momentum.

The beam width has been then calculated as twice the mean RMS of the two Gaussian fits $2\bar{\sigma}$ with an approximated error of one pad width (0.72 mm). When plotting the beam width against the electron momentum, a dependence similar to Figure 3.11 can be seen (see Figure 4.12). Furthermore, two more observations are remarkable from Figure 4.12: First, the momentum dependence seems to increase with the distance to the collimator. This can be explained by the fact, that at lower momenta, the electrons undergo more scattering processes *per length*. Hence, the further a detector is positioned down the beam line, the bigger will be the difference between the widths at different momenta.
Second, even at high electron momenta there is a gap between the width measured on the TRDs 0-2, which is in Y-direction, and TRD 3, which is in X-direction. This is due to the beam not being symmetrical, as mentioned in Section 3.1.4.

Table 4.2.: Fractions of the electon beam hitting the pad plane of each individual TRD at all four momenta: The fractions were calculated using Equation 4.8 and the Gaussian fits shown in Figure 4.11 and Figure A.5 - A.9.

		Electron Momentum			
TRD	Trg.	1 GeV/c	2 GeV/c	3 GeV/c	4 GeV/c
0	1	$(86.50 \pm 4.84)\,\%$	$(97.89 \pm 5.87)\,\%$	$(99.61 \pm 4.35)\,\%$	$(99.90 \pm 4.69)\,\%$
	1 & 3	$(89.07 \pm 4.85)\,\%$	$(97.67 \pm 6.00)\,\%$	$(99.36 \pm 6.08)\,\%$	$(99.76 \pm 4.82)\,\%$
1	1	$(85.60 \pm 4.74)\,\%$	$(97.88 \pm 5.73)\,\%$	$(99.67 \pm 4.27)\,\%$	$(99.91 \pm 4.56)\,\%$
	1 & 3	$(87.87 \pm 4.74)\,\%$	$(97.24 \pm 5.83)\,\%$	$(99.24 \pm 6.00)\,\%$	$(99.72 \pm 4.76)\,\%$
2	1	$(82.93 \pm 4.67)\,\%$	$(96.86 \pm 5.64)\,\%$	$(99.23 \pm 5.96)\,\%$	$(99.79 \pm 4.76)\,\%$
	1 & 3	$(86.83 \pm 4.58)\,\%$	$(96.76 \pm 5.57)\,\%$	$(98.98 \pm 5.96)\,\%$	$(99.61 \pm 6.16)\,\%$
3	1	$(91.31 \pm 3.96)\,\%$	$(99.18 \pm 4.56)\,\%$	$(99.87 \pm 3.08)\,\%$	$(99.96 \pm 2.90)\,\%$
	1 & 3	$(90.70 \pm 4.13)\,\%$	$(98.54 \pm 4.99)\,\%$	$(99.66 \pm 5.17)\,\%$	$(99.89 \pm 3.97)\,\%$

From the Gaussian fits, also the percentage of the electron beam hitting the active detector area can be determined. This was done by dividing the integral of the fit function over the active pad plane by its integral over the whole space:

$$\mathrm{Ratio} = \frac{\int_{64.5}^{79.5} f(x)\mathrm{d}x}{\int_{-\infty}^{\infty} f(x)\mathrm{d}x} \tag{4.8}$$

The results for each TRD at each momentum can be found in Table 4.2.

4.1.4. Signal Shapes and ADC Spectra

An investigation of the signal shapes is useful to gain a deeper understanding of the behaviour of the detectors and readout electronics, as they essentially characterize the response of the system as a whole to incoming radiation. At first, signal shapes from the most active channels on each TRD and SD from run 97 were compared. As radiators were mounted on all four TRDs, similar detector responses are expected. Overlays of all signal shapes per detector from one TSA file can be seen in Figure 4.13 - Figure 4.15, and Figure A.10 & Figure A.11.

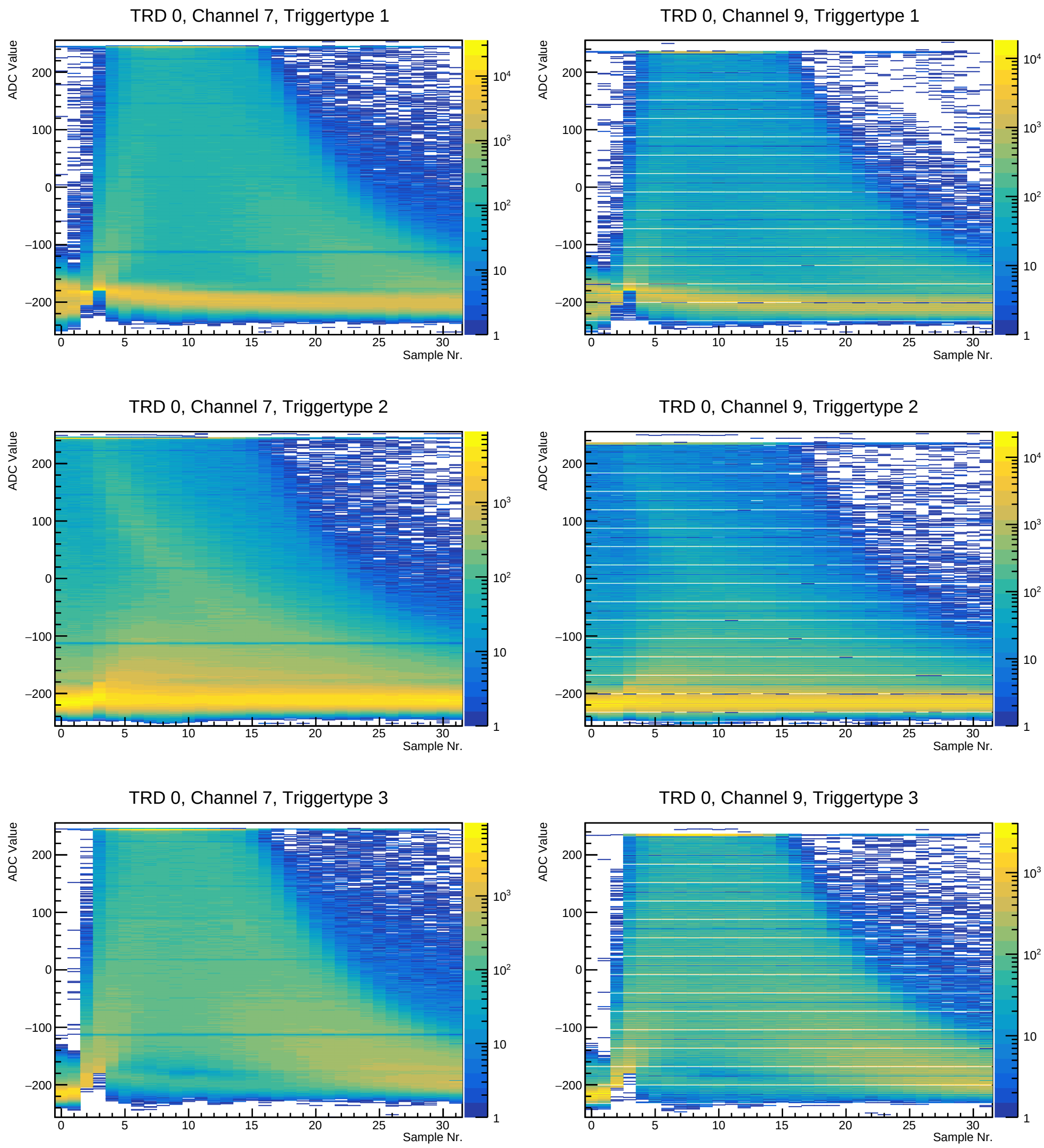

Figure 4.13.: Overlays of signal shapes on the two most active channels of TRD 0 for different triggertypes. The data is taken from one TSA file of run 97.

For triggertype 1 (upper two panels), two bands are visible: One is a wide band of signals with shapes similar to the expected shaper response (Equation 3.1). Starting at low ADC values, the signals then rise above the trigger thresholds to their maximum before decreasing exponentially. The second, more narrow band consists of signals with high ADC values at the beginning, which seem to just fall to the baseline over time. These signals are caused by a retriggering on the falling tail of a previous, higher signal. As described in Section 3.3.1, a signal coming from above and dipping between the thresholds for just one or two samples can also fulfill the trigger condition (see right panel of Figure 3.21). As these signals do not contain information about charge or timing of a particle entering the detector, they can be regarded as noise. They are noticable in the signal shapes for triggertype 3 (lower two panels) as well, but with a significantly lower amount of entries. This is because it is less likely for a retriggering on the falling tail to occur at the exact moment of a trigger on the neigbouring pad.

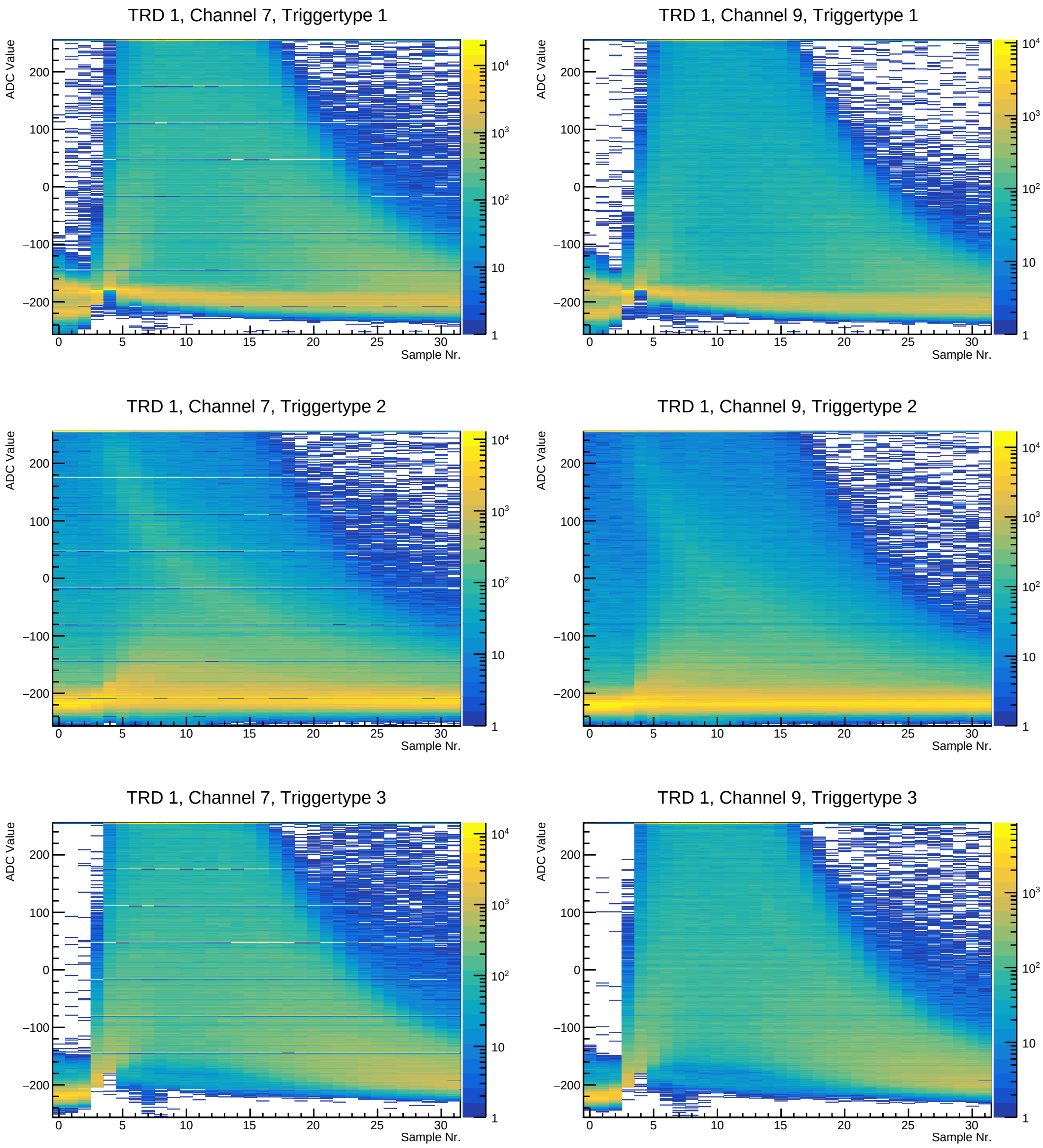

Figure 4.14.: Overlays of signal shapes on the two most active channels of TRD 1 for different triggertypes. The data is taken from one TSA file of run 97.

A broad distribution of ADC values of the first samples can be observed for signal shapes with triggertype 2 (middle panels). In theory, the forced neighbour readout was implemented to read low amplitude signals on pads next to the ones with the main part of the signal as this increases the position resolution. Although also a band of low amplitude signals can be spotted, it is clear that in many cases, falling tails of high amplitude signals were read out. Hence, these high amplitude signals triggered a readout themselves, which was then interrupted by a FNR due to a trigger on a neighbouring pad. This could be partly caused by the *multimessage effect*[2] characterized in [Bec18].
Furthermore, in Figure 4.13 and Figure 4.14 some problems with the ADC sampling can be recognized, as certain ADC values on certain channels (e.g. TRD 0, channel 9 or TRD 1, channel 7) were not sampled in any message. Additionally, the signals on TRD 0 seem to reach an upper limit of the ADC already at values lower than 255 (245 on channel 7 and 234 on channel 9). The suppression of certain ADC values has been observed in various runs on different SPADICs and channels. Also the extent of the suppression seems to be varying. In some cases, as the beforementioned ones, certain ADC values are sampled not even once. On the other hand, in certain runs and channels, e.g. every second ADC value was observed to have just slightly less entries. This is noticable in the ADC spectra used for the baseline calculation in Section 4.1.6 (see Figure 4.20). This was excluded to be an reconstruction artifact, but it could not be determined in a brief analysis if this behaviour was caused by the individual SPADICs, AFCKs or in the message unpacking.

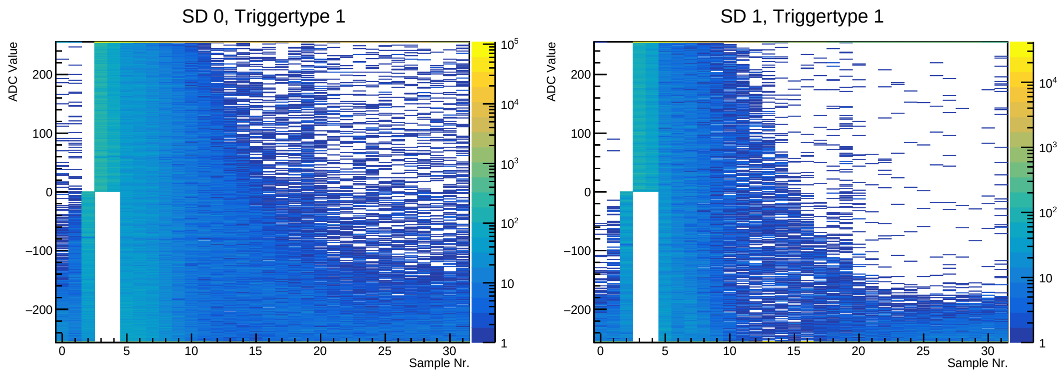

Figure 4.15.: Overlays of signal shapes on the two SDs. The data is taken from one TSA file of run 97.

[2]The fix in the unpacker to recombine multi messages was implemented in this analysis, but it only recombines messages with predecessors with less than 5 samples. As this value was chosen on the basis of data from a setup with a different detector prototype, chamber gas and incoming radiation, it can't be excluded that in this setup, multi messages occur also with 5 or more samples in the predecessor.

Finally, also the signal shapes of the scintillation detectors have to be considered (Figure 4.15). These look different to the ones of the TRDs, since the PMTs output negatively charged pulses and hence, the negative front-end of the SPADIC had to be used. The PMT's specified rise time of 3.4 ns is already significantly shorter than the signal collection time of the TRDs, and in combination with the lower shaping time of the negative frontend (80 ns compared to 240 ns) this leads to fairly short signal shapes. Also, as the baselines were not calibrated on this SPADIC, its position is below the minimum ADC value. The properties of the CSA of the SPADIC are designed to fit the output charge pulses of the TRD with charges up to 75 fC into the dynamic range of the ADC. The signals from the SDs seem to have a higher amplitude and thus exceed the maximum ADC value. In Figure A.12 it can be observed very clearly, that the majority of signals first stays below the minimum ADC, then rises above the maximum ADC for a few TS, before falling back below the minimum.

A brief study of spectra of maximum ADC values was done only on one channel, which does not show the problems with the sampling seen in the signal shapes. A spectrum can be seen in the upper right panel of Figure 4.16. In the upper left panel, the maximum ADC is plotted against the ADC value of the first sample. Here the "normal" signals and the signals caused by retriggering on falling tails are clearly separated. As already noticed in the signal shapes, the band of retrigger signals starts at fairly high ADC values before falling down to the baseline. Hence, in the plot of maximum ADC against the ADC of sample[0], these signals are located at positions close to the diagonal of $\mathrm{ADC}_{\mathrm{Max}} = \mathrm{ADC}_0$. In the maximum ADC spectrum they can be seen as a peak at values just above the second threshold $T_2 = -180\,\mathrm{ADC}$. To exclude these signals, following cut condition for the left histogram was introduced:

$$\text{Cut if}(\mathrm{ADC}_{\mathrm{Max}} \leq 0.41 \cdot \mathrm{ADC}_0 - 85.6) \tag{4.9}$$

The values were chosen rather arbitrarily. The condition cuts 17.18 % of hit messages and the results can be seen in the lower two panels of Figure 4.16. As a radiator was mounted on TRD 1 in the run where the data for Figure 4.16 was taken, the spectrum is, as expected fairly broad. Results with and without this cut for data without a radiator can be seen in Figure 4.17. Here the spectrum is more narrow. In both spectra without the cut, there are also entries below the upper threshold $T_2 = -180\,\mathrm{ADC}$. These result from signals being retriggered by FNR before of sample[5] and are also excluded by the cut.

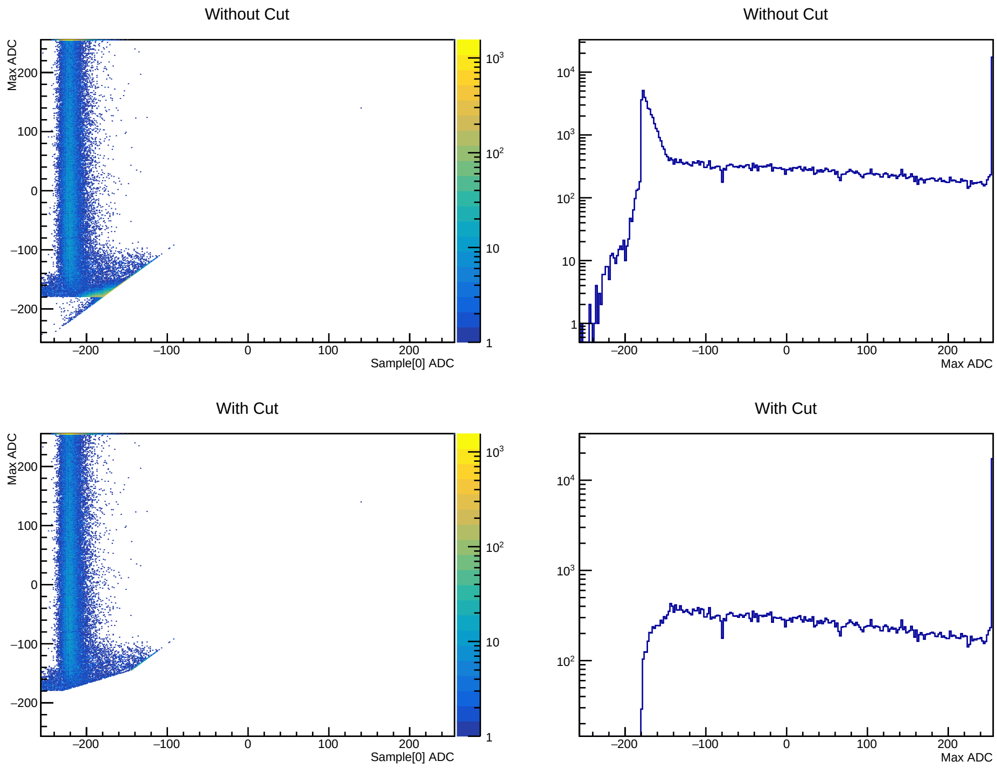

Figure 4.16.: Maximum ADC of channel 7 on TRD 1 without a cut (top panels) and with a cut for retriggering on falling tails: In the left panels the maximum ADC value is plotted against the value of the first sample, in the right panels, the maximum ADC spectrum can be seen. The data was taken from a run at 4 GeV/c with a radiator mounted on the detector.

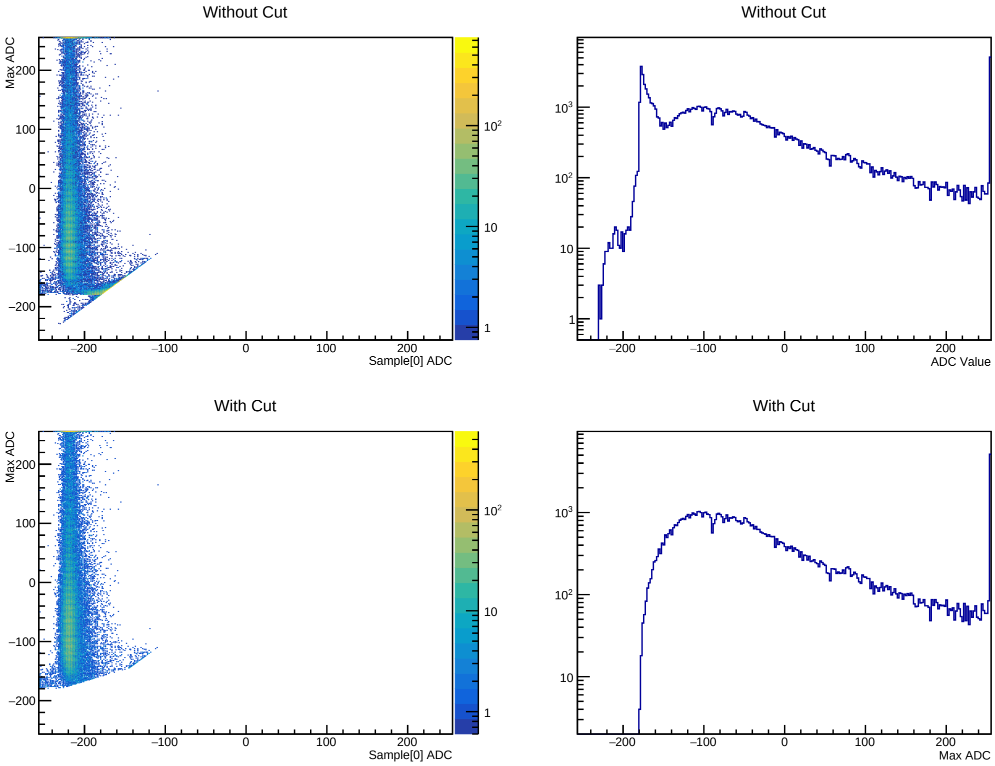

Figure 4.17.: Maximum ADC of channel 7 on TRD 1 without a cut (top panels) and with a cut for retriggering on falling tails: In the left panels the maximum ADC value is plotted against the value of the first sample, in the right panels, the maximum ADC spectrum can be seen.

4.1.5. Missing Presample

As the first two of the 32 samples of a hit message are presamples, the samples corresponding to a, b and c in the trigger condition (Equation 3.2) are sample[2], sample[3], and sample[4] respectively. When applying this trigger condition to all self-triggered hit messages (triggertype 1 & 3), one would expect each one to fulfill it. In Figure 4.18 and Figure 4.19 the signal shapes of all self-triggered hit messages from the SPADICs TRD 0 and TRD 1 from a TSA file of run 88 are visualized. Signal shapes fulfilling the trigger condition are plotted in the left panel, while those which do not are filled into the right panel.

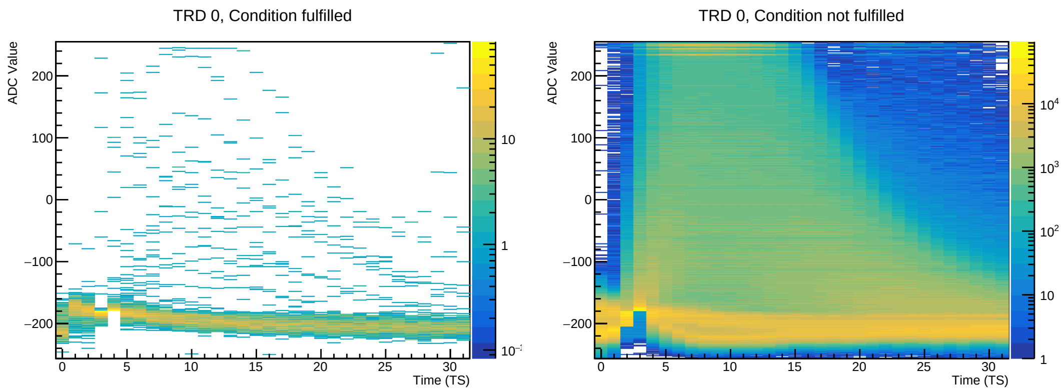

Figure 4.18.: Self triggered hit messages from TRD 0, which do fulfill the trigger condition (left panel) and do not (right panel). The data is taken from one TSA file of run 88.

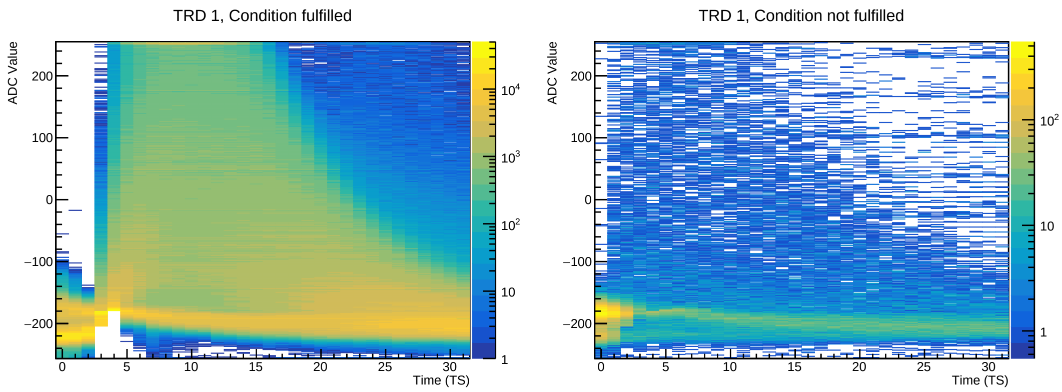

Figure 4.19.: Self triggered hit messages from TRD 1, which do fulfill the trigger condition (left panel) and do not (right panel). The data is taken from one TSA file of run 88.

Contrary to the expectation, on the SPADIC on TRD 0 only about 0.05 % of all self-triggered hit messages fulfill the trigger condition. Furthermore, the overlay of signal shapes not fulfilling the condition shows a sharp decrease in entries below an ADC value of -205 at sample[2] and below -180 at sample[3], hence, at the ADC values of the set thresholds, but one sample too early. Therefore, the data indicates that in this run, this SPADIC transmitted one presample less, thus checking its trigger condition one sample earlier in the hit message. As full messages from this SPADIC still have 32 samples, it does not seem to be caused by the loss of one presample at some point in the transmission. Also, the number of presamples is an intrinsic property of the SPADIC, which, under normal circumstances should not be changeable. Hence, this effect could not be caused by a wrong configuration.
The SPADIC on TRD 1 on the other hand works mostly as expected, with only 2.24 % of messages failing to fulfill the trigger condition. Since the condition is applied to sample[2], sample[3] and sample[4] of each hit message, a message needs to have at least 5 samples to fulfill it. This leads to all messages with less than 5 samples being flagged as "not fulfilling the condition" and plotted into the right panel. This is noticeable in the data, as the majority of entries on the right panel of Figure 4.19 are indeed in the first three bins on the X-axis.

When comparing different runs, it was noticed that in some runs, all SPADICs behave as expected (as in Figure 4.19), while in others, the SPADICs on TRD 0 (the one in the beam spot as well as the one in front of the iron source), TRD 3, and the SPADIC on the 2012-type chamber could show the behaviour seen in Figure 4.18. A full list of the number of presamples transmitted by each SPADIC in each viewed run can be found in Table A.1. As can be seen, the number of presamples does not switch randomly between 1 and 2, but stays mostly constant over several runs before changing. As both times, in which a resynchronization of the SPADICs was noted, the number of presamples transmitted by at least one SPADIC changed, it is suspected that an error in the sychronization process could be cause of this behaviour[3]. This assumption is also supported by the fact that the clock of each SPADIC which is missing one presample, is also out of synchronicity by one epoch, as was descibed in Section 4.1.2.1 (in that case for the SPADIC on TRD 0 in run 88).
When a resynchronization is conducted, the 160 MHz clock signal of the AFCK is passed down to the SPADIC, which locks to every 10th period to generate its internal clock frequency of 16 MHz, while it is not clear if the whole ASIC locks to this frequency monolithically, or individually for each of its segments. If the latter is the case, there could be the possiblilty of a phase shift between the clocks of the hit logic and the message builder, which could result in one sample less at the start of the message and a sample more at the end of it.

[3] It is worth noting that unfortunately, not every resynchronization process was written down. Hence, inbetween runs where the number of presamples changed, a resynchronization can have been done.

4.1.6. Baseline

4.1.6.1. Baseline Position and Width

As absolute trigger thresholds were used during the whole measurement campaign, a precise knowledge about position, width and time behaviour of the baseline is crucial. For this purpose, the three following methods to determine the baseline have been tested:

1. Taking the first sample of self-triggered messages (sample[0])

2. Taking the second sample of self-triggered messages (sample[1])

3. Taking the last sample of neighbour-triggered messages with small maximum ADC values (sample[31])

The positions of the named samples are fixed to the relative position of the pulse via the trigger codition, and thus, all carry information about the baseline. Method 1 is an obvious choice, since the presamples were implemented especially for the purpose of baseline calculation. But as the first presample is missing in the data of some SPADICs in various runs (see Section 4.1.5), methods 2 and 3 were proposed as possible workarounds. Generally, the baseline of each channel was calibrated to be at the ADC value of -220 at the initialization of the Data Acquisition (DAQ) chain, but since the measurement interval for this calibration has been chosen to be rather short, deviations from the value of -220 are expected. Furthermore, triggering all channels at once, as it was done for the calibration, causes the buffer of certain channels (see Section 3.3.1) to fill up, resulting in the SPADIC discarding all messages from channels 8, 14, 24 and 30 (8 and 14 on both half chips). Thus, these channels could not calibrated automatically.

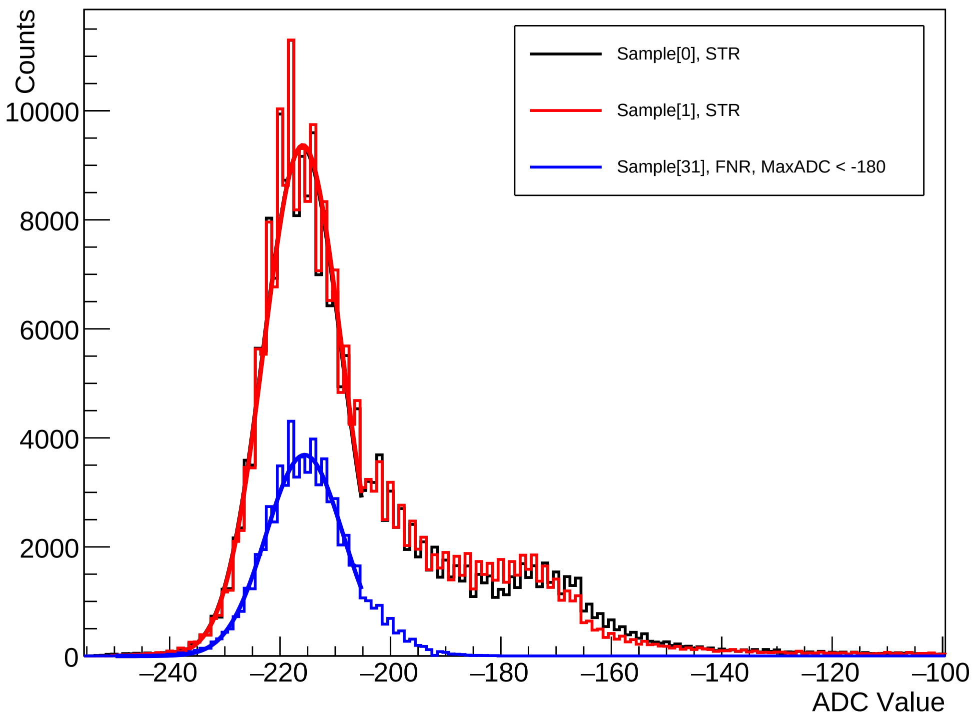

Figure 4.20.: ADC spectra of the samples used for the three proposed methods for baseline determination, each fitted with a Gaussian function. The resulting fit parameters can be found in Table 4.3. The data was taken from one channel in the beam spot. Here, also the slight suppression of every second ADC value on this channel is noticable (see Section 4.1.4).

To compare the three mentioned methods, the baseline was at first assumed to be static and the spectra of sample[0], sample[1] and sample[31] on one channel in the beam spot were compared (Figure 4.20). As can be seen, the spectra of sample[0] and sample[1] nearly coincide. Since, in most cases, sample[2] will be still beneath the lower trigger threshold and the signal shape has a short rising time of 240 ns ($\equiv$ 3.84 TS), it was to be expected that the signal does not rise significantly between sample[0] and sample[1]. On the right side of both of these spectra, there is a "shoulder" of values considerably higher than the calibrated baseline. This is caused by triggering on the falling tail of a previous signal, as already described in Section 4.1.4. The first and second samples of these signals do not carry any information about the baseline. Hence, the Gaussian fit is only applied in the range of -256 to -205 ADC.
The ADC spectrum of sample[31] naturally does not have the "shoulder" of higher ADC values, and has generally less entries, as a cut for signals with $\mathrm{ADC}_{\mathrm{max}} > -180$ was applied. Furthermore, the position of the maximum de-

termined by the fit for sample[31] is higher than the ones for sample[0] and sample[1]. Therefore, it was investigated if this is systematic dependence.

Table 4.3.: Parameters of Gaussian fit functions applied to ADC spectra for baseline determination. The spectra and the Gaussian functions can be seen in Figure 4.20.

Fitted Spectrum	Constant	Mean (ADC)	Sigma (ADC)	χ^2_{red}
Sample[0], STR	9340.67 ± 30.23	-215.96 ± 0.02	7.03 ± 0.02	81.11
Sample[1], STR	9370.21 ± 30.35	-215.87 ± 0.02	7.04 ± 0.02	84.21
Sample[31], FNR, $\mathrm{ADC_{max}} < -180$	3686.67 ± 19.21	-215.56 ± 0.04	6.95 ± 0.03	20.95

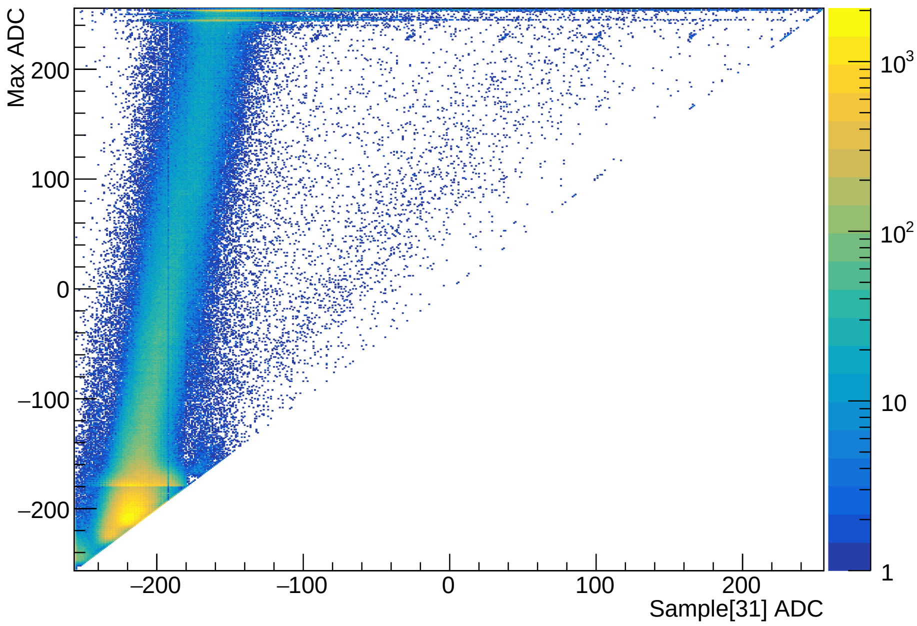

Figure 4.21.: Maximum ADC value plotted against the ADC value of sample[31] for self or neighbour triggered messages on all channels of SPADIC 0.

In Figure 4.21 the maximum ADC value is plotted against the value of sample[31] for trigger types 1,2 and 3 on all channels of SPADIC 0. A clear correlation between the two quantities can be observed. This is due to the relatively slow exponential decrease of the shaper response (see Equation 3.1). By inserting $t = t_{31}$ and $A = \mathrm{ADC_{Max}} \cdot e$ in Equation 3.1 one gets for the value of sample[31]:

$$f(t_{31}) = \mathrm{ADC_{Max}} \cdot \frac{t}{\tau} \cdot \exp\left(-\frac{t}{\tau} + 1\right). \tag{4.10}$$

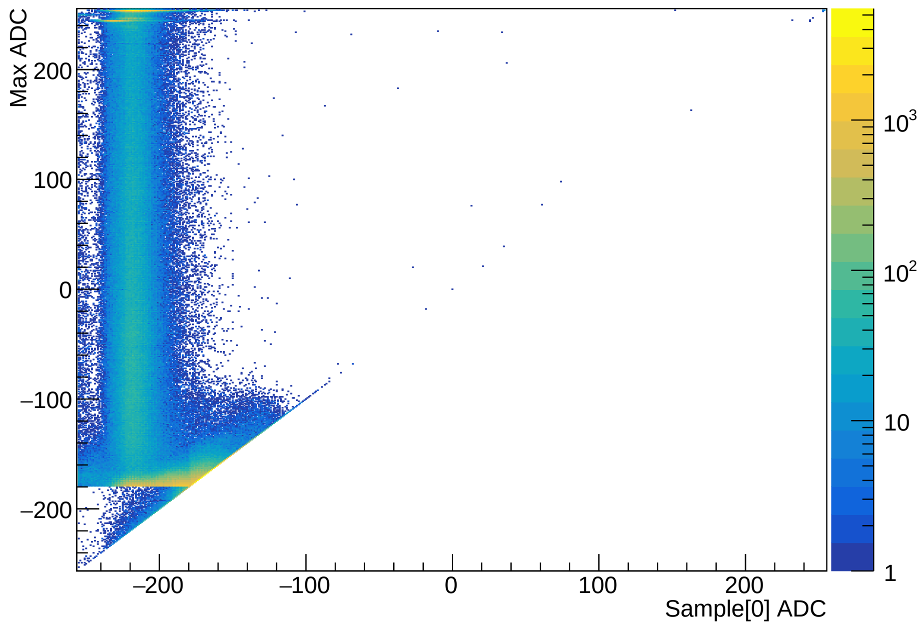

Figure 4.22.: Maximum ADC value plotted against the ADC value of sample[0] for self-triggered messages on all channels of SPADIC 0 .

As a first approximation for the time of sample[31], $t_{31} \approx 29 \cdot 62.5\,\text{ns}$ was used, since the signal described by Equation 3.1 starts at about the first trigger sample, resulting in sample[31] being 29 samples behind the start of the signal. With a shaping time of $\tau = 240\,\text{ns}$ this results in

$$f(t_{31}) \approx 0.01 \cdot \text{ADC}_{\text{Max}}, \tag{4.11}$$

hence, the value of sample[31] being at about 1% of the maximum ADC value. As Equation 3.1 describes the shaper response to a δ-peak, the response to a real physical signal will be longer, resulting in the sample[31] being higher than 1% of ADC_{Max}.
Even though no correlation between either sample[0] or sample[1] and ADC_{Max} was expected, it was still examined. In Figure 4.22 and Figure 4.23, the maximum ADC value is plotted against sample[0] and sample[1], respectively. Here, no clear correlation can be observed.

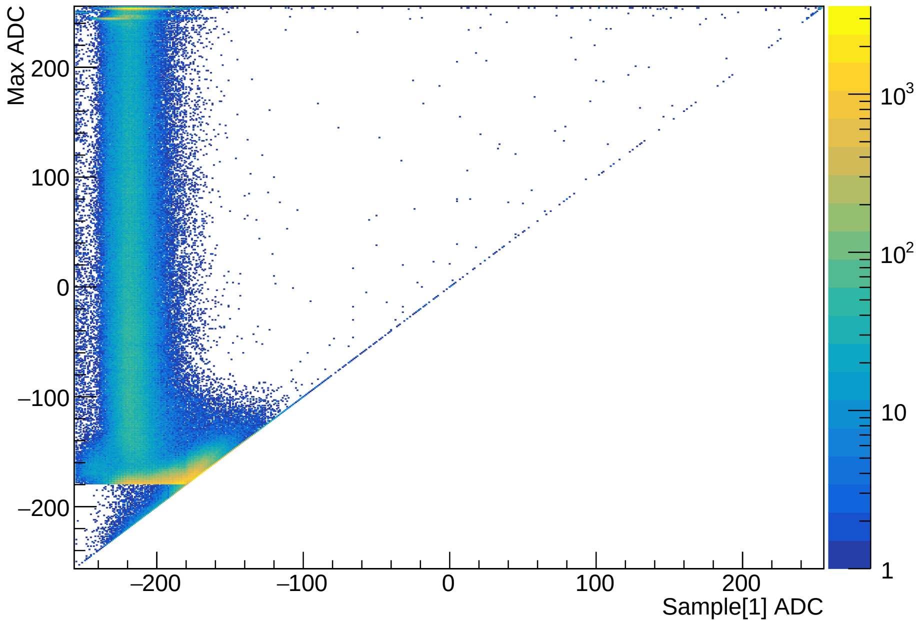

Figure 4.23.: Maximum ADC value plotted against the ADC value of sample[1] for self-triggered messages on all channels of SPADIC 0 .

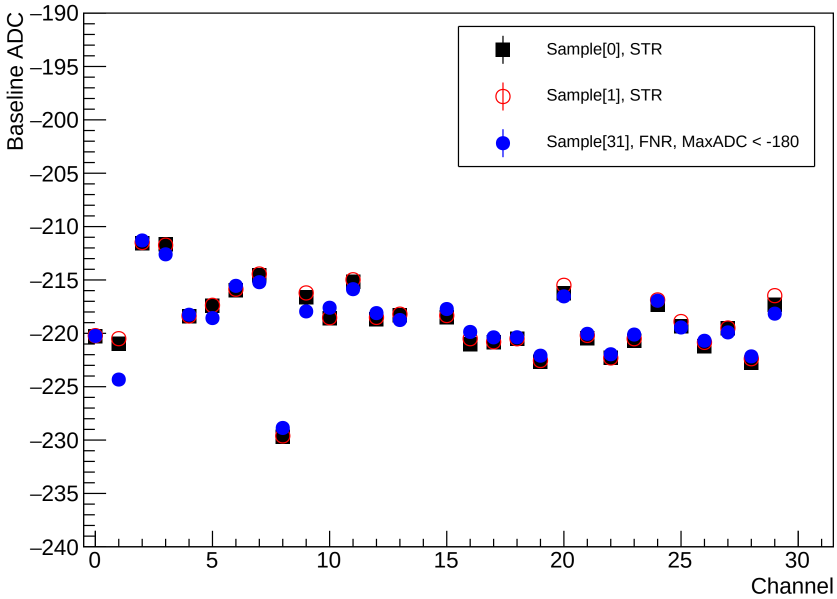

Figure 4.24.: Baseline positions on SPADIC 0 determined by Gaussian fits for the sample[0], sample[1] and sample[31] methods.

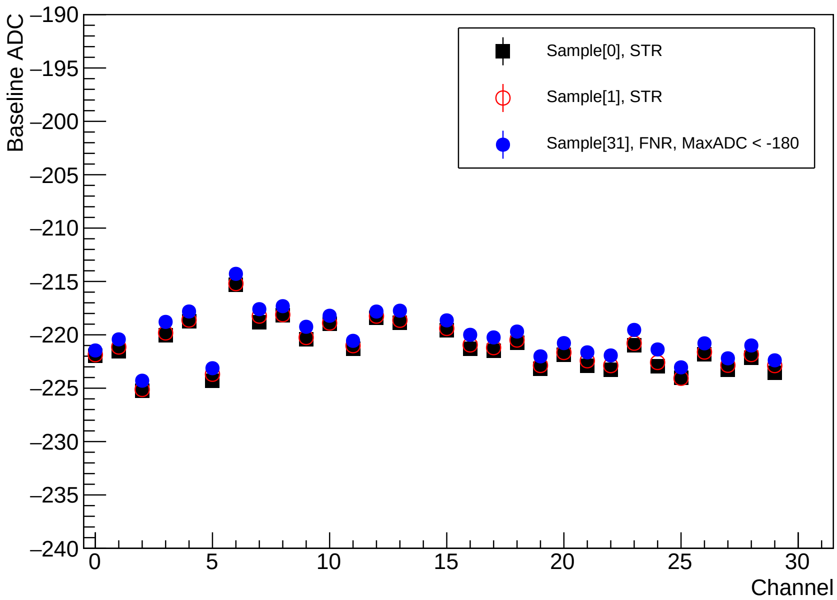

Figure 4.25.: Baseline positions on SPADIC 3 determined by Gaussian fits for the sample[0], sample[1] and sample[31] methods.

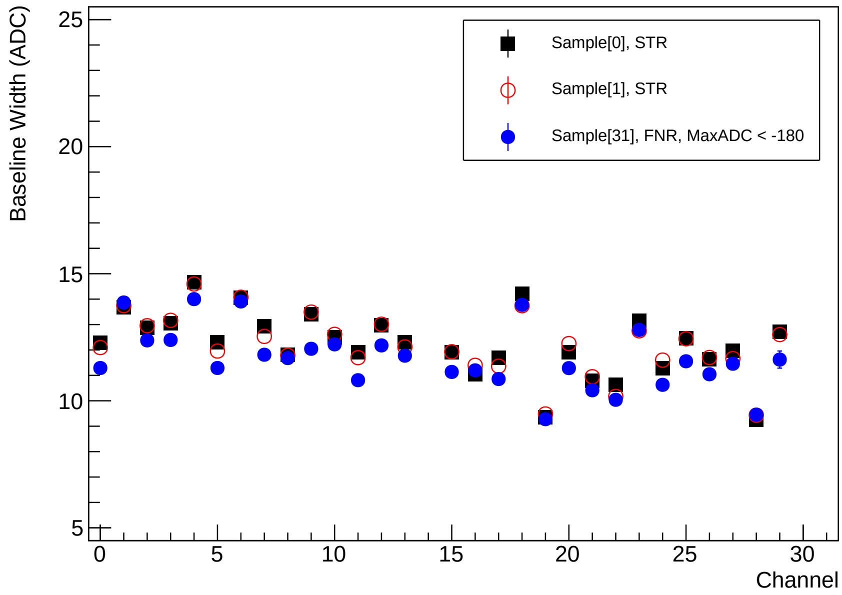

Figure 4.26.: Baseline widths on SPADIC 0 determined by Gaussian fits for the sample[0], sample[1] and sample[31] methods.

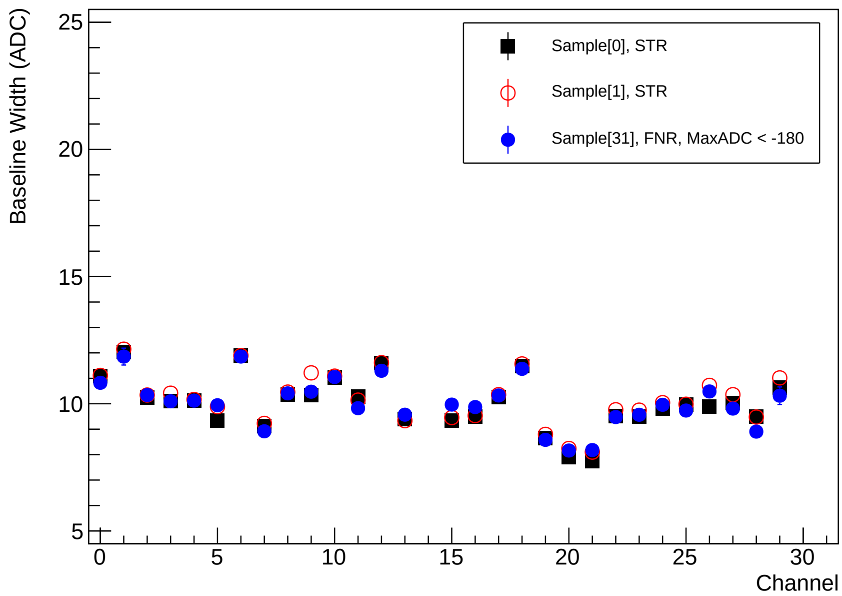

Figure 4.27.: Baseline widths on SPADIC 3 determined by Gaussian fits for the sample[0], sample[1] and sample[31] methods.

As a next step, the positions the baselines determined by the Gaussian fits were compared for the different channels on the SPADICs. For the SPADICs 0 and 3 this can be seen in Figure 4.24 and Figure 4.25, while the same histograms for SPADICs 6 and 9 can be found in the appendix (Figure A.13 & Figure A.14). As expected, the baseline positions on all channels deviate from the calibrated position of -220, with the strongest deviation being mostly on the not calibrated channels (8,14 & 24). On SPADICs 3 and 6 the values calculated by the three different methods are also very close to each other and, in accordance with the results shown before, the value calculated by sample[0] is always the lowest, followed by sample[1], while sample[31] gives the highest value. For the most part, this is also true for SPADIC 0, while deviations from this could be caused by greater fluctuations of the baseline, indicated by its greater width on SPADIC 0 (see below). SPADIC 9 was part of a different production revision, and its chip was soldered by hand to the FEB and not, like the other three, mechanically. This is a likely explanation for its slightly different behaviour.
The width of the baseline here is defined as two times the standard deviation σ of the Gaussian fit. The determined widths of the baselines on SPADICs 0 and 3 are plotted in Figure 4.26 and Figure 4.27, histograms showing the widths on SPADICs 6 and 9 are located in the appendix (Figure A.15 & Figure A.15). Generally, the widths are much larger than expected, as random analog noise was calculated to be less than 2 ADC values (see Section 3.3.5). For the most part, the method using sample[31] gives smaller baseline widths, presumably since the cut for signals with small maximum ADC values reduces the total range of possible values for sample[31]. Furthermore, it is not affected by retriggering on the falling tail of previous signals, even though the impact of this effect on the two other methods was alleviated by decreasing the fit range.

4.1.6.2. Baseline Behaviour with Time

As stated above, the large width of the baseline indicates fluctuations or oscillations. This was investigated by analyzing the temporal behaviour of the calculated baseline on several timescales. Firstly, the mean baseline positions and widths for 46 consecutive TSA files were determined, accounting for 833 s ($\approx$ 14 min) of recorded data. In Figure 4.28 and Figure 4.29 the results on one of the channels on SPADIC 0 located in the beam spot (channel 6) are plotted. Evidently, the baseline position does change over time, even though this change is very small (about 1 ADC). By comparing the values for the different calculation methods, one can distinguish between random/statistical fluctuations and actual shifts of the baseline, since the latter should be visible in the results of all three methods. In Figure 4.29 three clear discontinuities, in which the baseline width drops significantly, can be observed, located at around 100 s, 450 s and 780 s, respectively. In the time of recording of these three TSA

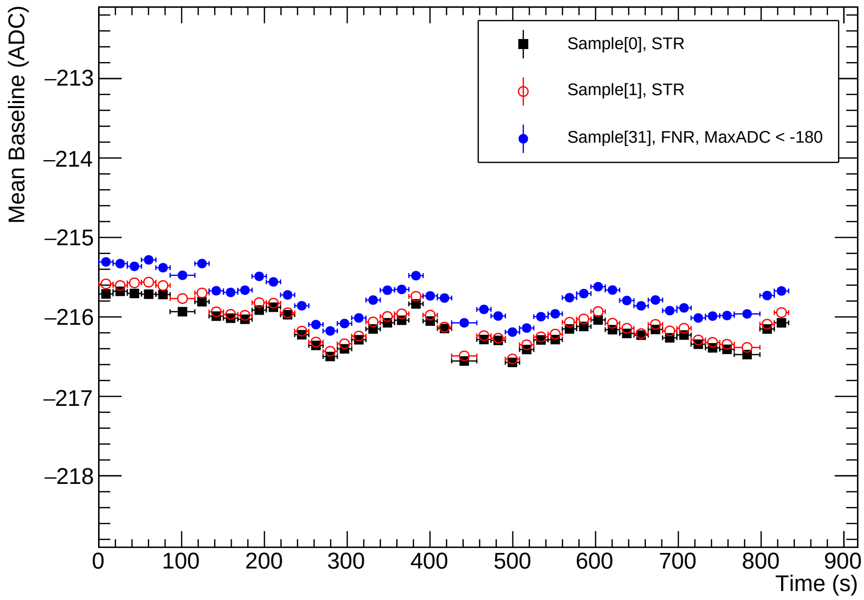

Figure 4.28.: Baseline positions on channel 6 of SPADIC 0 determined by Gaussian fits for the Sample[0], sample[1] and sample[31] methods plotted against time.

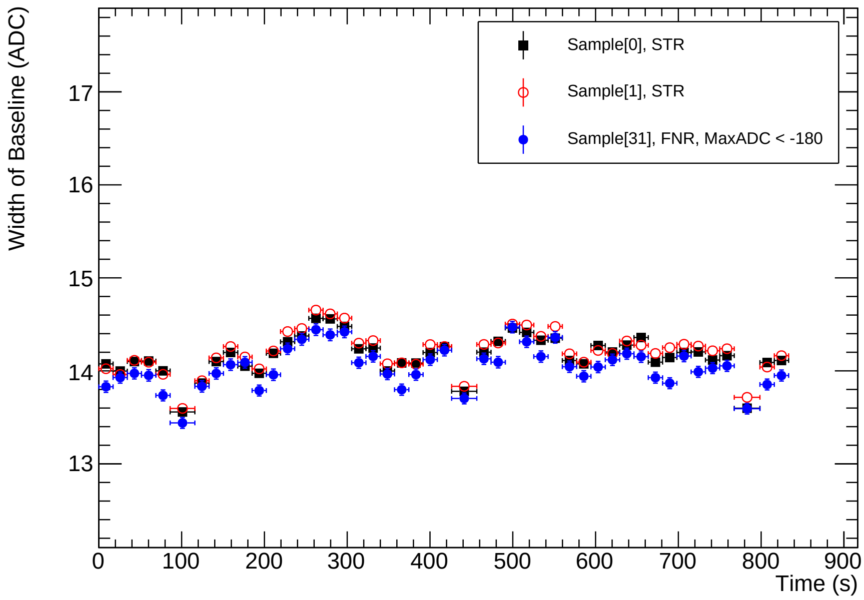

Figure 4.29.: Baseline widths on channel 6 of SPADIC 0 determined by Gaussian fits for the Sample[0], sample[1] and sample[31] methods plotted against time.

files, a "PETRA III top-up" (see Section 3.1.2) happened, resulting in almost no incoming data for half of the time recorded in these files. As a TSA file is limited in data size and not in time of recording, these three files span over a longer time than the other files as indicated by the larger horizontal error bars. Why the baseline position and especially its width drops significantly at a PETRA III top-up is not yet fully clear. While it could also be a reconstruction artifact, it would otherwise suggest a load dependence, though a verification of this is non-trivial. If a higher load, quantified by an increased hit rate, would raise baseline position and width, so would a raised baseline position and width increase the hit rate since absolute thresholds were used. For a disentaglement of these two effects, more refined measurements and analysis have to be conducted, exceeding the scope of this thesis.

On the left side of Figure 4.29 an oscillation of the width with a period of about 100 s seems to be visible. To check for correlations between different channels, the baseline positions and widths determined by using sample[0] on four channels were plotted in Figure 4.30 and Figure 4.31. Here the 100 s oscillation is also visible on channel 4. Since the channels 5 and 7, as well as the channels 4 and 6 behave very similarly to each other, it can be concluded that the baselines of neighbouring pads are correlated. As channel 4 and 6 were located in the beam spot, thus receiving higher statistics, they have generally less statistical fluctuations, but are affected more strongly by the PETRA top-ups.

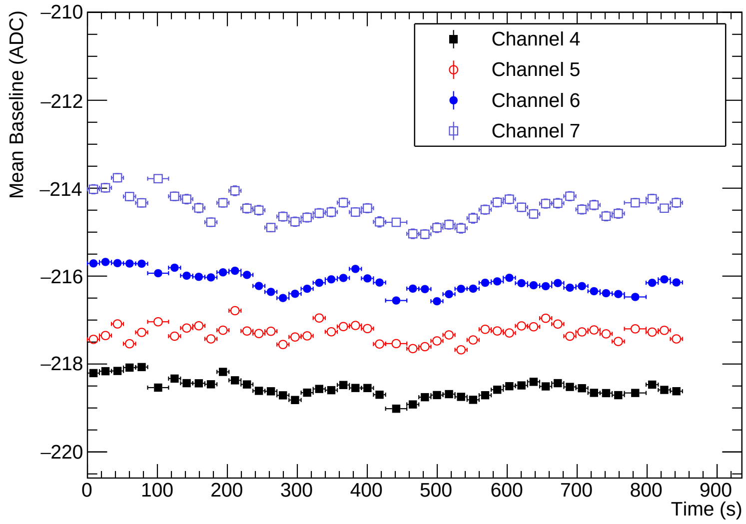

Figure 4.30.: Baseline positions on channels 4-7 of SPADIC 0 determined by Gaussian fits for the Sample[0] plotted against time. The channels 4 and 6 correspond to pads located in the beam spot, the pads of channels 5 and 7 were located outside of it. One data point equals one TSA file.

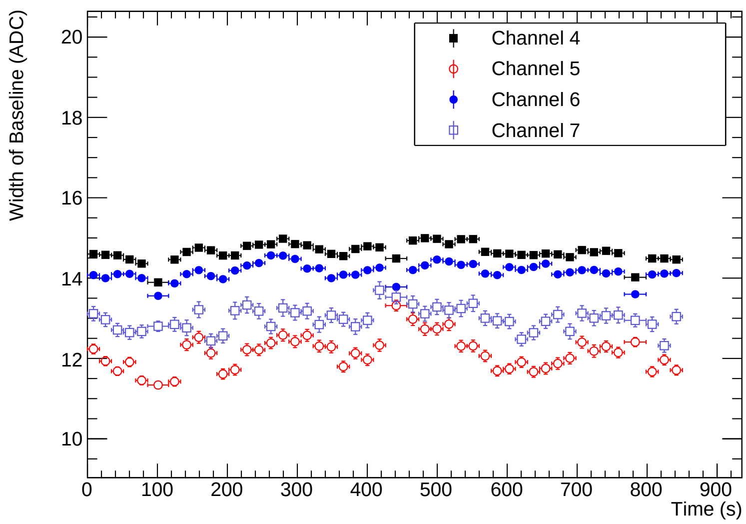

Figure 4.31.: Baseline widths on channels 4-7 of SPADIC 0 determined by Gaussian fits for the Sample[0] plotted against time. The channels 4 and 6 correspond do pads located in the beam spot, the pads of channels 5 and 7 were located outside of it. One data point equals one TSA file.

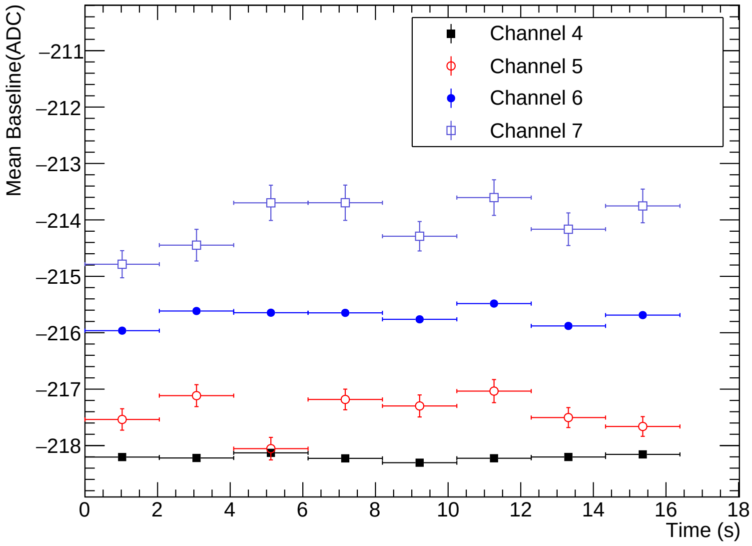

Figure 4.32.: Baseline positions on channels 4-7 of SPADIC 0 determined by Gaussian fits for the Sample[0] plotted against time. The channels 4 and 6 correspond to pads located in the beam spot, the pads of channels 5 and 7 were located outside of it. One data point equals 20 Timeslices = 2.048 s of data.

As a next step, variations of baseline width and position within one TSA file were investigated. Here a sampling interval of 20 Timeslices = 2.048 s was chosen. The baseline widths and positions of the same channels as above are plotted in Figure 4.32 and Figure 4.33. In general, the changes of the baseline on the channels in the beam spot are fairly small, mostly below 0.5 ADC and, in contrast to the results from longer timescales, a correlation between the two is not evident. As statistics decrease for smaller time windows, the errors for channels outside of the beam spot become quite large, complicating a statement about oscillations with these small amplitudes. Since the errors will increase for even smaller time windows, an analysis of high frequency effects on the baseline was not done with the previous methods.

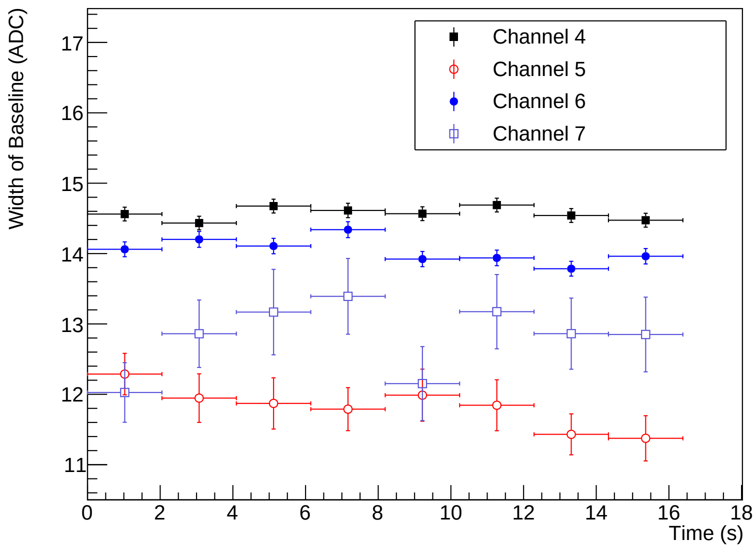

Figure 4.33.: Baseline widths on channels 4-7 of SPADIC 0 determined by Gaussian fits for the Sample[0] plotted against time. The channels 4 and 6 correspond to pads located in the beam spot, the pads of channels 5 and 7 were located outside of it. One data point equals 20 Timeslices = 2.048 s of data.

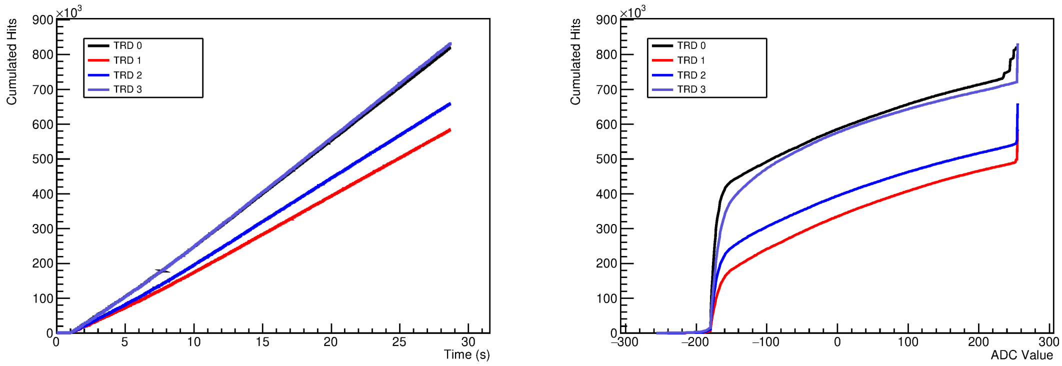

Figure 4.34.: Cumulated self-triggered hit messages (triggertypes 1 &3) from all four TRDs plotted against time (left panel) and against their maximum ADC value (right panel).

4.1.7. Hit Message Frequencies and Noise

When comparing the total amount of self-triggered hits (triggertypes 1 & 3) per detector over time (left panel of Figure 4.34), a vast difference between the four TRDs can be seen, with TRD 0 and 3 registering many more hits than the TRDs 1 and 2. Since the beam spot on TRD 3 was located close to the border between the two pad rows, the charge was distributed between more pads, explaining the higher hit rate to some extent. From the cumulated maximum ADC spectrum (right panel) it becomes clear that the difference between the detectors comes mainly from hits with very low maximum ADC values. To check if this noise was correlated with the electron beam, the hit message frequencies were plotted against time (Figure 4.35 and Figure A.17). The hit message frequencies were calculated by counting every self-triggered hit message in a time window of $6 \cdot 10^4$ TS ($\equiv 3.75\,\mathrm{ms}$) and then dividing this number by the length of the time window. This is not equivalent to a real physical hit frequency, since charge clusters with more than one self-triggered pad are counted multiple times, but it should be proportional to it.
In Figure 4.35, the 12.5 Hz spill structure of the electron beam is visible very clearly. Furthermore, it can be seen that every second spill has an decreased intensity due to higher beam loss at lower energies and matches Figure 3.4 very well. In contrast to the other three TRDs, TRD 0 registers a low, but noteworthy amount of hits also between the spills, indicating uncorrelated noise. By investigating the hit message frequency per channel, it was noticed that this uncorrelated noise appears mostly on the channels 0 and 1, which were not located in the beam spot. The hit message frequency without channels 0 and 1 is plotted in Figure 4.36. As can be seen, without channels 0 and 1, amount of hit messages on TRD 0 between the spills has decreased significantly, but the hit message frequency in the spills is still higher than on TRD 1. The results of

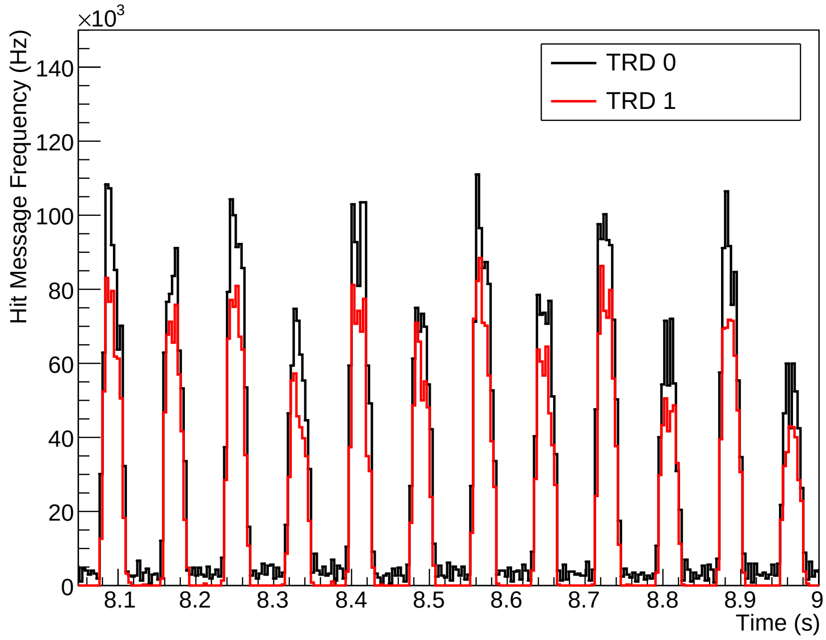

Figure 4.35.: Hit message frequency on TRD 0 and TRD 1 plotted against time. The data was taken from run 97 at a beam momentum of 4 GeV/c.

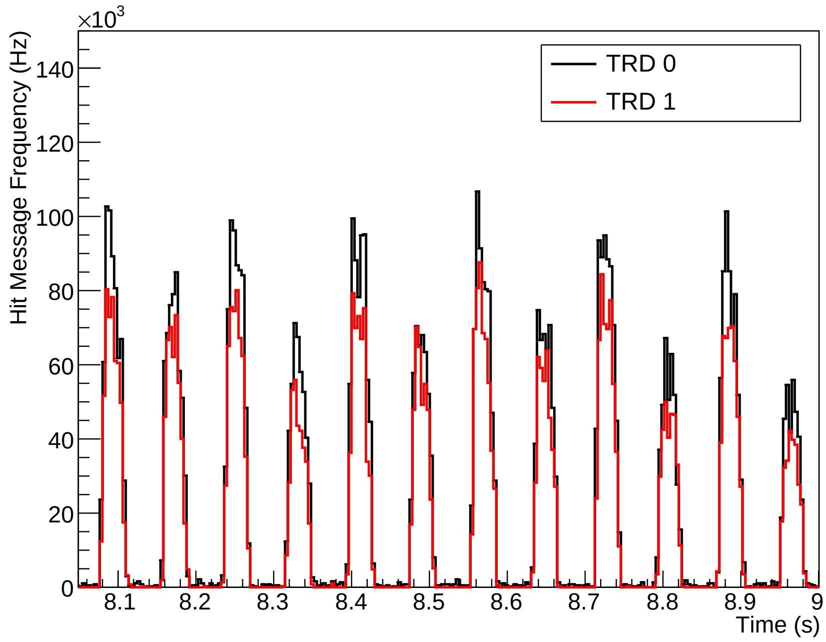

Figure 4.36.: Hit message frequency on TRD 0 and TRD 1 after excluding all hits from the channels 0 and 1 plotted against time. The data was taken from run 97 at a beam momentum of 4 GeV/c.

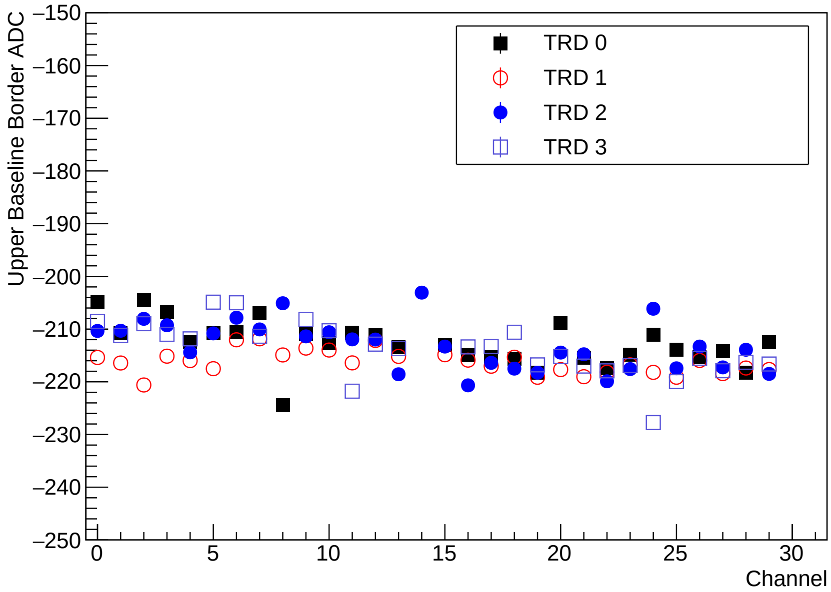

Figure 4.37.: Sum of baseline position and half of its width for each channel on each TRD, calculated with the sample[1] method (see Section 4.1.6), since one presample was missing on TRD 0. The data was taken from run 97 at a beam momentum of $4\,\mathrm{GeV}/c$.

the baseline analysis (see Section 4.1.6) showed, that on the TRDs 0 and 3, the baseline width is generally a few ADC values higher than on the TRDs 1 and 2. An upper "border" of the baseline, can be calculated by adding the baseline's position b and half of its width σ_b

$$\hat{b} = b + \sigma_b, \tag{4.12}$$

which was then plotted for each TRD to be compared (Figure 4.37). On the most active channels (3,5,7,9 & 11), the baselines of TRD 0 and TRD 3 generally have a higher upper border of the baseline, making retriggering on falling tails especially likely on these detectors, as the baselines are closer to the trigger thresholds. Hence, the cut for these type of noise signals (see Equation 4.9) was applied also to this frequency calculation. The results can be seen in Figure 4.38 and Figure A.19. Even though the resulting hit message frequencies decreased for all four TRDs, the cut had, as expected, the greatest impact on the TRDs 0 and 3. After applying the cut, the hit message frequencies of the TRDs 0, 1 and 2 have similar amplitudes, while TRD 3's frequency is slightly higher, caused by its rotation by 90° as stated above.

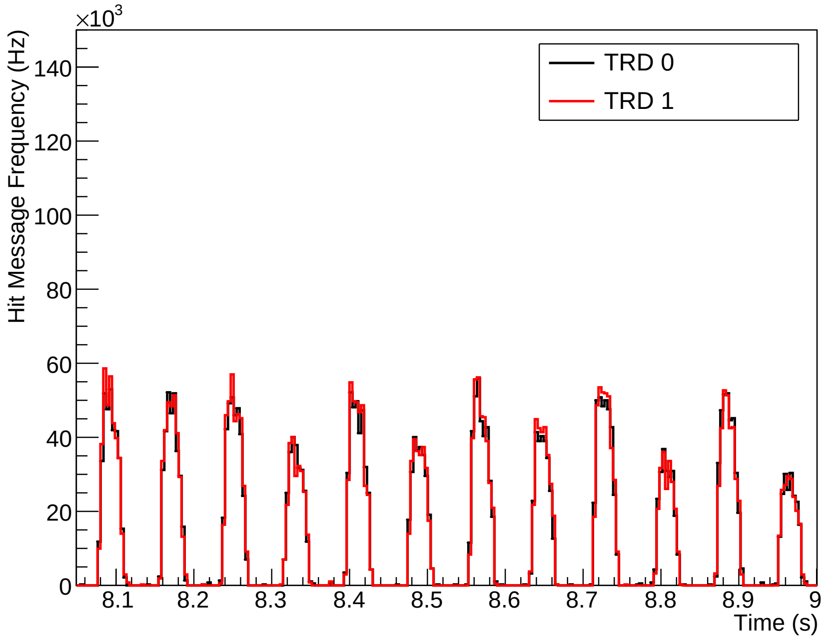

Figure 4.38.: Hit message frequency on TRD 0 and TRD 1 after excluding all hits from the channels 0 and 1 and applying the cut for tail retriggering (Equation 4.9) plotted against time. The data was taken from run 97 at a beam momentum of 4 GeV/c.

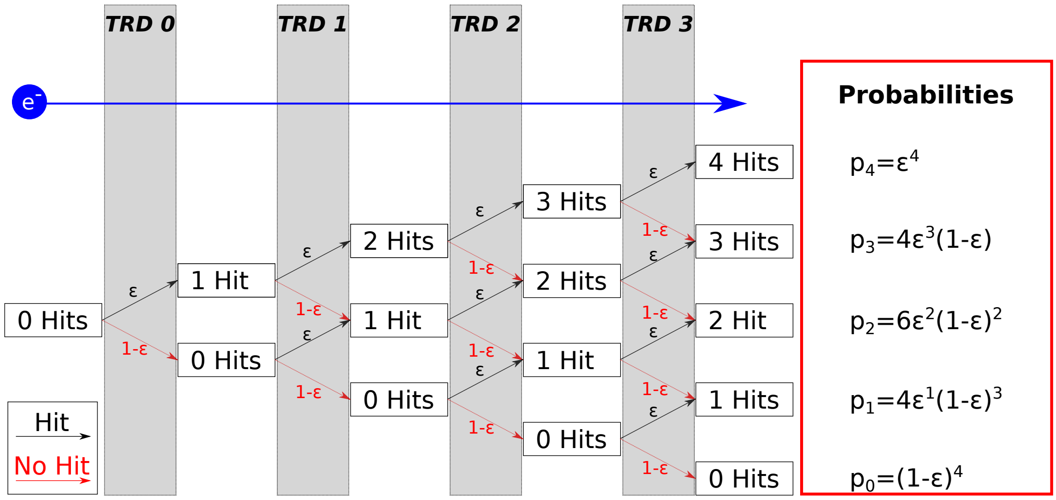

Figure 4.39.: Visualization of the probabilities of an electron being detected by any number of the four TRDs under the assumption of the same efficiency ε in each detector.

4.2. Efficiency

4.2.1. System Efficiency via Binomial Distribution

To evaluate the overall system efficiency, the SDs were used as reference detectors: At every coinciding signal from both SDs, the number of TRDs also detecting a hit was counted. Under the assumption of each single TRD having the same efficiency ε, a binomial distribution is expected, as visualized in Figure 4.39. As the time difference distribution between a coincidence in the SDs and a hit in one of the TRDs is broader than 1 TS (see Section 4.1.2.2), a reasonable coincidence window had to be chosen. Based on the shape of the peak in Figure 4.5, the window should include at least all hits with $\Delta t = \pm 2\,\mathrm{TS}$. Since the closest expected time between two electrons in the beam is 15.61 TS and hence, will be measured as either 15 TS or 16 TS, the window should not be larger than $\Delta t = \pm 14\,\mathrm{TS}$. To compare the signals included in coincidence windows with different lengths, the maximum ADC spectra of self-triggered correlated hits were plotted for each TRD (Figure 4.40 and Figure A.20 - A.22). As can be seen, the spectra behave almost identical at maximum ADC values above -100, and deviate the more, the closer the maximum ADC is to the upper threshold $T_2 = -180$. For wider coincidence windows (i.e. 5 TS or 8 TS), the spectra show a peak similar to the one caused by tail retriggering in the spectrum without cut (black line), indicating that these entries are noise. Thus, a coincidence window of $\pm 3\,\mathrm{TS}$ was chosen, while keeping results for the windows of $\pm 2\,\mathrm{TS}$ and $\pm 4\,\mathrm{TS}$ as reference values.
Since the maximum ADC spectra indicate very low noise in the sample of correlated hits, no further cuts were applied. Now, for every coincidence in the

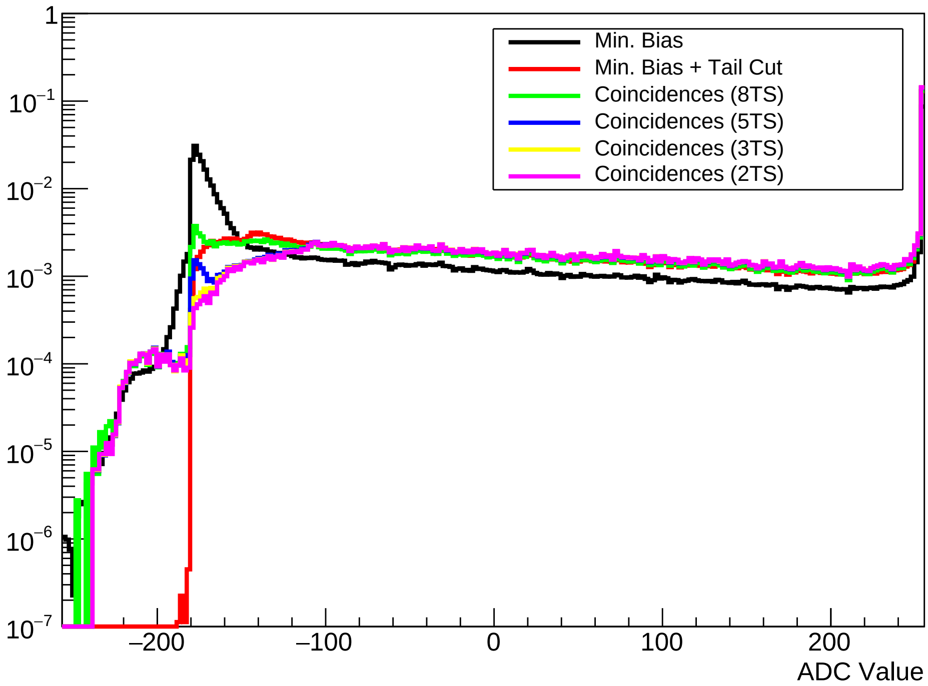

Figure 4.40.: Normalized maximum ADC spectra of all self-triggered hits on TRD 2 without cut (black), all self-triggered hits after applying the cut for retriggering on falling tails (Equation 4.9) (red), and self-triggered hits in different coincidences windows (green, blue, yellow and pink). For the latter ones, no further cut was applied. The data was taken from 10 consecutive TSA files from run 97 at a beam momentum of 4 GeV/c.

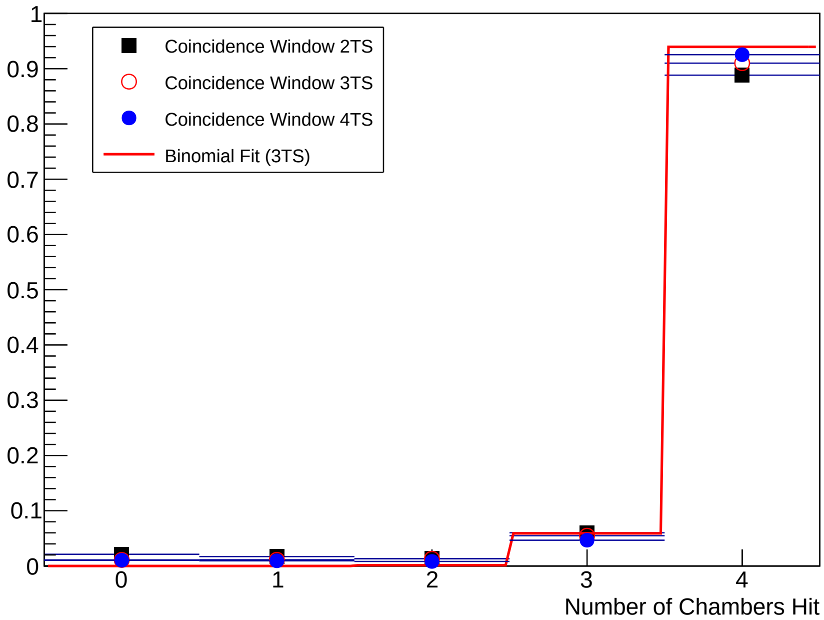

Figure 4.41.: Normalized coincidence distributions of the four TRDs for different coincidence windows. For the window of ± 3 TS also a binomial fit is shown. The fit parameters for all three windows can be found in Table 4.4.

SDs it was counted, how many TRDs register a hit in the chosen time windows. Hereby, all trigger types and and channels were considered, but more than one hit in the same window were still counted as only one, as at least three hit messages per incident electron are expected due to FNR (see Section 3.3.2). The inclusion of triggertype 2 was done to alleviate the effects of the data loss in the channel switch (see Section 3.3.4) and is further discussed in Section 4.2.2. Hence, an SD coincidence was flagged as "detected" on a TRD if at least one channel registered a hit in the time window, and flagged as "not detected" only if no channel registered a hit. The results for data from 10 TSA files of run 97 at a beam momentum of 4 GeV/c can be seen in Figure 4.41 and Figure 4.42, together with a binomial fit for the data from a coincidence window of ± 3 TS. The fit was also applied to the data from the other two windows, the resulting fit parameters can be found in Table 4.4.

As can be seen, while the general shape of the data is similar to the expected binomial distribution, it deviates significantly from the fit, visible also in the large values for χ^2_{red} (see Table 4.4). This can be caused by either random coincidences, or by different overlaps of the active areas of the individual TRDs with the SDs.

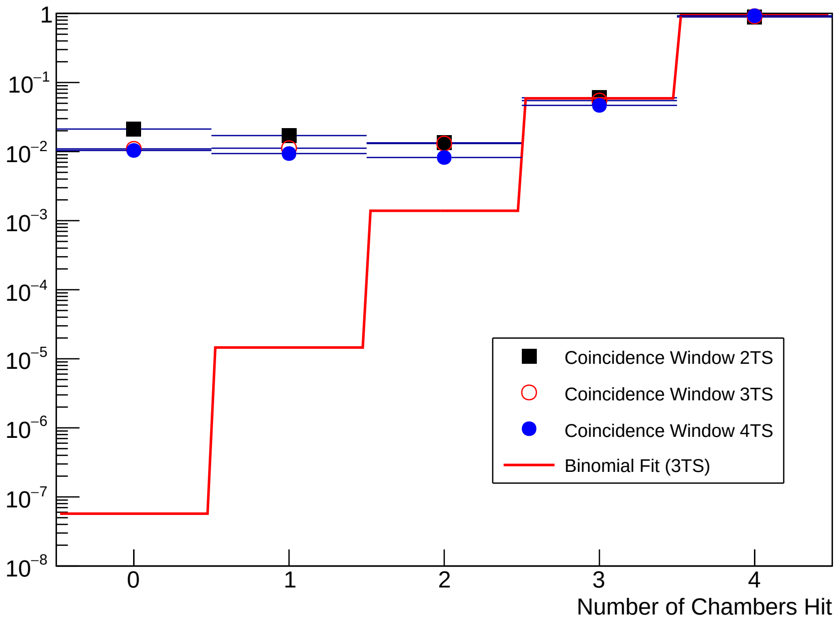

Figure 4.42.: Normalized coincidence distributions of the four TRDs for different coincidence windows on a logarithmic scale. For the window of ±3 TS also a binomial fit is shown. The fit parameters for all three windows can be found in Table 4.4.

Table 4.4.: Parameters of binomial fits for coincidence distributions with different coincidence window lengths: The data and the fit (only for ±3 TS) can be seen in Figure 4.41.

Coincidence Window (TS)	Efficiency ε (%)	χ^2_{red}
±2	98.26 ± 0.02	1561.93
±3	98.45 ± 0.02	1034.60
±4	98.87 ± 0.02	822.83

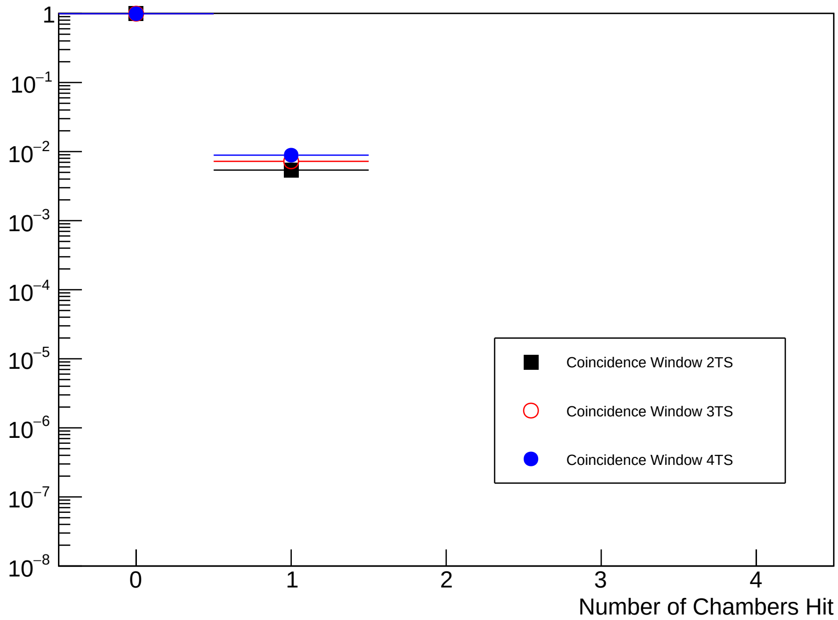

Figure 4.43.: Normalized coincidence distributions of the four TRDs for different coincidence windows after shifting the data of each detector (SDs were kept as one unit) relative to each other in time by $n \cdot 80\,\text{ms}$.

To check the amount of random coincidences, the data coming from each individual TRD was given a time shift, each a different multiple of the 80 ms DESY II magnet cycle causing the spill structure of the beam (see Section 3.1.2). Since the data should be completely uncorrelated after applying these shifts, only random coincidences are expected. The resulting coincidence distribution using the same data as for Figure 4.42 is plotted in Figure 4.43. As can be seen, no random coincidences of the SDs and more than one TRD occur. Most importantly, when investigating the distribution of random coincidences other the TRDs, it was noticed that they *only* occur on TRD 0. This was then compared with the distribution of single coincidences (i.e. coincidences of the SDs and only one TRD) over the TRDs, which can be seen in Figure 4.44. Since the single coincidences visible in Figure 4.44 occur mainly on TRD 3 and not on TRD 0, they are interpreted as actual correlated events, and not as random coincidences.

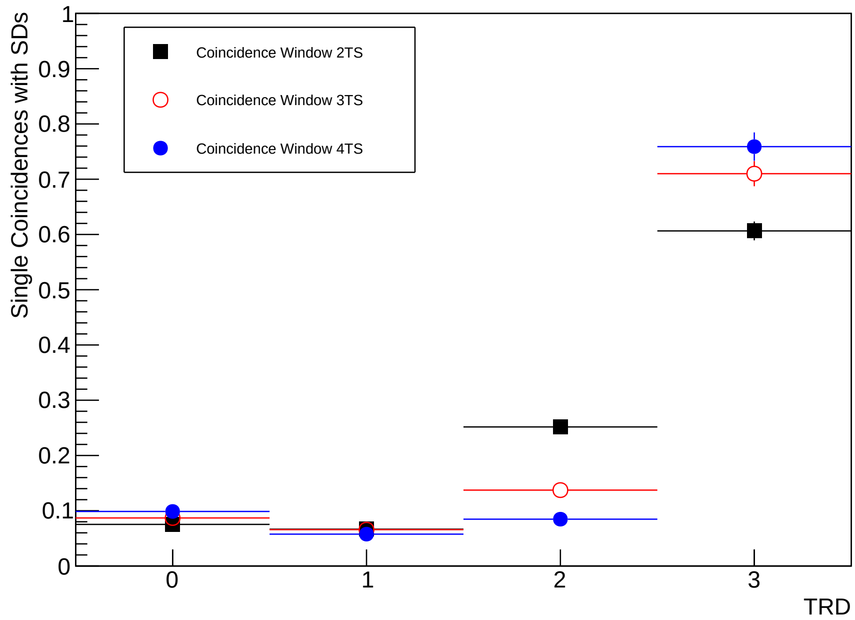

Figure 4.44.: Normalized distributions of coincidences of the SDs and only one TRD for different coincidence windows: The data was taken from 10 consecutive TSA files of run 97 at 4 GeV/c.

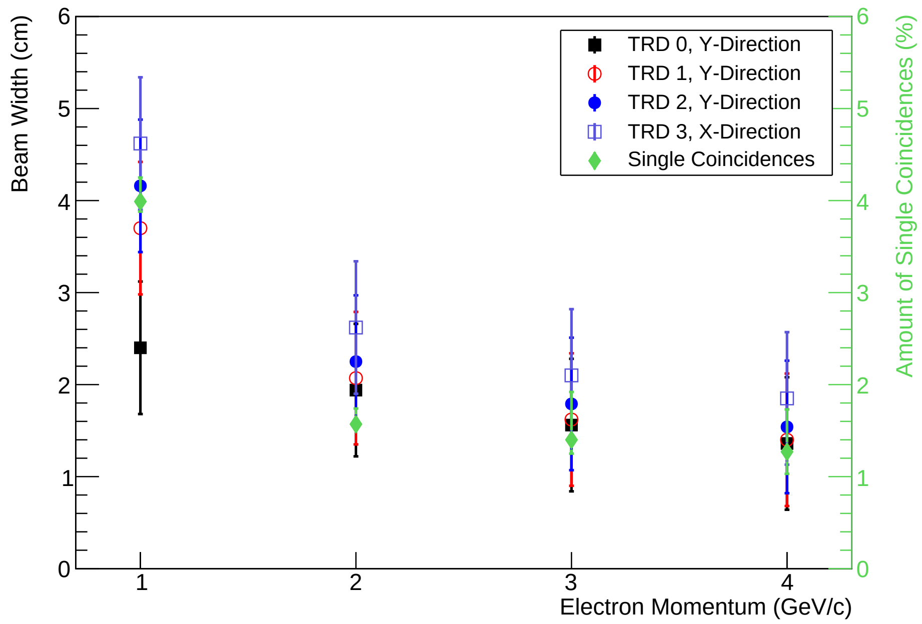

Figure 4.45.: Beam width plotted against the electron momentum (same as Figure 4.12) on the left Y-axis, while the right Y-axis and the green data points signify the amount of single coincidences found in data at each momentum.

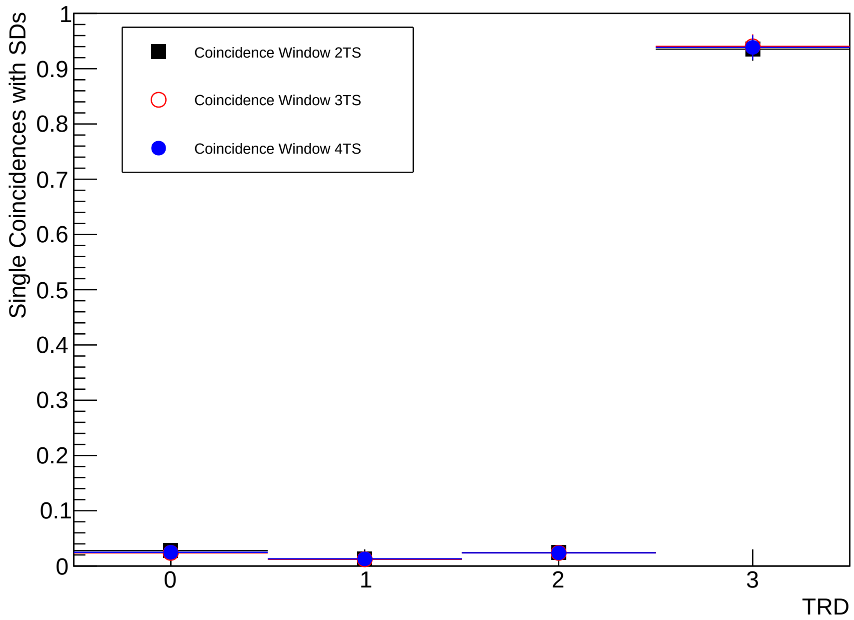

Figure 4.46.: Normalized distributions of coincidences of the SDs and only one TRD for different coincidence windows: The data was taken from 3 consecutive TSA files of run 87 at 1 GeV/c.

The contrast between the results for the first three TRDs and TRD 3, indicates that this could be caused by the difference in the active areas. Furthermore, a correlation between the amount of single coincidences and the beam width was found, which can be seen in Figure 4.45. Here, the beam width calculated in Section 4.1.3, as well as the amount of registered single coincidences was plotted against the beam momentum.

At 1 GeV/c, at which the amount of single coincidences is the largest, the distribution of these single coincidences is also shifted more clearly towards TRD 3, which is evident when comparing the distribution for 4 GeV/c (Figure 4.44) and 1 GeV/c (Figure 4.46). Due to these two observations, the different overlap of active areas is likely to be the cause of the overly large amount of detected single coincidences, which is in accordance with the calculated fractions of the beam not hitting the active area in Section 4.1.3, considering the uncertainties. The calculated fractions were just first approximations and precise results can only be achieved with clusterization. Furthermore, the calculations could only be done in one direction per detector.

As a result of the different overlaps of active areas, the assumption of each detector having the same detection efficiency for electrons passing through both SDs is not true, with the difference between the efficiencies increasing for a wider beam. This limits the accuracy of the efficiency determination of this method.

4.2.2. Effects of Data Loss in Channel Switch

Under the assumption that every generated hit message is successfully transmitted, stored and finally reconstructed by the analysis, there should not be any difference in the results of the correlation method described in Section 4.2.1, if all triggertypes or only triggertypes 1 and 3 are used. Hit messages with triggertype 2 are only generated simultaneously with at least one hit message with triggertype 1 or 3. Due to the known loss in the channel switch (see Section 3.3.4), it is possible that triggertype 2 messages occur isolated, if the hit message with triggertype 1 or 3 from their neighboring pad was lost. Hence, including also triggertype 2 should stablize the analysis against the loss effects. To check also the rate dependence of the loss, this was evaluated by calculating the individual efficiencies for each TRD, by dividing the number of "detected" electrons per TRD with the number of coincidences on the SDs. This was done for a run at $4\,\mathrm{GeV}/c$ to minimize effects caused by different detector acceptancies. In Figure 4.47, the efficiencies can be seen, resulting from including all triggertypes or only the triggertypes 1 and 3. The data points signify values with a coincidence window of $\pm 3\,\mathrm{TS}$, while the results for $\pm 2\,\mathrm{TS}$ and $\pm 4\,\mathrm{TS}$ were used as error values. Generally, the increase of efficiency resulting from correlating also triggertype 2 hit messages confirms the presence of data loss. Furthermore, the TRDs 0 and 3 show the largest increase, indicating the largest amount of data loss on the SPADICs of these two detectors. As pointed out in Section 4.1.7, these were also the two detectors with the highest load, which is in accordance with the expected load dependence of the data loss (see Section 3.3.4).

4.2.3. Lower Efficiency Limits

By defining an electron as "detected" if all four TRDs, or alternatively at least 3 TRDs have registered a hit in the coincidence window, efficiencies can be determined by simply dividing the number of detected electrons by the number of coincidences in the SD. Due to the different detector overlaps and load dependent loss of hit messages in by the channel switch, the resulting values can only be seen as lower limits, with the actual detection efficiency being equal or above. The calculated values are noted in Table 4.5.

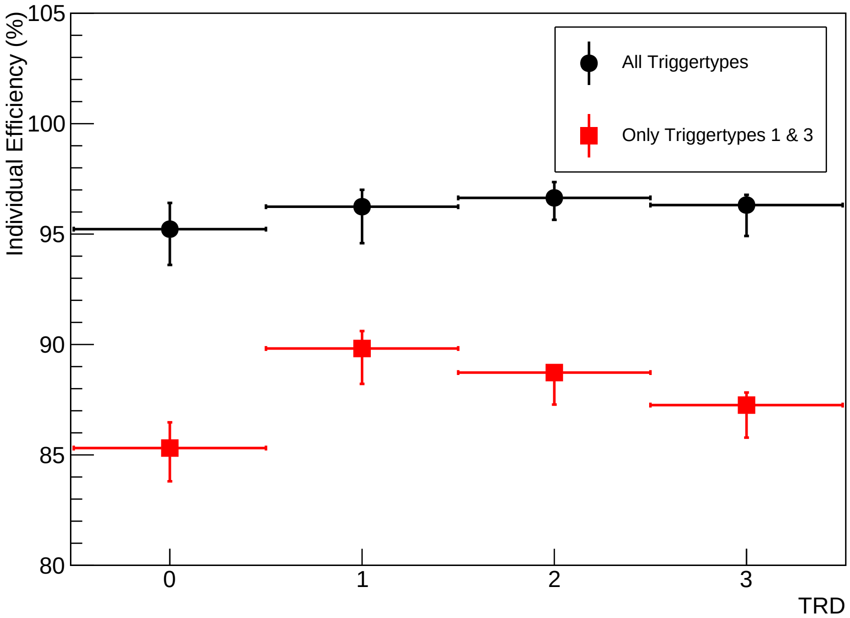

Figure 4.47.: Individual efficiencies calculated using all triggertypes (black) and only triggertypes 1 and 3 (red) at a coincidence window of ± 3 TS: The data was taken from one TSA file at $4\,\mathrm{GeV}/c$

Table 4.5.: Calculated efficiencies by diving the number of detected electron by the number of coincidences in the SD: Due to factors decreasing the calculated value, these can only be seen as lower limits of the actual efficiency.

Momentum (GeV/c)	Coinc. Window (TS)	All 4 TRDs	At least 3 TRDs
1	± 2	84.009 %	92.406 %
	± 3	85.636 %	92.900 %
	± 4	86.165 %	93.085 %
2	± 2	82.575 %	94.955 %
	± 3	84.401 %	95.524 %
	± 4	85.219 %	95.760 %
3	± 2	80.318 %	93.720 %
	± 3	82.575 %	94.992 %
	± 4	83.608 %	95.381 %
4	± 2	89.209 %	94.995 %
	± 3	91.292 %	96.558 %
	± 4	92.904 %	97.274 %

5. Conclusion and Outlook

In this thesis, data from a test beam campaign with, for the CBM-TRD, unprecedented system size and complexity have been evaluated under various aspects. Apart from some brief analyzes, this thesis documents the first in-depth examination of the data recorded at DESY, while the 2017 test beam was also the first one featuring 7 individual detectors of which the data of 6 has been successfully correlated in the course of this thesis. Though various issues in the readout system were uncovered, the general functionality of the detector setup with a high electron detection efficiency could be shown.

After confirming the correlation of the data from the detectors on a larger timescale in Section 4.1.1, also the small measured time differences between hits on the individual detectors have been thoroughly investigated (Section 4.1.2). It was known before that the method for the synchronization between the AFCKs was not working perfectly at the time of measurement. This issue has been fixed shortly after, but its effects on the data from this test beam had not been quantified yet. Hence, the results from Section 4.1.2.1 are fundamental for any analyis correlating hits from different detectors in the DESY 2017 data. Furthermore, the observation of varying time differences between the same detectors in the same measurement was made in Section 4.1.2.2 and subsequently explained by triggering of different phases of the analog signal. This can result from a different baseline position, a different signal amplitude and a different phase position with respect to the sampling of the ADC.

In Section 4.1.3, first results by [Fid] concerning the beam width have been reproduced, and then extended to all four beam momenta. A correlation of beam width and momentum, comparable to the one shown in [ACE+05] has been found. Though calculations of actual physical beam widths would require a more sophisticated analysis which includes clusterization, it could be confirmed that, depending on the beam momentum and detector layer, between 85 % and 99.9 % of the beam along the axis of high position resolution were located on the active detector area.

The investigation of the signal shapes and the maximum ADC spectra in Section 4.1.4 showed that, while a great number of incoming hits is actual signal, there is also a considerable amount of additional hit messages, due to retriggering on falling tails of previous signals. Hit messages caused by this effect were then separated and a first cut was introduced, which performed well under brief examinations and was reused later in comparisons regarding hit message frequencies (see Section 4.1.7). Though the observed suppression of certain ADC values on certain channels and its possible effects on charge reconstruction should be

further investigated, the general functionality of the charge reconstruction from data taken with the same electronics has already been shown by [Bec18] with an with an ^{55}Fe source. Furthermore, first electron spectra reconstructed from the DESY data by F. Roether in [Kae18] look promising.
Subsequently, in Section 4.1.5, the bug resulting in the transmission of one presample less than expected, occuring on several SPADICs, was uncovered, which had not be observed and described before. The possibility of this being a reconstruction artifact has been excluded as far as possible and communication with SPADIC development was opened. Since the SPADIC 2.2 will have an exact frequency locking, future comparison measurements will show if the suggested explanation is true. As long as the cause for this issue is not found, a check for the number of presamples as done in this thesis should be conducted before taking data in future measurements, as a missing presample impedes the accuracy of the baseline determination.
In Section 4.1.6, an in-depth examination of the SPADIC's baseline has been carried out. Up to this point, only baseline corrections by taking the first sample of each signal, or running averages over the first sample of each signal have been conducted. Both methods have been found as not suitable for this thesis, as retriggering on falling tails causes a shift on the running averages, and the large baseline width indicates high frequency oscillations, thus limiting the accuracy of individual baseline corrections for each signal.
Keeping the issue of the missing presample in mind, the proposed method using a Gaussian fit over the first sample has been presented with two workarounds for data with one presample less, which also served as reference values. After confirming the general functionality of the proposed three methods, the baseline behaviour has been investigated for different timescales in Section 4.1.6.2. Since slow baseline shifts were observed to be small, the timescale was subsequently decreased. Also with one data point per 2 s, no different behaviour has been observed. As the baseline width has been found to still be larger than expected, the higher frequency changes should be considered. Because no data with external triggering has been taken at DESY, the available data lacks the statistics for a meaningful analyis. A new master thesis with a dedicated test setup for baseline measurements is in preparation by [Mor], based on the obervations made in this thesis. While the width of the baseline needs to be reduced substantially to achieve the design value, it has to be noted that a good detector energy resolution was measured with a ^{55}Fe source by [Bec18].
As a last part of the QA, hit message frequencies and especially their differences among the detectors were investigated. The main increase of the hit message frequency on TRD 0 could be explained by a larger amount of retriggering on falling tails due to a wider baseline. After applying the cut for these types of signals introduced in Section 4.1.4, the TRDs 0-2 behaved similarly. The remaining small increase of hit message frequency on TRD 3 was explained by the beam position on the pad border, as has been shown in Section 4.1.3.
In the final part of the thesis (Section 4.2), the electron detection efficiency has

been evaluated by looking at the distribution of how many TRDs registered a hit in a short timewindow around a coincidence in the SDs. While the general shape of the data was comparable to the expected binomial distribution, a large number of entries in the smaller bins has been observed. After excluding random coincidences as a cause, the entries in bin 1 were suspected to be a result of the different orientation of the TRDs, since most single coincidences (i.e. coincidence of both SDs and only one TRD) occur on TRD 3. A clear correlation between the beam momentum (and thus, width) and the amount of single coincidences has been found. Hence, the hypothesis was formed that an electron could bypass the active areas of the first three TRDs and thus, only be detected by TRD 3 and the SDs. This is in accordance with the results of Section 4.1.3, considering the large uncertainties of the amount of beam hitting the active detector area. To verify that the cause of the lower efficiency at $1\,\mathrm{GeV}/c$ was indeed the wider beam, the measurements could be repeated with either a larger active area on the TRDs or smaller trigger detectors.
In general, the resulting efficiencies confirm the overall detector and readout functionality. Even though the beforementioned issues should be resolved as much as possible in the future, electron detection is already possible with a high efficiency at the present state.

A. Appendix

A.1. Tables

Note: To improve readability, the tables containing the fit results for the hitmaps (see Section 4.1.3) are positioned on the same pages as the plots. Hence, they can be found in Section A.2

Table A.1.: Number of presamples in hit messages of the SPADICs connected to the different detectors in all viewed runs.

	AFCK0		AFCK 1	AFCK 2	AFCK 3	AFCK 1	AFCK 3
Run	TRD0	^{55}Fe Source	TRD 1	TRD 2	TRD 3	MWPC	SD 0 & 1
72	OFF	2	OFF	OFF	OFF	OFF	OFF
73	2	2	2	2	2	1	2
74	2	2	2	2	2	1	2
75	2	2	2	2	2	1	2
RUN 76 MISSING							
77	2	2	2	2	2	1	2
RUN 78 MISSING DUE TO FLESNET ERROR							
79	2	2	2	2	2	1	2
80	2	2	2	2	2	1	2
81	2	2	2	2	2	1	2
82	2	2	2	2	2	1	2
83	2	2	2	2	2	1	2
84	2	2	2	2	2	1	2
85	2	2	2	2	2	1	2
86	2	2	2	2	2	1	2
87	2	2	2	2	2	1	2
RESYNC							
88	1	1	2	2	2	2	2
89	1	1	2	2	2	2	2
91	1	1	2	2	2	2	2
RUNS 92-94 MISSING							
95	1	1	2	2	2	2	2
RUN 96 MISSING							
97	1	1	2	2	2	2	
RUNS 98/99 MISSING DUE TO FLESNET ERROR							

100	1	1	2	2	2	2	2
101	1	1	2	2	2	2	2
102	1	1	2	2	2	2	2
103	1	1	2	2	2	2	2
104	1	1	2	2	2	2	2
105	1	1	2	2	2	2	2
106	1	1	2	2	2	2	2
107	1	1	2	2	2	2	2
RUNS 108/109 MISSING							
110	2	2	2	2	2	2	2
111	2	2	2	2	2	2	2
112	2	2	2	2	Corrupted	2	2
113	1	OFF	2	2	2	2	2
114	1	OFF	2	2	2	2	2
115	1	2	2	2	2	2	2
116	1	2	2	2	2	2	2
117	1	2	2	2	2	2	2
118	1	1	2	2	2	2	2
119	1	1	2	2	2	2	2
120	1	1	2	2	2	2	2
121	1	1	2	2	2	2	2
RESYNC							
122	1	1	2	2	1	2	2
123	1	1	2	2	1	2	2
124	1	1	2	2	1	2	2
125	1	1	2	2	1	2	2
126	1	1	2	2	1	2	2

A.2. Figures

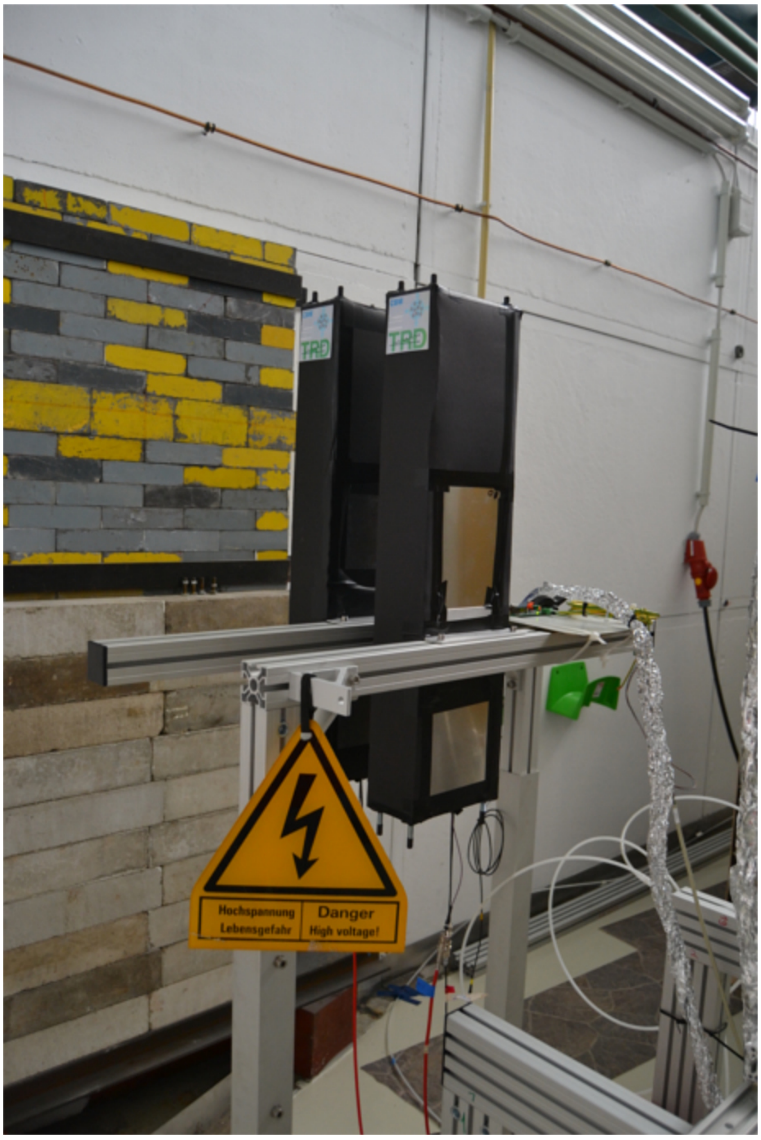

Figure A.1.: Close up photo of the scintillation detectors (Photo: Florian Roether)

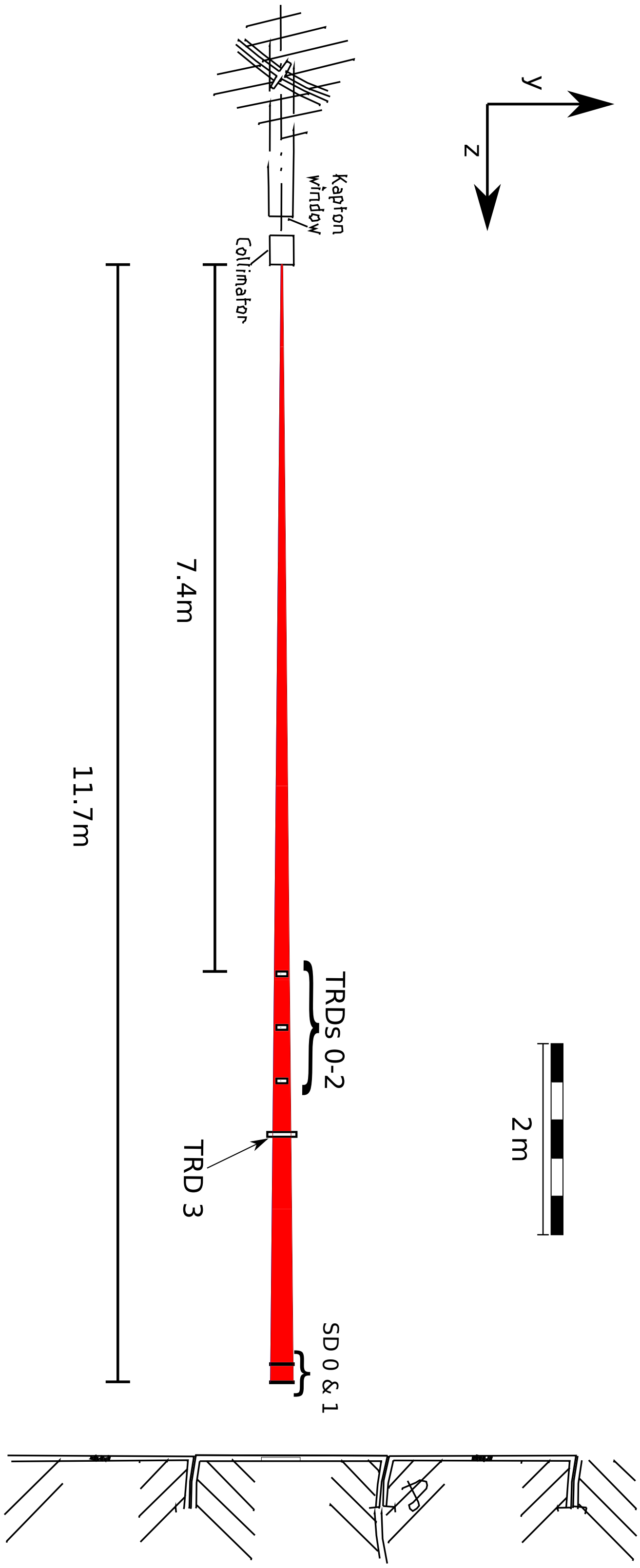

Figure A.2.: To scale schematic drawing of the active detector areas in the YZ-plane of the test beam area: The red area signifies the widest possible electron beam still hitting the SDs.

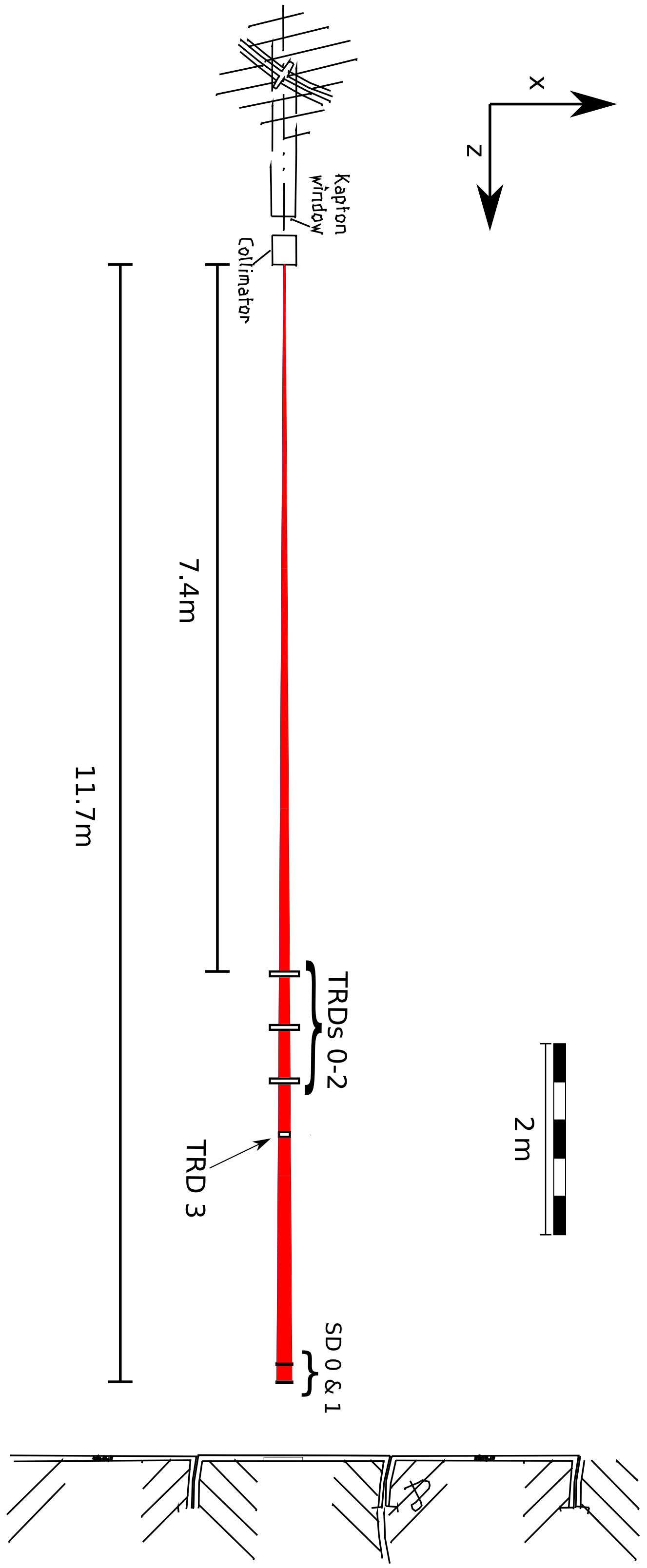

Figure A.3.: To scale schematic drawing of the active detector areas in the XZ-plane of the test beam area: The red area signifies the widest possible electron beam still hitting the SDs.

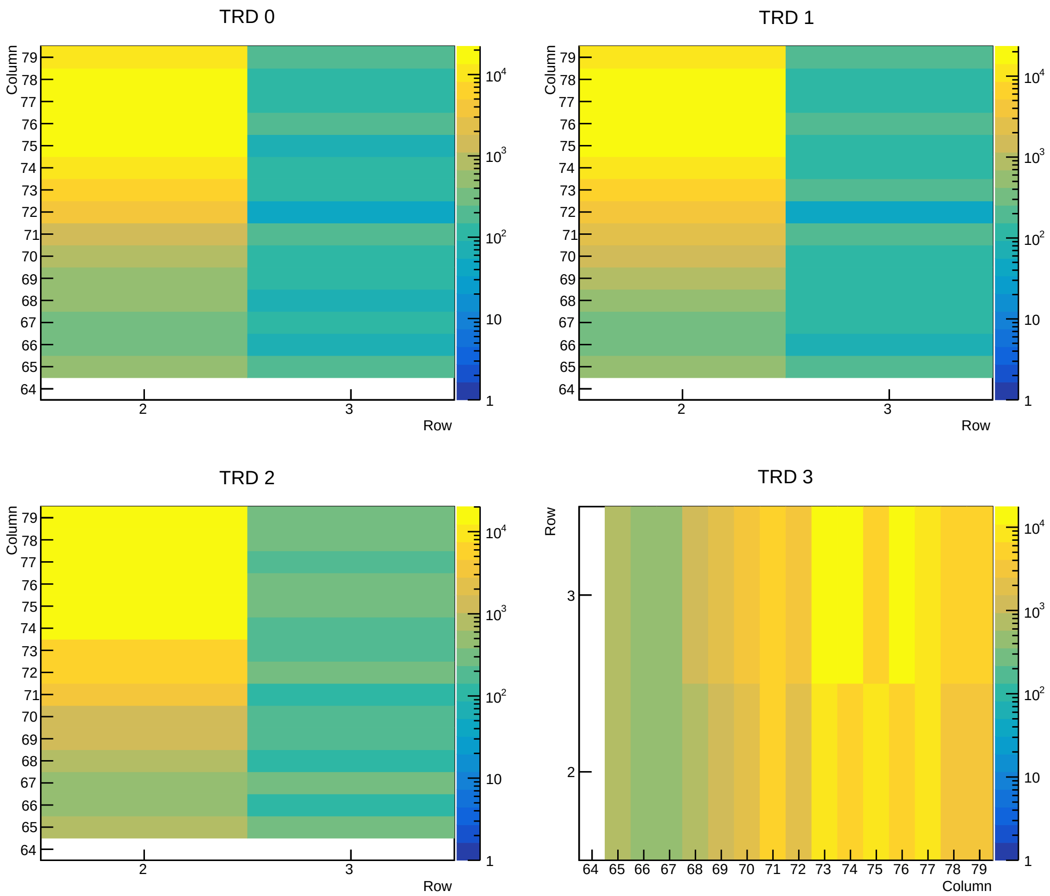

Figure A.4.: Hitmaps for each TRD: The total amount of hit messages with triggertype 1 registered on individual pad is plotted. The data was taken from one TSA file at a momentum of $1\,\mathrm{GeV}/c$.

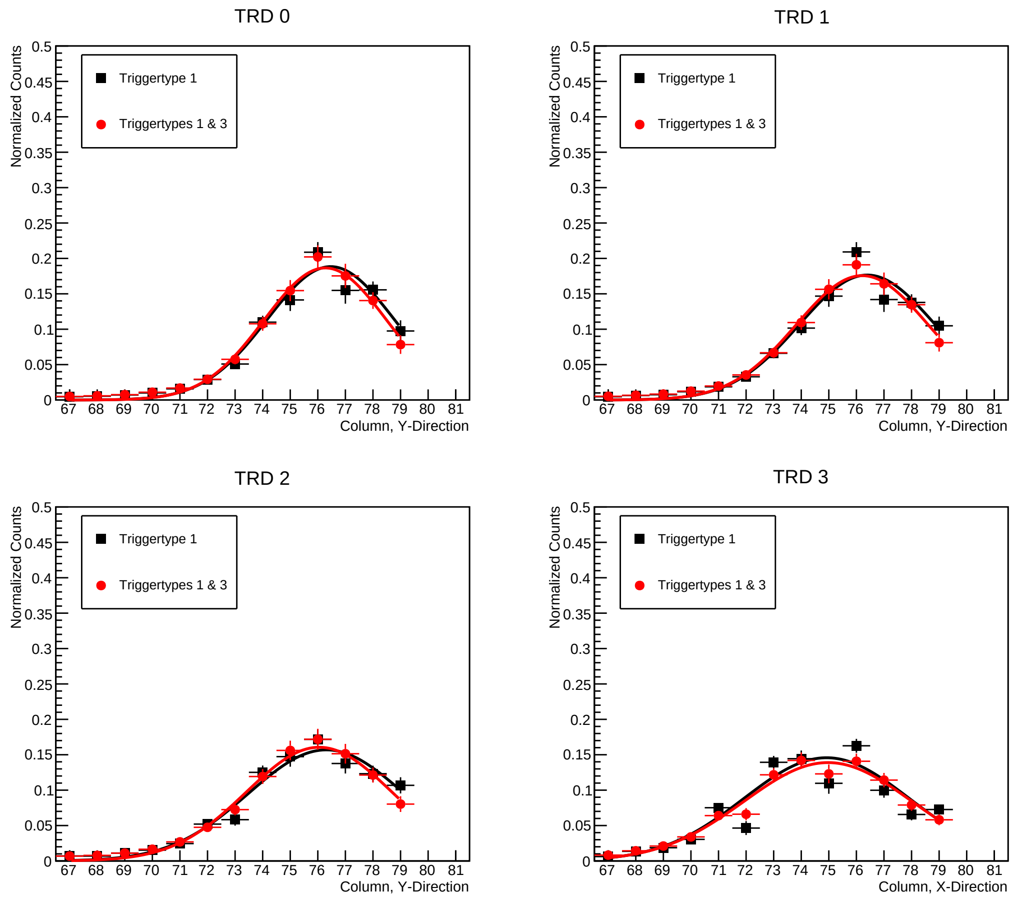

Figure A.5.: Projections of the hitmaps on the “column-axis”, each fitted with a Gaussian function: The TRDs 0-2 give the beam position in Y-direction and TRD 3 in X-direction, due to its rotation by 90°. The data was taken from one TSA file at a momentum of 1 GeV/c.

Table A.2.: Fit parameters of the Gaussian fits for the projections of the hitmaps at 1 GeV/c: The data and the Gaussian functions are plotted in Figure 4.11.

TRD	Triggertypes	Constant	Mean (Column)	Sigma (Column)	χ^2_{red}
0	1	0.19 ± 0.01	76.47 ± 0.13	2.295 ± 0.121	1.36
	1 & 3	0.19 ± 0.01	76.27 ± 0.11	2.218 ± 0.111	0.97
1	1	0.18 ± 0.13	76.39 ± 0.14	2.452 ± 0.131	1.52
	1 & 3	0.18 ± 0.01	76.21 ± 0.12	2.387 ± 0.121	0.84
2	1	0.16 ± 0.01	76.31 ± 0.17	2.830 ± 0.156	1.55
	1 & 3	0.16 ± 0.01	76.05 ± 0.13	2.639 ± 0.136	0.85
3	1	0.14 ± 0.01	74.97 ± 0.11	2.995 ± 0.115	5.84
	1 & 3	0.14 ± 0.01	74.97 ± 0.12	3.041 ± 0.126	1.19

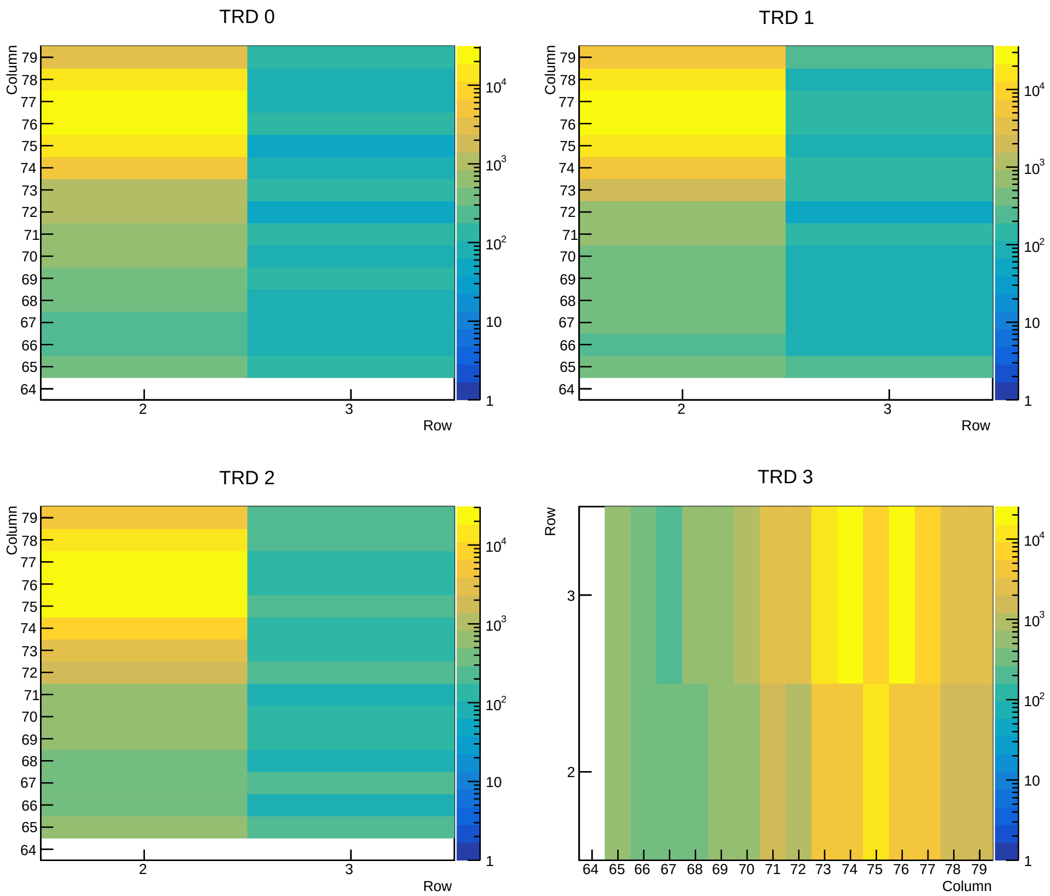

Figure A.6.: Hitmaps for each TRD: The total amount of hit messages with triggertype 1 registered on individual pad is plotted. The data was taken from one TSA file at a momentum of 2 GeV/c.

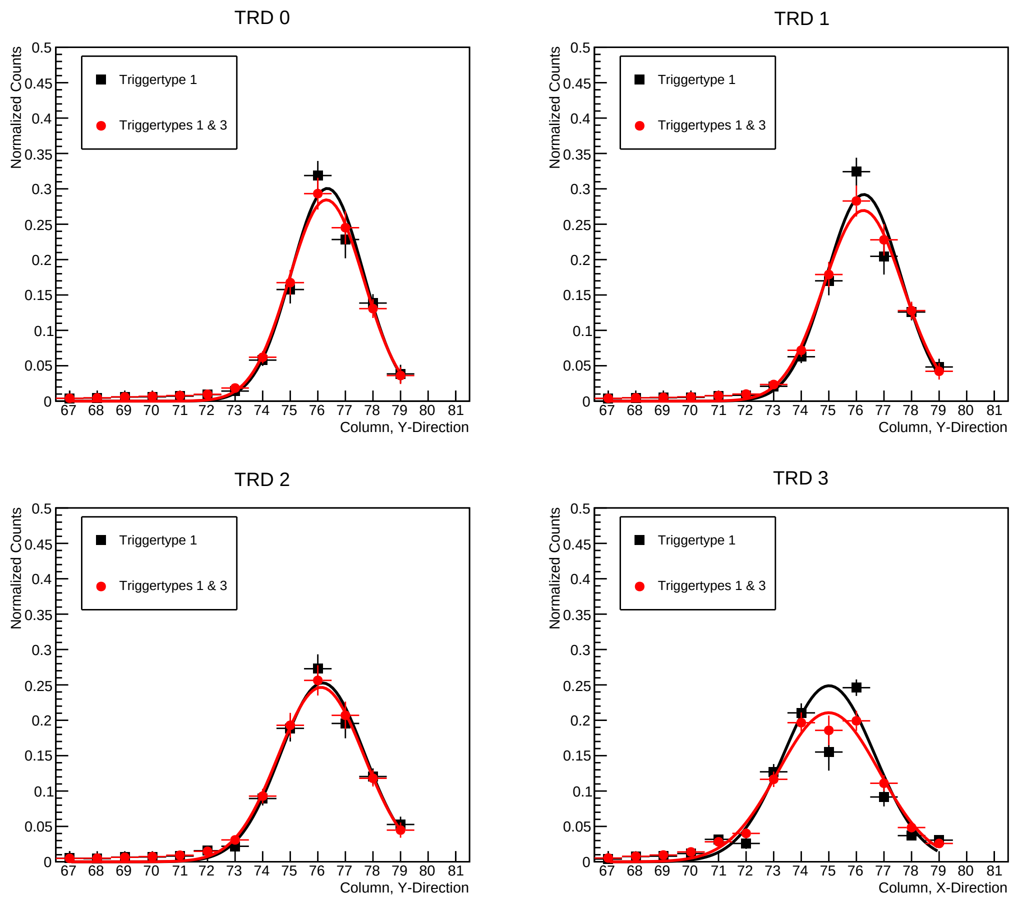

Figure A.7.: Projections of the hitmaps on the "column-axis", each fitted with a Gaussian function: The TRDs 0-2 give the beam position in Y-direction and TRD 3 in X-direction, due to its rotation by 90°. The data was taken from one TSA file at a momentum of 2 GeV/c.

Table A.3.: Fit parameters of the Gaussian fits for the projections of the hitmaps at 2 GeV/c: The data and the Gaussian functions are plotted in Figure A.7.

TRD	Triggertypes	Constant	Mean (Column)	Sigma (Column)	χ^2_{red}
0	1	0.30 ± 0.02	76.35 ± 0.06	1.306 ± 0.051	1.34
	1 & 3	0.28 ± 0.02	76.31 ± 0.06	1.351 ± 0.056	1.11
1	1	0.29 ± 0.02	76.27 ± 0.06	1.346 ± 0.053	1.73
	1 & 3	0.27 ± 0.02	76.25 ± 0.06	1.433 ± 0.059	0.93
2	1	0.25 ± 0.02	76.17 ± 0.07	1.518 ± 0.063	1.47
	1 & 3	0.25 ± 0.01	76.12 ± 0.07	1.560 ± 0.064	1.07
3	1	0.25 ± 0.01	75.01 ± 0.07	1.662 ± 0.057	6.82
	1 & 3	0.21 ± 0.01	75.00 ± 0.07	1.834 ± 0.065	2.22

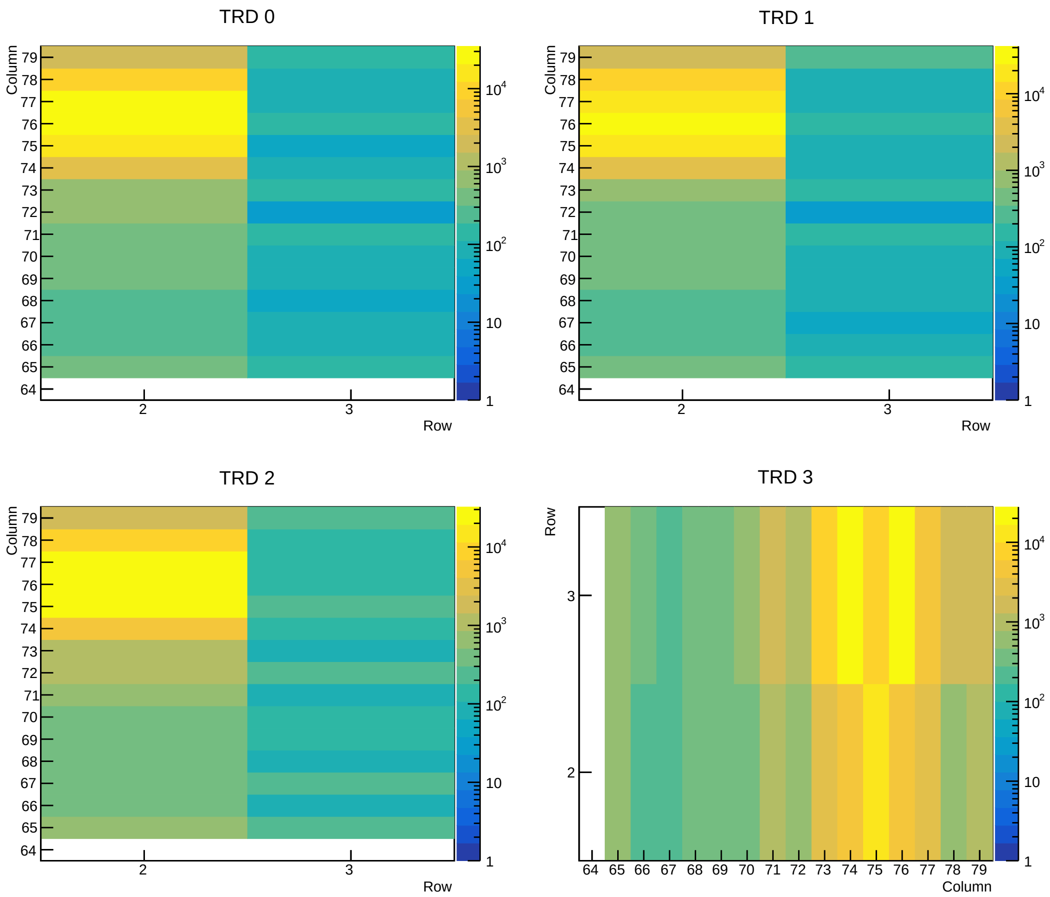

Figure A.8.: Hitmaps for each TRD: The total amount of hit messages with triggertype 1 registered on individual pad is plotted. The data was taken from one TSA file at a momentum of 3 GeV/c.

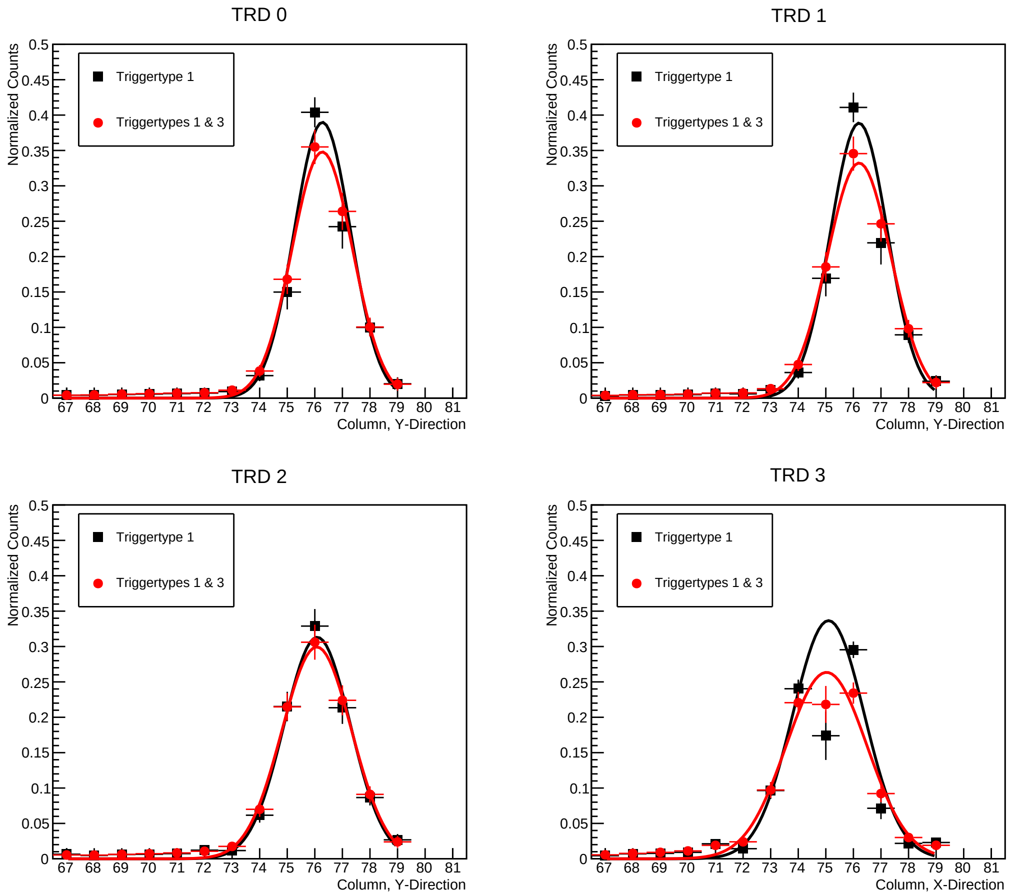

Figure A.9.: Projections of the hitmaps on the "column-axis", each fitted with a Gaussian function: The TRDs 0-2 give the beam position in Y-direction and TRD 3 in X-direction, due to its rotation by 90°. The data was taken from one TSA file at a momentum of 3 GeV/c.

Table A.4.: Fit parameters of the Gaussian fits for the projections of the hitmaps at 3 GeV/c: The data and the Gaussian functions are plotted in Figure A.9.

TRD	Triggertypes	Constant	Mean (Column)	Sigma (Column)	χ^2_{red}
0	1	0.39 ± 0.02	76.27 ± 0.05	1.024 ± 0.038	1.69
	1 & 3	0.35 ± 0.02	76.27 ± 0.05	1.098 ± 0.044	1.14
1	1	0.39 ± 0.02	76.20 ± 0.05	1.031 ± 0.038	1.95
	1 & 3	0.33 ± 0.02	76.21 ± 0.05	1.151 ± 0.046	1.07
2	1	0.31 ± 0.02	76.09 ± 0.05	1.201 ± 0.047	1.56
	1 & 3	0.30 ± 0.02	76.07 ± 0.06	1.262 ± 0.049	1.25
3	1	0.34 ± 0.01	75.01 ± 0.05	1.298 ± 0.043	7.31
	1 & 3	0.26 ± 0.01	75.03 ± 0.06	1.467 ± 0.052	3.10

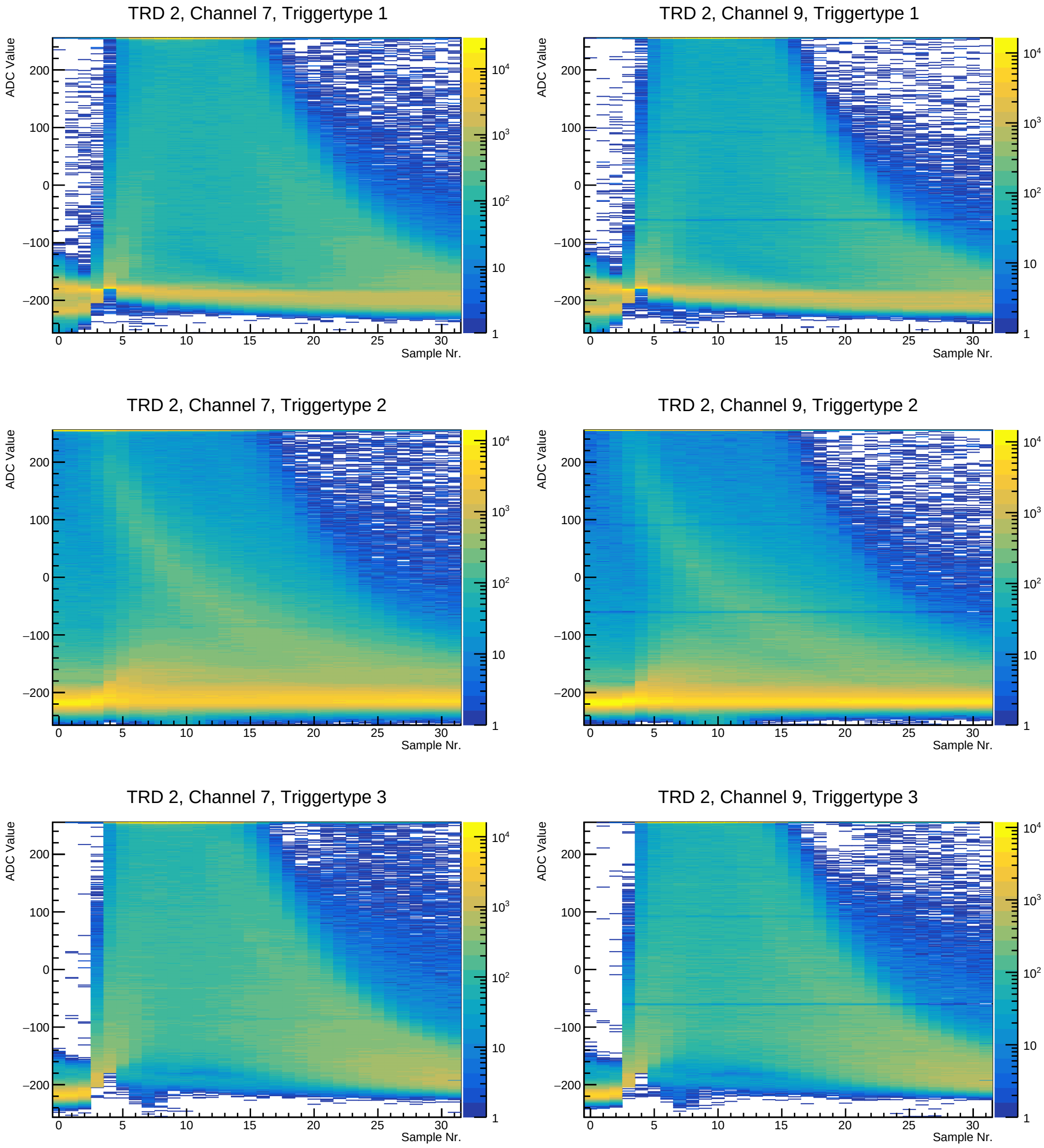

Figure A.10.: Overlays of signal shapes on the two most active channels of TRD 2 for different triggertypes. The data is taken from one TSA file of run 97.

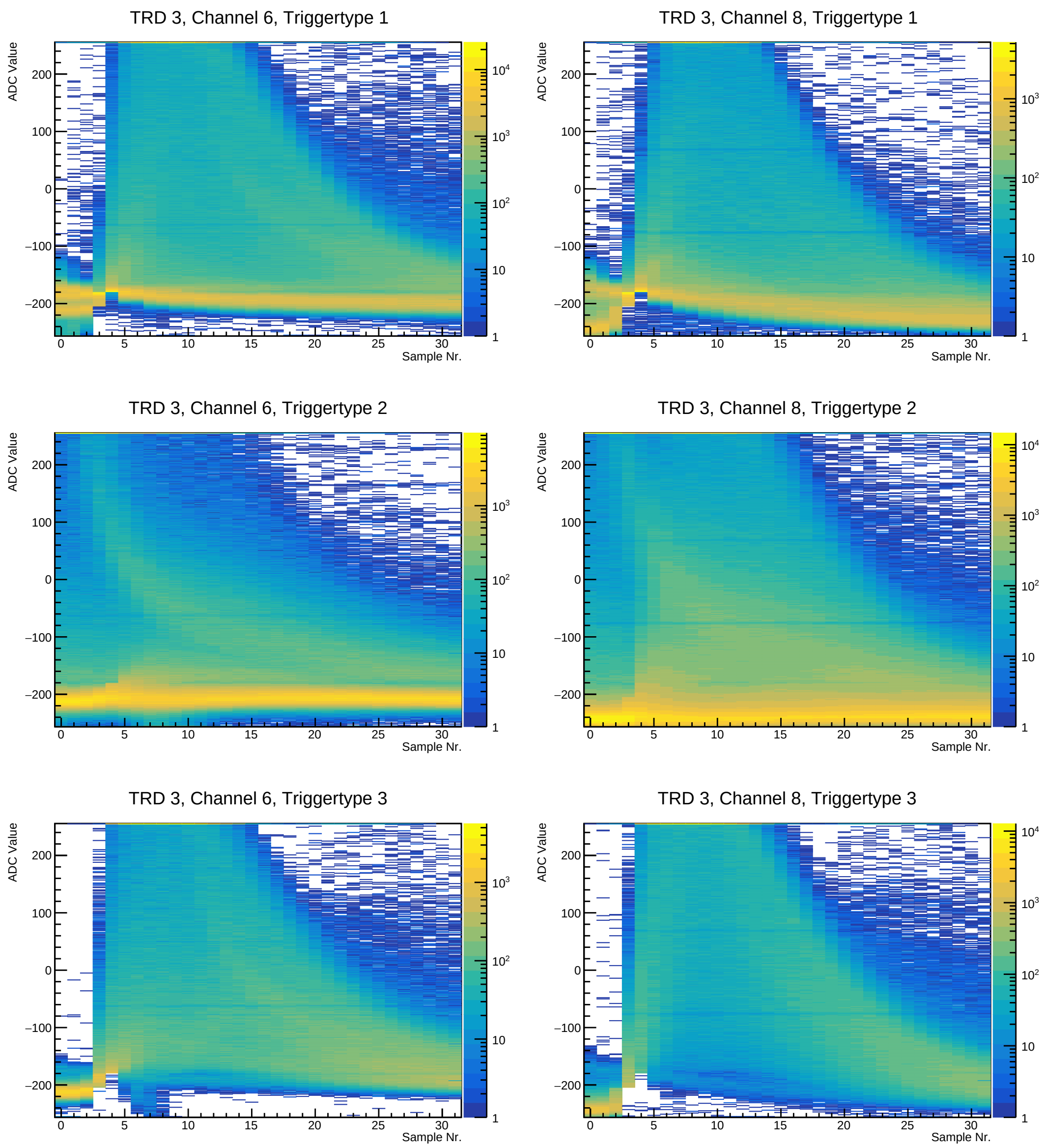

Figure A.11.: Overlays of signal shapes on the two most active channels of TRD 3 for different triggertypes. The data is taken from one TSA file of run 97.

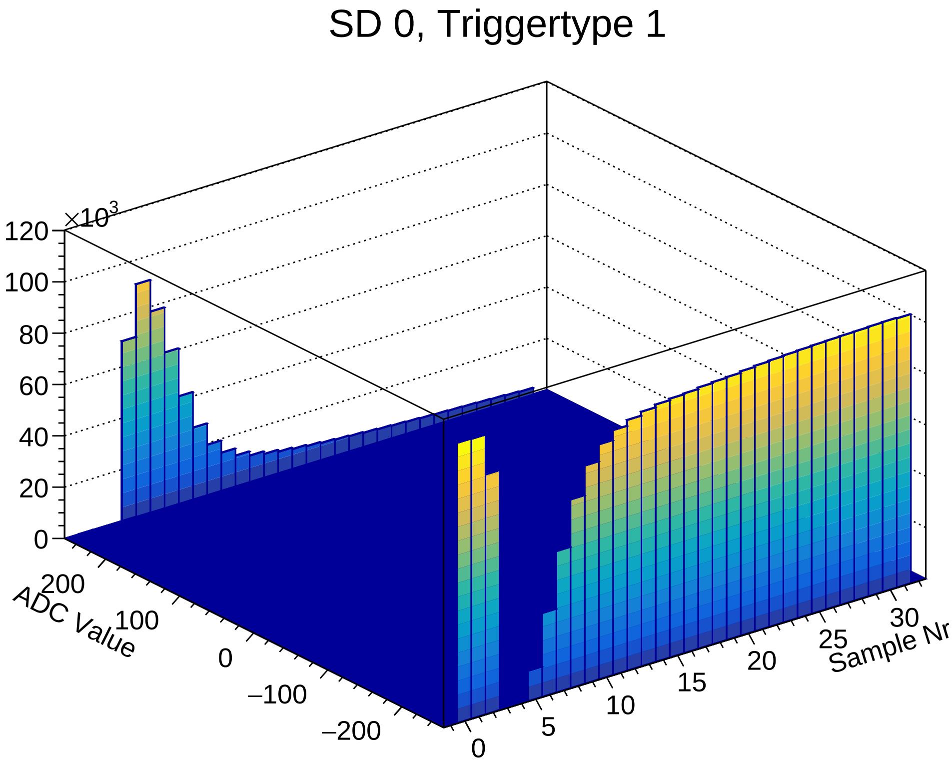

Figure A.12.: Overlays of signal shapes of SD 0 on a non logarithmic z-scale. The data is taken from one TSA file of run 97.

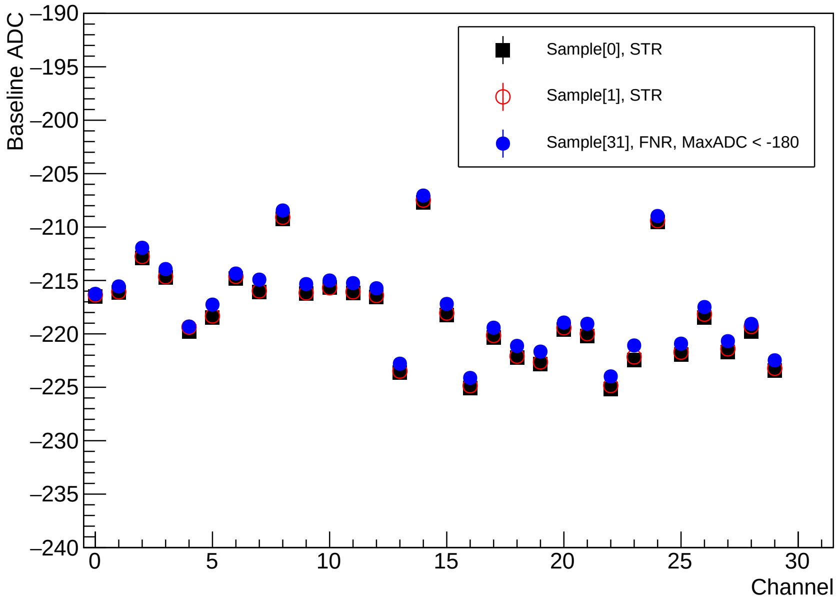

Figure A.13.: Baseline positions on SPADIC 6 determined by Gaussian fits for the sample[0], sample[1] and sample[31] methods.

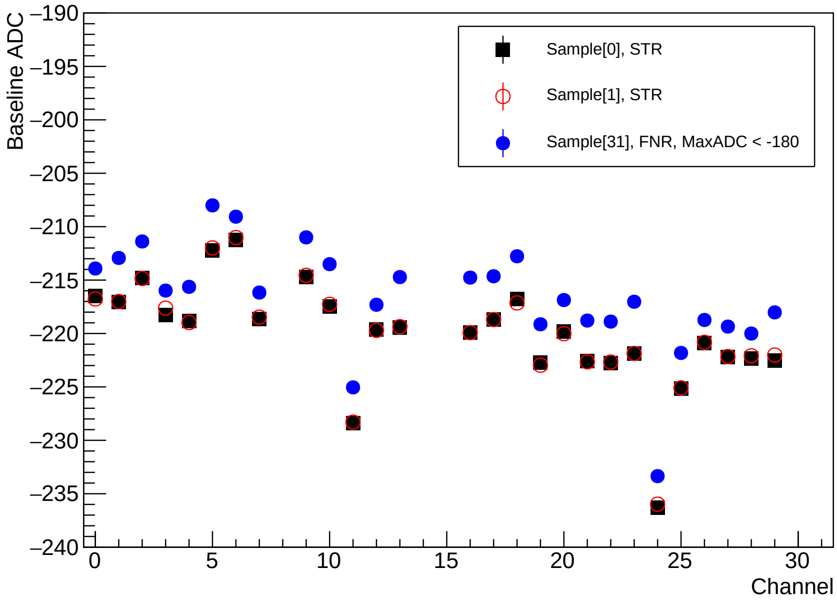

Figure A.14.: Baseline positions on SPADIC 9 determined by Gaussian fits for the sample[0], sample[1] and sample[31] methods.

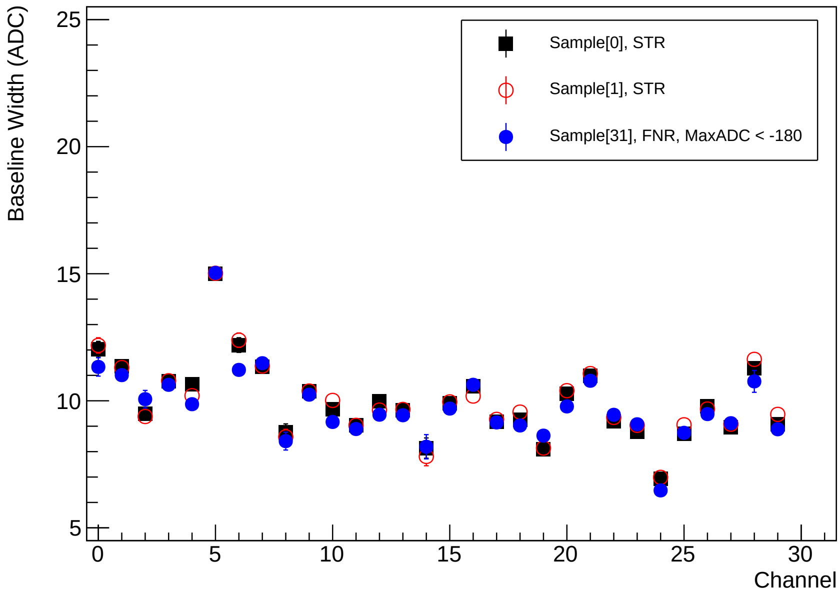

Figure A.15.: Baseline widths on SPADIC 6 determined by Gaussian fits for the sample[0], sample[1] and sample[31] methods.

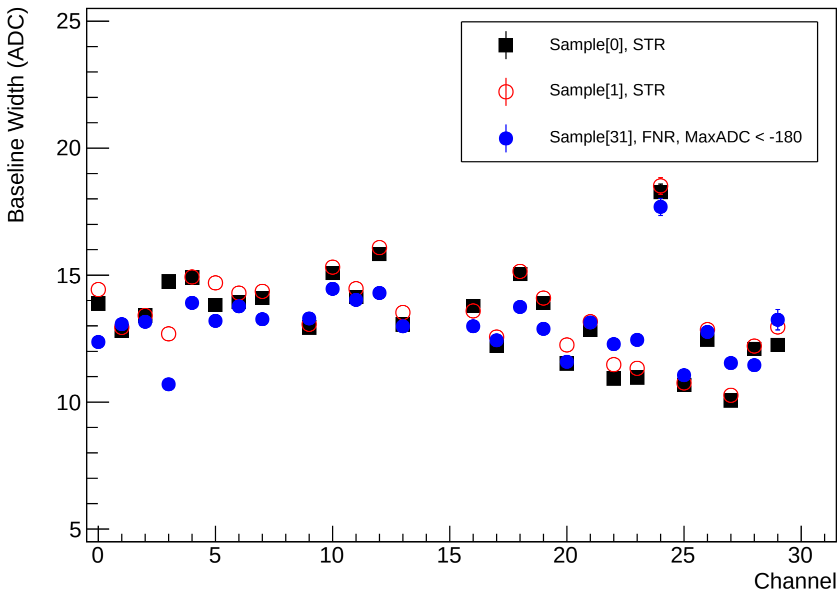

Figure A.16.: Baseline widths on SPADIC 9 determined by Gaussian fits for the sample[0], sample[1] and sample[31] methods.

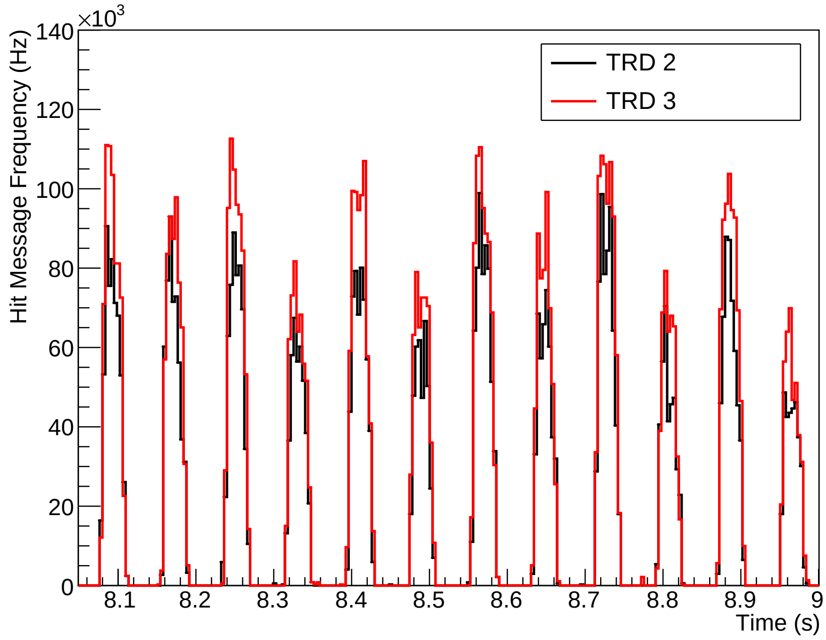

Figure A.17.: Hit message frequency on TRD 2 and TRD 3 plotted against time. The data was taken from run 97 at a beam momentum of 4 GeV/c.

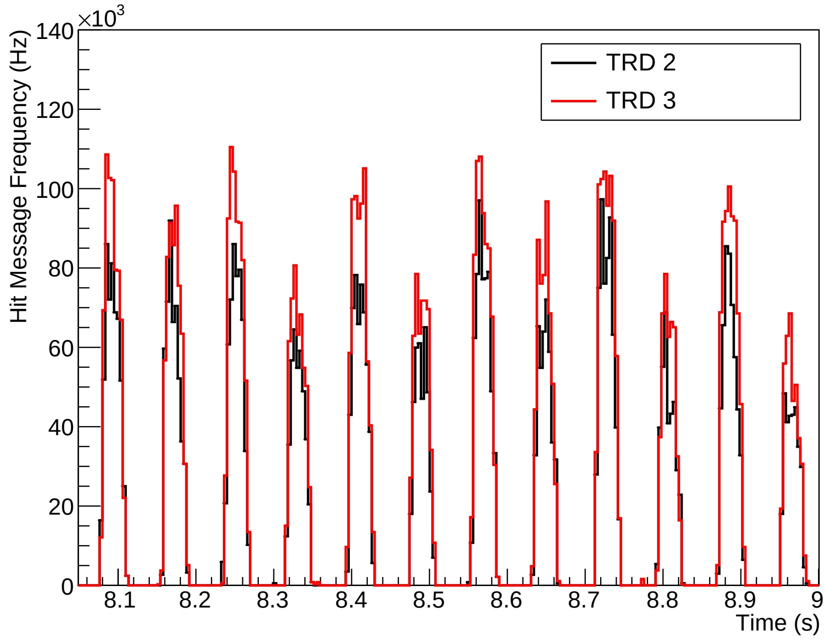

Figure A.18.: Hit message frequency on TRD 2 and TRD 3 after excluding all hits from the channels 0 and 1 plotted against time. The data was taken from run 97 at a beam momentum of 4 GeV/c.

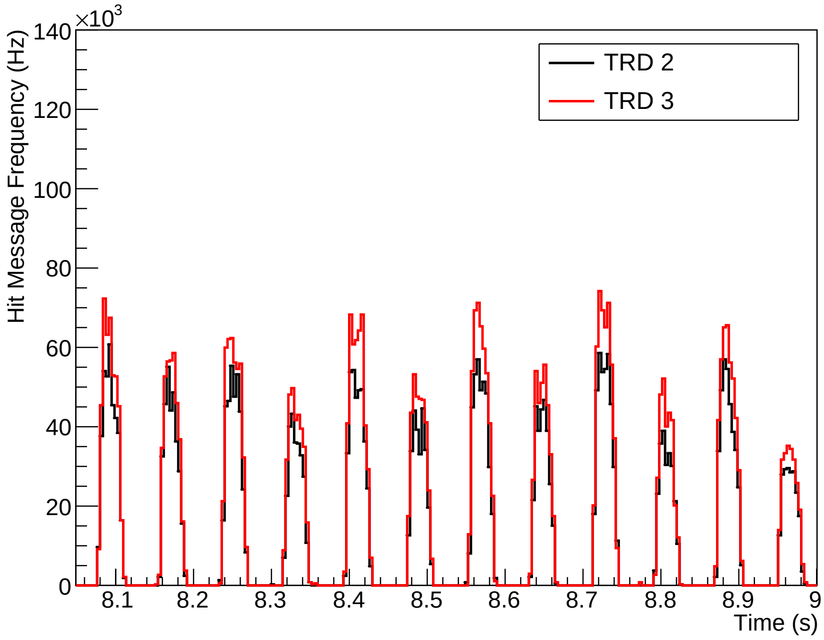

Figure A.19.: Hit message frequency on TRD 0 and TRD 1 after excluding all hits from the channels 0 and 1 and applying the cut for tail retriggering (Equation 4.9) plotted against time. The data was taken from run 97 at a beam momentum of 4 GeV/c.

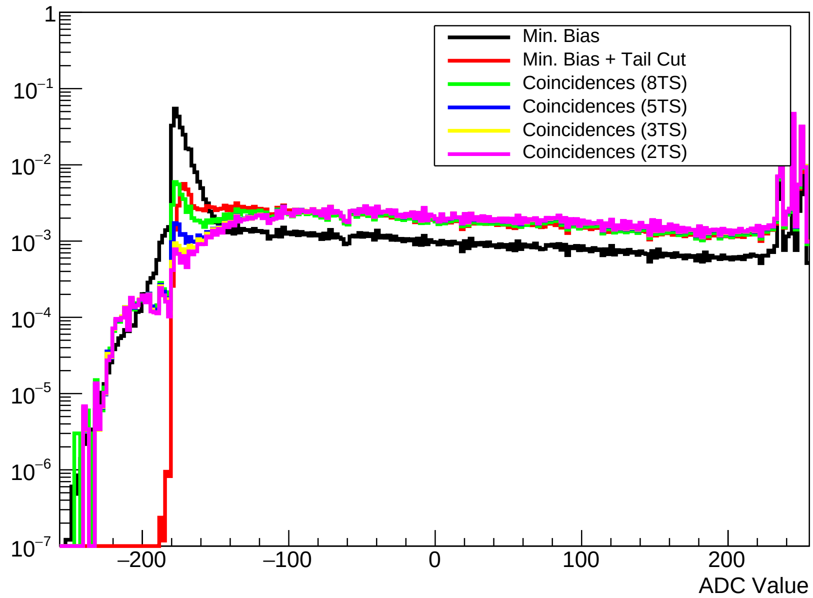

Figure A.20.: Normalized maximum ADC spectra of all self-triggered hits on TRD 0 without cut (black), all self-triggered hits after applying the cut for retriggering on falling tails (Equation 4.9) (red), and self-triggered hits in different coincidences windows (green, blue, yellow and pink). For the latter ones, no further cut was applied. The data was take from 10 consecutive TSA files from run 97 at a beam momentum of 4 GeV/c.

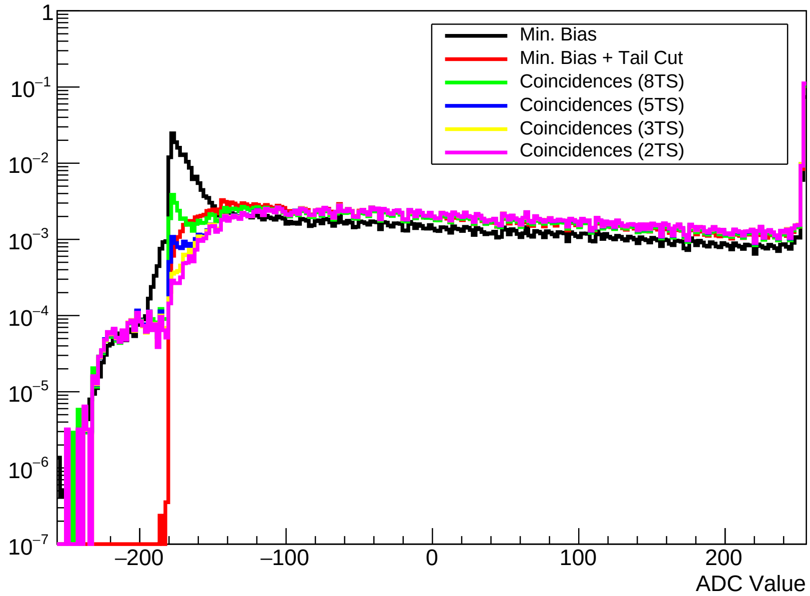

Figure A.21.: Normalized maximum ADC spectra of all self-triggered hits on TRD 1 without cut (black), all self-triggered hits after applying the cut for retriggering on falling tails (Equation 4.9) (red), and self-triggered hits in different coincidences windows (green, blue, yellow and pink). For the latter ones, no further cut was applied. The data was take from 10 consecutive TSA files from run 97 at a beam momentum of $4\,\mathrm{GeV}/c$.

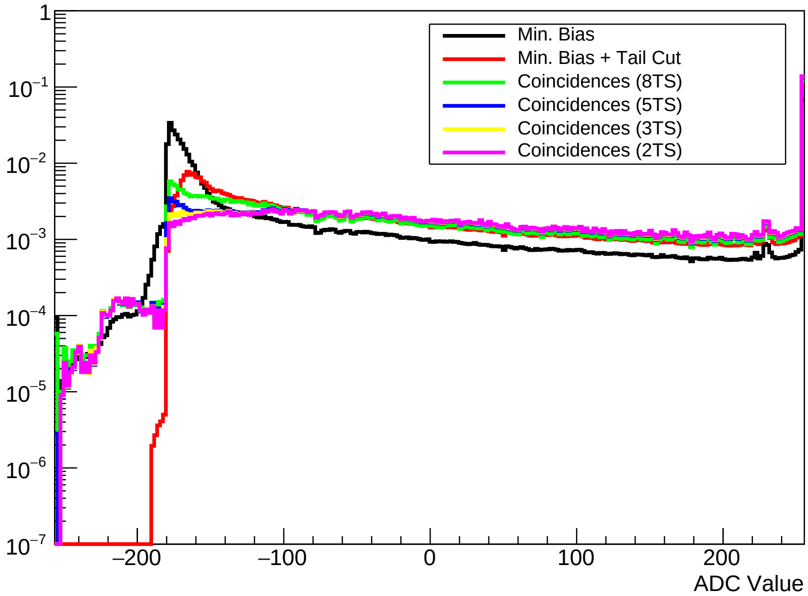

Figure A.22.: Normalized maximum ADC spectra of all self-triggered hits on TRD 3 without cut (black), all self-triggered hits after applying the cut for retriggering on falling tails (Equation 4.9) (red), and self-triggered hits in different coincidences windows (green, blue, yellow and pink). For the latter ones, no further cut was applied. The data was take from 10 consecutive TSA files from run 97 at a beam momentum of 4 GeV/c.

A.3. Conditions for Filtering Time Difference Distributions

Notation:

- $S_n(t)$: Normalized baseline corrected signal amplitude at timestamp t
- $\Delta_{i,j}$: ADC value of sample[i]−sample[j]

For $\Delta t = -1\,\mathrm{TS}$:

1. Maximum ADC $\neq 255$
2. $\Delta_{3,2} < \Delta_{5,4}$
3. $\Delta_{4,3} < \Delta_{5,4}$
4. $\Delta_{11,10} < \Delta_{3,2} < \Delta_{9,8} < \Delta_{8,7} < \Delta_{7,6}$
5. $\Delta_{7,6} < \Delta_{4,3}$

For $\Delta t = 0\,\mathrm{TS}$:

1. Maximum ADC $\neq 255$
2. $S_n(2) < 0.02$
3. $0.09 < S_n(3) < 0.2$
4. $\Delta_{3,2} < \Delta_{5,4} < \Delta_{4,3}$

For $\Delta t = 1\,\mathrm{TS}$:

1. Maximum ADC $\neq 255$
2. $S_n(1) < S_n(2)$
3. $\Delta_{5,4} < \Delta_{3,2}$
4. $\Delta_{5,4} < \Delta_{4,3}$
5. $\Delta_{9,8} < \Delta_{2,1}$

Bibliography

[A^+17] T. Ablyazimov et al. Challenges in QCD matter physics –The scientific programme of the Compressed Baryonic Matter experiment at FAIR. *Eur. Phys. J.*, A53(3):60, 2017.

[ACE^+05] D Autiero, Y Caffari, Luigi Salvatore Esposito, A Marotta, J Marteau, and Pasquale Migliozzi. Characterization of the T24 electron beam line available at DESY. 01 2005.

[Arm13] Tim Armbruster. SPADIC - a Self-Triggered Detector Readout ASIC with Multi-Channel Amplification and Digitization, 2013.

[AW12] A. Andronic and J. P. Wessels. Transition radiation detectors. *Nuclear Instruments and Methods in Physics Research A*, 666:130–147, February 2012.

[Bec18] Johannes Beckhoff. Automated Test Stand Setup and Signal Reconstruction for the CBM-TRD, 2018.

[Ber14] Cyrano Bergmann. Development, Simulation and Test of Transition Radiation Detector Prototypes for the Compressed Baryonic Matter Experiment at the Facility for Antiproton and Ion Research, 2014.

[Bic] Bicron Scintillator Data Sheet. `https://www.crystals.saint-gobain.com/sites/imdf.crystals.com/files/documents/bc400-404-408-412-416-data-sheet.pdf`. Accessed: 22.2.2019.

[BRR08] Walter Blum, Luigi Rolandi, and Werner Riegler. *Particle detection with drift chambers*. Particle Acceleration and Detection. 2008.

[CBM18] The Transition Radiation Detector of the CBM Experiment at FAIR : Technical Design Report for the CBM Transition Radiation Detector (TRD). Technical Report FAIR Technical Design Report, Darmstadt, 2018.

[D^+18] R. Diener et al. The DESY II Test Beam Facility. 2018.

[Ems] David Emschermann. CBM TRD in Münster. `http://cbm.uni-muenster.de/padplane/more/2015_preview/82_2015_type8.pdf`. Accessed: 24.02.2019.

[Fid] Felix Fidorra. Master thesis, to be published.

[Ham] Hamamatsu R2154-02 Data Sheet. `https://www.hamamatsu.com/resources/pdf/etd/R2154-02_TPMH1089E.pdf`. Accessed: 22.02.2019.

[Kae18] Philipp Kaehler. Status of DESY and GIF Analysis. `https://indico.gsi.de/event/5862/session/21/contribution/34/material/slides/0.pdf`, March 2018. Cited plot provided by F. Roether. Accessed: 24.02.2019.

[Kle05] Konrad Kleinknecht. *Detektoren für Teilchenstrahlung*. 2005.

[Kri18] Michael Krieger. The State of Spadic 2.1. `https://indico.gsi.de/event/6883/session/1/contribution/12/material/slides/0.pdf`, March 2018. Accessed: 24.02.2019.

[KW16] Hermann Kolanoski and Norbert Wermes. *Teilchendetektoren*. Springer, 2016.

[Leo87] W. R. Leo. *Techniques for Nuclear and Particle Physics Experiments: A How to Approach*. 1987.

[Lov28] Howard Phillips Lovecraft. The Call of Cthulhu. *Weird Tales*, 11:159–178, February 1928.

[MA16] Adrian Meyer-Ahrens. Auslese eines Szintillationszählers mit selbstgetriggerter Elektronik, 2016.

[Mor] Hannes Morgenweck. Master thesis, to be published.

[T+18] M. Tanabashi et al. Review of Particle Physics. *Phys. Rev.*, D98(3):030001, 2018.

Acknowlegements

First of all, I want to thank Prof. Dr. Anton Andronic and Prof. Dr. Christian Klein-Bösing for giving me the opportunity to write this thesis and providing helpful advice whenever needed. Furthermore, i give my special thanks to Philipp Kähler for all the help in form of suggestions, constructive criticism, discussions of plots and proof reading. I thank also the additional proof readers Daniel Mühlheim, Hendrik Poppenborg, Florian Jonas and my parents Monika and Sven Meyer-Ahrens.

Declaration of Academic Integrity

I hereby confirm that this thesis on *Electron Detection Efficiency of the CBM-TRD Prototypes in Testbeams at DESY* is solely my own work and that I have used no sources or aids other than the ones stated. All passages in my thesis for which other sources, including electronic media, have been used, be it direct quotes or content references, have been acknowledged as such and the sources cited.

(date and signature of student)

I agree to have my thesis checked in order to rule out potential similarities with other works and to have my thesis stored in a database for this purpose.

(date and signature of student)